FAILURE INVESTIGATION OF COMPOSITE MATERIALS USING MULTI-INSTRUMENT EXPERIMENTAL TECHNIQUES AND NUMERICAL METHOD

by
RAJA MUHAMMAD AWAIS KHAN

Submitted to the Graduate School of Engineering and Natural Sciences
in partial fulfillment of
the requirements for the degree of Doctor of Philosophy

Sabanci University
July 2021

FAILURE INVESTIGATION OF COMPOSITE MATERIALS USING MULTI-INSTRUMENT EXPERIMENTAL TECHNIQUES AND NUMERICAL METHOD

Approved by:

Date of Approval: July 14, 2021

ABSTRACT

FAILURE INVESTIGATION OF COMPOSITE MATERIALS USING MULTI-INSTRUMENT EXPERIMENTAL TECHNIQUES AND NUMERICAL METHOD

RAJA MUHAMMAD AWAIS KHAN

Materials Science and Nano-Engineering Ph.D. Dissertation, July 2021

Dissertation Supervisor: Prof. Dr. Mehmet Yildiz

Keywords: Structural health monitoring, Failure analysis, Angle-ply CFRPs, Size-effect, Interacting holes

Carbon fiber reinforced polymer matrix laminates are widely used in aerospace, automotive, turbine blades and marine structures due to their light weight, and high specific stiffness and strength. Another important feature of laminated composites is anisotropy, which enables one to tailor their strength depending on the stacking sequences and the constituent material combinations. However, failure analysis of fiber laminates is very complicated process due to the presence of multiple constituents and spatially heterogenous damage accumulation inside the material. Therefore, an extensive investigation is carried out in the current study to comprehensively analyze various failure modes and damage growth in carbon fiber reinforced polymer composites, under various loading conditions, by simultaneously utilizing numerous structural health monitoring techniques. The outcomes of these investigations have resulted in four distinct papers and are presented individually in this study.

In the first paper, acoustic emission (AE) analysis coupled with digital image correlation (DIC) is used to study the effect of end-tabs' material on the mechanical properties and failure accumulation in angled-ply unidirectional carbon fiber reinforced plastics (CFRPs), under tensile loading condition. The strain fields, obtained from DIC, are found to be relatively more uniform, indicating an effective load transfer to gauge section, when the difference between the elastic modulus of the tab material and test material becomes smaller. The damage accumulation rate from the evolution of AE energy results determined three

distinct stages in AE activity. The duration of the second stage is observed to be longer, slower damage progression, in the specimens with smaller difference in elastic modulus between the tab material and the test material, supplementing the DIC analysis.

The second paper from this thesis, utilizes a comparison between three different strain monitoring techniques, namely DIC (contact-less), Fiber Brag's Grating (FBG) sensors (embedded) and strain gauge (surface mounted), simultaneously during tensile testing of the multidirectional (angled-ply) CFRP laminates. This assisted not only to effectively monitor the strain evolution but also directed to analyze through the thickness failure progression by correlating the inconsistencies in strain measurements from different methods with the tendency of interlaminar delamination due to distinct layup sequence in each laminate. To complement further, AE, and Infra-red thermography (IRT) are also employed simultaneously to identify and classify the characteristic failure types as matrix crack, interface failure or fiber failure.

The third paper investigates the size-effect i.e., the effect of thickness variation on the mechanical properties and failure dynamics of woven CFRPs under tensile and in-plane shear loading, by simultaneously employing AE, DIC, and IRT. Wherein, it is revealed that micro-damage initiation point is observed earliest in the thinnest laminate, showing lowest maximum tensile and shear strengths, as compared to the thicker ones. The failure accumulation in thicker laminates is found to be delayed due to activation of delamination failure in thicker laminates unlike the thinner ones, in which, the damage is predominantly controlled by comparatively lower energy release phenomenon i.e., matrix cracking.

The fourth paper in this thesis presents a comparison and scrutinization of failure initiation and progression in laminates containing two interacting notches with that of single notched laminate under tensile loading, by utilizing DIC and IRT simultaneously. The physics, behind the increase in strength and the decrease in stress concentration around the notches in laminates with two holes drilled parallel to the loading direction as compared to that of single hole laminate, was successfully unearthed. It was revealed that a relatively high energy release rate mechanism i.e., interface failure was more dominant in the laminates with two holes, parallel to loading axis, as compared to a low energy release mechanism i.e., transverse matrix cracking, being dominant in single hole laminates.

ÖZET

FAILURE INVESTIGATION OF COMPOSITE MATERIALS USING MULTI-INSTRUMENT EXPERIMENTAL TECHNIQUES AND NUMERICAL METHOD

RAJA MUHAMMAD AWAIS KHAN

Materials Science and Nano-Engineering Ph.D. Dissertation, July 2021

Dissertation Supervisor: Prof. Dr. Mehmet Yildiz

Keywords: Structural health monitoring, Failure analysis, Angle-ply CFRPs, Size-effect, Interacting holes

Karbon fiber takviyeli polimer matris laminatlar, hafiflikleri ve yüksek özgül sertlikleri ve mukavemetleri nedeniyle havacılık, otomotiv, türbin kanatları ve deniz yapılarında yaygın olarak kullanılmaktadır. Lamine kompozitlerin bir diğer önemli özelliği, istifleme dizilerine ve bileşen malzeme kombinasyonlarına bağlı olarak mukavemetlerinin ayarlanmasını sağlayan anizotropidir. Bununla birlikte, fiber laminatların başarısızlık analizi, çoklu bileşenlerin mevcudiyeti ve malzeme içinde mekansal olarak heterojen hasar birikimi nedeniyle çok karmaşık bir süreçtir. Bu nedenle, mevcut çalışmada, karbon fiber takviyeli polimer kompozitlerdeki çeşitli arıza modlarını ve hasar büyümesini, çeşitli yükleme koşulları altında, aynı anda çok sayıda yapısal sağlık izleme tekniğini kullanarak kapsamlı bir şekilde analiz etmek için kapsamlı bir araştırma yapılmıştır. Bu araştırmaların sonuçları dört farklı makaleyle sonuçlanmıştır ve bu çalışmada ayrı ayrı sunulmuştur.

İlk makalede, açılı-kat tek yönlü karbon fiber takviyeli plastiklerde uç tırnak malzemesinin mekanik özellikler ve arıza birikimi üzerindeki etkisini incelemek için çekme yükleme koşulu altında dijital görüntü korelasyonu (DIC) ile birleştirilmiş akustik emisyon (AE) analizi kullanılmıştır. (CFRP'ler) . DIC'den elde edilen gerinim alanlarının nispeten daha muntazam olduğu bulunmuştur, bu da tırnak malzemesinin elastik modülü ile test malzemesi arasındaki fark küçüldüğünde ölçü uzunluğuna etkin bir yük aktarımını gösterir. AE enerji sonuçlarının evriminden kaynaklanan hasar birikim oranı, AE aktivitesinde üç farklı aşama belirledi. İkinci aşamanın süresinin daha uzun olduğu, hasar ilerlemesinin daha yavaş

olduğu, tırnak malzemesi ile test malzemesi arasındaki elastik modül farkının daha küçük olduğu numunelerde, DIC analizine ek olarak gözlemlenmiştir.
Bu tezin ikinci makalesi, çok yönlü (yani açılı-kat) CFRP laminatların çekme testi sırasında üç farklı eş zamanlı gerinim izleme tekniği arasında bir karşılaştırma yapılmıştır. Kullanılan gerinim ölçüm teknikleri, DIC (temassız), Fiber Bragg Izgara (FBG) sensörleri (gömülü) ve gerinim ölçerdir (yüzeye monte). Bu, yalnızca gerinim gelişimini etkili bir şekilde izlemeye yardımcı olmakla kalmayıp, aynı zamanda farklı yöntemlerden gelen gerinim ölçümlerindeki tutarsızlıkları, her bir laminattaki farklı döşeme dizisinden dolayı katmanlar arası delaminasyon eğilimi ile ilişkilendirerek, kalınlık bozulması ilerlemesini analiz etmeye yönlendirildi. Daha fazlasını tamamlamak için, AE ve Kızılötesi termografi (IRT) aynı zamanda matris çatlağı, arayüz hasari veya fiber kırılması olarak karakteristik hasar tiplerini tanımlamak ve sınıflandırmak için de kullanılır.
Üçüncü makale, aynı anda AE, DIC ve IRT kullanarak, çekme ve düzlem içi kesme yüklemesi altında dokuma CFRP'lerin mekanik özellikleri ve kırılma dinamikleri üzerindeki kalınlık değişiminin etkisini, yani boyut etkisini araştırmaktadır. Burada, mikro hasar başlama noktasının en ince laminatta en erken gözlemlendiği ve daha kalın olanlara kıyasla en düşük maksimum çekme ve kesme mukavemetlerini gösterdiği ortaya konmuştur. Daha kalın laminatlardaki arıza birikiminin, daha ince laminatların aksine, daha kalın laminatlardaki delaminasyon başarısızlığının aktivasyonu nedeniyle geciktiği bulunmuştur, burada hasarın ağırlıklı olarak nispeten daha düşük enerji salımı fenomeni, yani matris çatlaması tarafından kontrol edilir.
Bu tezdeki dördüncü makale, DIC ve IRT'yi aynı anda kullanarak, çekme yüklemesi altında etkileşimli iki çentik içeren laminatlarda, tek çentikli laminatınki ile başarısızlık başlangıcı ve ilerlemesinin bir karşılaştırmasını ve incelemesini sunar. Yükleme yönüne paralel olarak açılan iki delikli laminatlarda tek delikli laminatlara göre mukavemet artışının ve çentiklerin etrafındaki gerilme konsantrasyonunun azalmasının arkasındaki fizik başarıyla ortaya çıkarılmıştır. Yükleme eksenine paralel iki delikli laminatlarda nispeten yüksek bir enerji salım hızı mekanizması, yani arayüz arızasının, tek delikli laminatlarda baskın olan düşük enerji salım mekanizması yani enine matris çatlaması ile karşılaştırıldığında daha baskın olduğu ortaya çıktı.

To my beloved parents, sisters, brothers,

To my lovely daughters

&

To my sincere wife

TABLE OF CONTENTS

CHAPTER 1. INTRODUCTION 1

1. 1. A Statement of Problem 1

1. 2. Description of Remaining Chapters 4

CHAPTER 2. DETERMINING TAB MATERIAL FOR TENSILE TEST OF CFRP LAMINATES WITH COMBINED USAGE OF DIGITAL IMAGE CORRELATION AND ACOUSTIC EMISSION TECHNIQUES 7

2. 1. Introduction 7

2. 2. Materials 10

2. 3. Experimental Procedure 11

2. 3. 1. Manufacturing of Tab Material 11

2. 3. 2. Mechanical Testing 12

2. 3. 3. Acoustic Emission (AE) 13

2. 3. 4. Digital Image Correlation (DIC): 14

2. 4. Results and Discussions 15

2. 4. 1. Statistical Approach for Tab Material Selection 15

2. 4. 2. Full Field Strain Analysis for Tab Selection 17

2. 4. 3. Damage Accumulation through Acoustic Emission Analysis 21

2. 5. Conclusion 26

CHAPTER 3. INVESTIGATION ON INTERLAMINAR DELAMINATION TENDENCY OF MULTIDIRECTIONAL CARBON FIBER COMPOSITES 28

3. 1. Introduction 28

3. 2. Materials 32

3. 3. Experimental Procedure 33

3. 3. 1. Manufacturing of Laminates 33

3. 3. 2. Mechanical Testing 33

3. 3. 3. Acoustic Emission (AE) and Digital Image Correlation (DIC) 34

3. 3. 4. Infrared Thermography (IRT) and Fiber Bragg Grating (FBG) 35

3. 3. 5. Set Up of Hybrid Evaluation Test 35

3. 4. Results and Discussion 36

3. 5. Conclusion: 47

CHAPTER 4. A NOVEL HYBRID DAMAGE MONITORING APPROACH TO UNDERSTAND THE CORRELATION BETWEEN SIZE EFFECT AND FAILURE BEHAVIOR OF TWILL CFRP LAMINATES 49

4. 1. Introduction 50

4. 2. Materials 53

4. 3. Experimental Procedure 53

4. 3. 1. Manufacturing of Laminates 53

4. 3. 2. Sample Preparation for Mechanical Tests 54

4. 4. Results and Discussion 55

4. 4. 1. Tensile Test Results 55

4. 4. 2. Shear Test Results 64

4. 5. Conclusions 71

CHAPTER 5. STRESS CONCENTRATION, STRENGTH PREDICTION, AND FAILURE ANALYSIS OF PLAIN-WEAVE CFRP WITH TWO INTERACTING NOTCHES 72

5. 1. 1. Introduction 73

5. 2. Experimental Setup and Numerical Modelling 76

5. 2. 1. Material 76
5. 2. 2. Manufacturing of Plain Weave CFRP laminates 76
5. 2. 3. Mechanical Testing 76
5. 2. 4. Digital Image Correlation (DIC) 78
5. 2. 5. Infrared Thermography (IRT) 79
5. 2. 6. Fractography 79
5. 2. 7. Numerical modelling 79
5. 3. Results and Discussion 81
5. 3. 1. Mechanical Test Results 81
5. 3. 2. Numerical Analysis 82
5. 3. 3. Critical Region Determination by DIC 85
5. 3. 4. Progressive Failure Analysis by IRT 87
5. 3. 5. Fracture Surface Analysis 92
5. 4. Conclusions 94
CHAPTER 6. CONCLUSIONS 96
REFERENCES 99

LIST OF TABLES

Table 2-1. Layup orientation of prepared laminates 11

Table 2-2. Specimen nomenclature 13

Table 2-3. Weighted peak frequency range for clustering 14

Table 2-4. Average & standard deviation of ultimate tensile strength of specimens 17

Table 3-1. Samples names and layup orientations 33

Table 3-2. Weighted peak frequency range for clustering 35

Table 3-3. Failure description for each laminate 47

Table 4-1. Prepreg specifications 53

Table 4-2 Configuration of twill laminates 54

Table 4-3 Specimens' Nomenclature 55

Table 4-4 Maximum Tensile Strength of Specimens 56

Table 4-5 Maximum Shear Strength of Specimens 65

Table 5-1. Specimen dimensions (all dimensions in mm) 77

Table 5-2. Average material properties of the fabricated plain-weave specimens 78

Table 5-3. Stress concentration factor for different notched plates 83

Table 5-4. Strength prediction by PSC and EPSC [120] approach 87

LIST OF FIGURES

Fig. 2-1. Dimensions of tensile test specimen 12

Fig. 2-2. Tensile specimen with speckle pattern & AE sensors 15

Fig. 2-3. Axial strain (ε_{yy}) field maps at (60, 80, 100)% σ_{UTS} for (a) C0 & G0, (b) C30 & G30, (c) C60 & G60, and (d) C90 & G90 18

Fig. 2-4. Typical failure for C0 & G0..... 21

Fig. 2-5. Comparison of stress-strain curve and AE data for ((a, b) C0 & G0) and ((c, d) C30 & G30) (MC-Matrix cracking, IF-Interface failure, FP-Fiber pullout, FB-Fiber breakage)22

Fig. 2-6. Out of plane displacement showing delamination for C30 sample 24

Fig. 2-7. Comparison of stress-strain curve and AE data for ((**a**, **b**) C60 & G60) and ((**c**, **d**) C90 & G90) (MC-Matrix cracking, IF-Interface Failure, FP-Fiber Pullout, FB-Fiber Breakage)..... 25

Fig. 3-1. Design of tensile specimen 34

Fig. 3-2 Schematic of experimental setup 36

Fig. 3-3. Stress-strain curves (SG: Strain gauge, DIC: Digital image correlation, FBG: Fiber Bragg's grating sensor)..... 37

Fig. 3-4. (a) Total AE cumulative energy and axial strain with time for specimen F0 (b) AE cumulative energy of each failure mode with time for specimen F0 (MC: Matrix cracking, IF: Interface failure, FP: Fiber pull-out, FB: Fiber breakage). Note: Points (i), (ii) and (iii) are marked to show the AE activity at 98, 154.4 and 301 seconds corresponding to the thermograms shown in Fig. 3-5 (i), (ii) and (iii), respectively 39

Fig. 3-5 Thermograms for specimen F0 at (i) 98 (12006με), (ii) 154.4 (11727με) and (iii) 301 (13825με) seconds corresponding to the points marked in Fig. 3-4b..... 40

Fig. 3-6. (a) Total AE cumulative energy and axial strain with time for specimen F15 (b) AE cumulative energy of each failure mode with time for specimen F15 (MC: Matrix cracking, IF: Interface failure, FP: Fiber pull-out, FB: Fiber breakage). Note: Points (i), (ii) and (iii) are marked to show the AE activity from 50.8 to 61.3 seconds, and at 104 and 107 seconds corresponding to the thermograms shown in Fig. 3-7 (i), (ii) and (iii), respectively 41

Fig. 3-7 Thermograms for specimen F15 at (i) 50.8 (5600με) – 61.3 (6453με) (ii) 104 (11855με) and (iii) 107 (11995με) seconds corresponding to the points marked in Fig. 3-6b 42

Fig. 3-8 Total AE cumulative energy and axial strain with time for specimen F45 (b) AE cumulative energy of each failure mode with time for specimen F45 (MC: Matrix cracking, IF: Interface failure, FP: Fiber pull-out, FB: fiber Breakage). Note: Points (i), (ii), (iii) and (iv) are marked to show the AE activity at 97, 133.5, 150 and 219 seconds corresponding to the thermograms shown in Fig. 3-9 (i), (ii), (iii) and (iv), respectively 43

Fig. 3-9 Thermograms for specimen F45 at (i) 97 (13478με) (ii) 133.5 (16728με) (iii) 150 (17732με) and (iv) 219 (19539με) seconds corresponding to the points marked in Fig. 3-8b 44

Fig. 3-10 (a) Total AE cumulative energy and axial strain with time for specimen F90 (b) AE cumulative energy of each failure mode with time for specimen F90 (MC: Matrix cracking, IF: Interface failure, FP: Fiber pull-out, FB: Fiber breakage). Note: Points (i), (ii) and (iii) are marked to show the AE activity at 35.4, 45 and 102 seconds corresponding to the thermograms shown in Fig. 3-11 (i), (ii) and (iii), respectively 45

Fig. 3-11 Thermograms for specimen F90 at (i) 35.4 (5670με) (ii) 45 (7058με) (three sequential images) and (iii) 102 (15468με) seconds corresponding to the points marked in Fig. 3-10b 46

Fig. 4-1. Vacuum bagging scheme for Twill CFRP prepreg..... 54

Fig. 4-2. Design of tensile specimen based on ISO 527-4 standard [24] (Thickness of laminates TW4s, TW6s and TW8s is 4.83 mm, 7.30 mm, and 9.87 mm, respectively)..... 55

Fig. 4-3. Representative k-means clusters for tensile Samples (a) T4-4, (b) T6-4 and (c) T8-4 from laminates TW4s, TW6s and TW8s, respectively, and (d) Average hit fraction for three failure types for each laminate (MC: Matrix cracking, IF: Interface failure, FB: Fiber breakage) 58

Fig. 4-4. Cumulative AE energy and tensile stress vs. time for specimens (a) T4-4, (b) T6-4 and (c) T8-4 (MC: Matrix cracking, IF: Interface failure, FB: Fiber breakage) 59

Fig. 4-5. Thermograms for representative specimen T4-4 from laminate TW4s at (a) 11 seconds, (b) 25 seconds (c) 30 seconds, (d) 33 seconds and (e) 72 seconds (MC: Matrix crack, FB: Fiber breakage/failure)..... 61

Fig. 4-6. Thermograms for representative specimen T6-4 from laminate TW6s at (a) 28 seconds, (b) 33 seconds (c) 38 seconds, and (d) 84 seconds (MC: Matrix crack, FB: Fiber breakage/failure)..... 62

Fig. 4-7. Thermograms for representative specimen T8-4 from laminate TW8s at (a) 40 seconds, (b) 55.8 seconds and (c) 56 seconds (MC: Matrix Crack)..... 64

Fig. 4-8. In-plane shear stress vs strain with DIC full field shear strain maps (ε_{xy}) at specified stress levels for samples S4-5, S6-5, and S8-5..... 65

Fig. 4-9. Representative k-means clusters for V-notch shear samples (a) S4-5, (b) S6-5 and (c) S8-5 from laminates TW4s, TW6s and TW8s, respectively, and (d) Average hit fraction for three failure types for each laminate (MC: Matrix cracking, IF: Interface failure, FB: Fiber breakage) 66

Fig. 4-10. Cumulative AE energy and in-plane shear stress vs. time for specimens (a) S4-5, (b) S6-5 and (c) S8-5 (MC: Matrix cracking, IF: Interface failure, FB: Fiber breakage) ... 68

Fig. 4-11. Temperature change ΔT vs. progression time of the shear test with irt thermograms at specified points (Inset 1 belongs to S8-5, Insets 2 & 7 belong to S6-5, Insets 3,4,5 & 6 belong to S4-5) 70

Fig. 5-1. Three well-known woven composites (a) Twill weave, (b) Plain weave, (c) Satin weave 73

Fig. 5-2. Schematic view of specimens 77

Fig. 5-3. Experimental setup including DIC cameras, IRT camera, load frame coupled with painted test sample 78

Fig. 5-4. Mesh convergence study ($\sigma_{11\,max}$ is the maximum tensile stress at vicinity of a hole) 80

Fig. 5-5. FEM model and applied boundary conditions together with the close-up view for the mesh resolution around a hole 80

Fig. 5-6. Comparison of FEM and average experimental result for the plane-weave plate without notch 81

Fig. 5-7. Average Tensile strength values of all the specimens with their corresponding standard deviation 82

Fig. 5-8. Stress in loading direction for final failure of (a) 1H, (b) 2H90, (c) 2H0, and (d) 2H45 (Arrows points to the loading direction) 83

Fig. 5-9. Averaged stress distributions of single hole and transverse holes 84

Fig. 5-10. Processing zone/critical region determination utilizing DIC experimental data. 85

Fig. 5-11. Averaged stress distributions and characteristic distance of 1H and 2H0 (DIC) 86

Fig. 5-12. IRT thermograms for sample 1H showing (a) initial delamination (462 MPa), (b) temperature distribution around the hole (523 MPa) and (c) final failure (528 MPa) 88

Fig. 5-13. IRT thermograms for sample 2H90 showing (a) initial delamination (528 MPa), (b), (c2) temperature distribution around the hole before and at maximum load (540 MPa), respectively, (d) final failure (529 MPa) and (c1) complimentary DIC image at max load 89

Fig. 5-14. IRT thermograms for sample 2H0 showing (a) initial delamination (309 MPa, 57.5 seconds), (b) complimentary DIC image after first failure, temperature distribution (c) at maximum load (368 MPa, 76.7 seconds), (d) before final failure, (e) at final failure (339 MPa, 89.5 seconds) and (f) complimentary DIC image after failure 90

Fig. 5-15. IRT thermograms for sample 2H45 showing (a) initial delamination (235 MPa, 41.8 seconds), (b) complimentary DIC image after first failure, (c) second delamination event, temperature distribution (d) before maximum load, (e) at maximum load (376 MPa, 89.7 seconds), (f) before final failure, (g) at final failure (353 MPa, 102.7 seconds) and (h) complimentary DIC image after failure 91

Fig. 5-16. Fracture surface morphology (Note: SLAD – Slanted large area delamination, TMC – Transverse matrix crack, FR – Fiber rotation)..... 92

CHAPTER 1. INTRODUCTION

1. 1. A Statement of Problem

Fiber reinforced plastics (FRP) have been extensively used in critical structural applications such as wind turbine blades, marine, aircraft and automotive components during the past few decades due to their higher specific strength and stiffness as compared to the metallic counterparts. The anisotropic nature of the FRPs further signifies their utilization which helps to tailor their mechanical properties in accordance with the in-service predicted loading conditions. One of the features which facilitates altering the mechanical properties of unidirectional (UD) FRP is the usage of multidirectional angle ply composites.

To be able to use FRPs reliably in critical engineering applications, their mechanical properties need to be determined accurately, which are notably affected by the adopted mechanical testing procedures. Among the most extensively conducted testing procedures for determining the mechanical properties of FRPs, ASTM D3039 “Standard Test Method for Tensile Properties of Polymer Matrix Composite Materials” is utilized the most. According to which, a standard tensile specimen of FRPs is recommended to have straight edges and failure region must be confined at the middle of the gauge length to avoid premature failure, which otherwise, results in under-estimation of mechanical properties. To assure occurrence of failure at gauge length of the specimen, the usage of end tabs, which can transfer clamping force to the specimen through shear action, is specifically recommended for unidirectional laminated composites (LCs) [1]. However, the usage of inappropriate tab materials could instigate problems such as failure within tab region and/or slippage of tabs, causing ineffective load transfer to the gauge section of the specimen. To solve this specimen design problem, it is inevitable to study and recommend an effective tab material. Considering this fact, the first step in the current study is focused on the determination of a suitable tab material for the tensile test of UD FRPs.

Apart from mechanical characterization of FRPs, failure analysis i.e., damage initiation and propagation in FRPs has always been an engineering challenge. Particularly, in case of multidirectional (angle ply) laminates, the presence of off-axis plies further complicates the process of damage origination and accumulation, thus implying that the failure types and their severity will be dependent on loading condition and material configuration i.e., lay-up of the laminate [2-6]. Considerable experimental and analytical research has been dedicated to study the failure modes in multidirectional fiber reinforced composites under tensile loading. But simultaneous utilization of multi-instrument experimental techniques not only to scrutinize the damage process but also to obtain strain occurring during a tensile test has not been done before, and this is considered in the second phase of the current study. It is shown that such a combination of experimental techniques opened new ways to obtain excessive information about the failure process in laminated composites (LCs).

As mentioned earlier that the properties of FRPs could be tailored easily by varying the stacking arrangement of laminates; the utilization of woven fabric also provide an opportunity to get additional benefits. However, the investigation of failure analysis due to the size-effect i.e., the effect of varying the thickness of woven FRPs on mechanical properties and failure dynamics is also another challenge, which is probed in the third phase of current work. Therefore, woven FRPs are studied to reveal the effect of size difference on (1) initiation of micro-damages, (2) activation of different failure modes, and (3) rate of failure accumulation, under tensile and in-plane shear loadings.

Further, in real scenarios (particularly for large structures), discontinuities such as holes, notches and non-uniformities are also inevitable for proper assemblage of the parts, causing additional complication due to stress concentrated around the hole(s) [7]. Considering these facts, the final stage of the current study focused on investigating the stress concentration around the hole(s) in woven FRP plates by tailoring the orientation of holes. The effect of interaction between holes on notch-sensitivity and failure behavior is scrutinized by utilizing and cross-validating numerical and experimental data. The physics behind the variation in stress-concentration and strength with changing orientation of holes is unearth by examining the variation in failure behaviors. The distinct failure behaviors due to different hole arrangements is shown to be associated with the dominancy of distinctive failure modes.

To deliver the experimental results and to analyze the failure progression under tensile and in-plane shear loading conditions, the following structural health monitoring systems are utilized in a hybrid manner:

Digital Image Correlation (DIC) - is a non-contact full-field displacement monitoring method which uses a high resolution charged coupled device (CCD) camera(s) to record series of images of a sample's surface having high contrast speckle pattern. The surface under the study is divided into several distinctive regions called "facets". Each facet region encloses subset of image pixels. Under a loading cycle, the facets on the speckle surface are tracked continuously which enable to record the progressive surface deformation. The consecutive deformed surfaces under the load are compared with the unloaded reference image utilizing a correlation algorithm to calculate full field strain. The average of the strains calculated at each facet point provide a global average strain value similar to the one obtained by a strain gauge [8].

Fiber Bragg's Grating (FBG) sensors - have been widely employed as embedded sensors inside composite materials for evaluation of mechanical strain, residual cure strain, temperature, and pressure [9-11]. As strain is applied on composite laminate causes an elastic strain on embedded FBG, therefore changing the Bragg wavelength λ_B of grating. This change in Bragg wavelength at constant temperature is related to mechanical strain ε_{app} as:

$$\frac{\Delta\lambda_B}{\lambda_B} = (1 - P_e)\Delta\varepsilon_{app}$$

Where P_e is the strain-optic coefficient of the fiber.

Acoustic Emission (AE) - method is used to distinguish possible damage generation mechanisms (Matrix cracking, Interface failure, Fiber failure (rupture & pull-out)), which are particularly important for failure assessment of composite materials. AE technique uses piezo-electric sensors which are sensitive to short and weak transient waves released by micro-damage formation. Several studies have employed AE method during the tensile test of LCs where transient waves generated by micro damage formations are recorded and classified [12, 13]. A variety of classification procedures can be found in literature which use different features of waves such as rise time, peak amplitude, peak frequency and weighted peak frequency [14]. Among these features, the usage of weighted peak frequency with the unsupervised K-means algorithm is the most promising one.

Infrared Thermography (IRT) - method provides an in-situ monitoring method, in passive mode, to observe the changes in temperature due the emission of infra-red radiation from the surface of a material owing to the damages occurring in the material under mechanical loading. These damages generate localized heat zones causing temperature fluctuations directing to the identification of location, severity, and type of damage [15]. Besides AE,

DIC and FBG data, the usage of passive thermography can also provide complementary information for monitoring damage evolution under different loading conditions.

Overall, this thesis provides a comprehensive investigation of full processing cycle of laminated fibrous composites starting from specimen design improvement for precise mechanical property characterization which is one of the paramount aspects of material qualification in aerospace industry. Additionally, to create a holistic understanding of complex failure dynamics due to anisotropic characteristics of angled-ply laminates, single instrument monitoring is not enough. Therefore, a full fledge multi-instrument so called a hybrid damage monitoring system is utilized to deepen the insight of failure progression in composites. After suggesting specimen design improvements and broadening the understanding about failure dynamics in composite materials, composite materials strength size effects is scrutinized which directs to strength the knowledge base for estimating performance of composites at real systems. Additionally, at actual scenarios, particularly in giant structures, part assembly requires drilling many holes causing undesired stress concentrations, leading to strength reduction, and added complications. Directing to in-depth analysis of failure dynamics in composites with hole(s), which is carried out in the current study by utilizing structural health monitoring.

1. 2. Description of Remaining Chapters

In the subsequent chapters the outcomes of the research approach adopted in this study are presented. The findings as detailed in chapter 2, 3, and 4 are associated with published articles in reputed journals, while the article associated with chapter 5 is currently under review. In the last chapter the overall conclusions of this study are reported. A brief description of chapters 2, 3, 4 and 5 is as follow:

In the 2nd Chapter of the thesis, an appropriate tab material for tensile tests of UD carbon fiber reinforced plastics (CFRPs) is proposed by concurrently utilizing DIC and AE to monitor the mechanical response of 7 unique UD laminates with varying stacking sequences. Two different tab materials namely CFRP and glass fiber reinforced plastic (GFRP) were scrutinized. Remarkably, it was unveiled that the full field strain maps obtained through DIC showed a distinct relationship between uniformity of strain field at gauge length and tab material used for tensile tests. The strain fields were found to be relatively more uniform,

indicating an effective load transfer to gauge section, when the difference between the elastic modulus of the tab material and test material became smaller. The damage accumulation rate from the evolution of AE energy results determined three distinct stages in AE activity. The duration of the second stage was observed to be longer meaning slower damage progression in the specimens with smaller difference in elastic modulus between the tab material and the test material, supplementing the DIC analysis.

In the 3rd chapter, the different strain monitoring techniques, namely DIC (contact-less), FBGs (embedded) and SG (surface mounted) are adopted and compared simultaneously during tensile testing of multidirectional (angled-ply) CFRP laminates. This assisted not only to effectively monitor the strain evolution but also directed to analyze through the thickness failure progression by correlating the inconsistencies in strain measurements from different methods with the tendency of interlaminar delamination due to distinct layup sequence in each laminate. To complement further, AE and IRT were also employed simultaneously to identify and classify the characteristic failure types as matrix crack, interface failure or fiber failure. Apart from the unmatched capabilities of multi-instrumental (hybrid) approach in damage characterization (initiation and accumulation), it was shown that in case of an unexpected disintegration of one or more system(s), particularly during the mechanical testing of angled-ply FRPs, multiple monitoring systems can be advantageous.

Acknowledging the competencies of hybrid failure progression analysis approaches, the investigation in 4th chapter of this thesis is focused on the effect of thickness variation on the mechanical properties and failure dynamics of woven CFRPs under tensile and in-plane shear loadings, by simultaneously employing AE, DIC, and IRT. Wherein, it was revealed that micro-damage initiation point is observed earliest in the thinnest laminate, showing lowest maximum tensile and shear strengths, as compared to the thicker ones. The failure accumulation in thicker laminates was found to be delayed due to activation of delamination failure in thicker laminates unlike the thinner ones, in which, the damage is predominantly controlled by comparatively lower energy release phenomenon i.e., matrix cracking.

The 4th paper included in this study as chapter-5 contains investigation on notched woven CFRPs with an aim to reduce the notch sensitivity. A comparison and scrutinization of failure initiation and progression in laminates containing two interacting circular notches with that of single notched laminates under tensile loading by utilizing DIC and IRT simultaneously, is presented. The physics, behind the increase in strength and the decrease in stress concentration around the notches in laminates with two holes drilled parallel to the loading direction as compared to that of single hole laminate, was successfully unearthed. It

was revealed that a relatively high energy release rate mechanism i.e., interface failure was more dominant in the laminates with two holes, parallel to loading axis, as compared to a low energy release mechanism i.e., transverse matrix cracking, being dominant in the single hole laminates.

CHAPTER 2. DETERMINING TAB MATERIAL FOR TENSILE TEST OF CFRP LAMINATES WITH COMBINED USAGE OF DIGITAL IMAGE CORRELATION AND ACOUSTIC EMISSION TECHNIQUES

Determining the precise tensile strength of carbon fiber reinforced polymer matrix composites is very important due to their anisotropic properties. In this study, tensile tests are carried out on carbon fiber reinforced laminates with glass and carbon fiber reinforced tab materials. Tests are conducted with concurrent monitoring of mechanical behavior of specimens through digital image correlation and acoustic emission techniques. Remarkably, the full field strain maps obtained through digital image correlation show that there is a relationship between uniformity of strain field at gauge length and tab material used for tensile tests. Three distinct stages of acoustic emission activity are determined, in which the duration of second stage changes significantly depending on the tab material used for tensile test.

2. 1. Introduction

Fiber reinforced polymer (FRP) matrix composites are commonly used at critical areas of engineering structures due to their high specific strength. Another important feature of FRPs is anisotropy, which enables one to tailor their strength depending on the stacking sequences and the constituent material combinations. To be able to use FRPs reliably in critical engineering applications, their mechanical properties need to be determined accurately, which are notably affected by mechanical testing and manufacturing procedures utilized. Some of the factors that considerably influence the mechanical performance of FRPs are fiber misalignment, manufacturing defects, size effect and test specimen design variables. Fiber misalignment has been revealed to have an adverse effect on mechanical properties of fiber reinforced polymers specifically on the compressive strength [16-18]. In a

comprehensive review by Mehdikhani et al., it is concluded that 1% increase in the void content due to improper manufacturing procedure, can decrease tensile strength of a laminate between 10-20% [19]. Specimen dimension in composite materials can also cause a change in the strength of material, known as size effect. Therefore, reliable scaling up from test coupons to realistic composite structures is very crucial [20]. Specifically, the presence of tab material at the grip location results in a variation in the thickness of the specimen along its length, which can have deteriorating effect on the mechanical properties of composite materials. Wisnom et al. in their investigation mentioned that high strength of fibers inside laminates causes unsuccessful transfer of load from grips of tensile specimen to gauge length, thus resulting in premature failure of the laminate at grip regions. To avoid the failure at the grip location due to the size effect, they produced tensile specimen with specific tapering for tensile test [21]. Lavoie et al. also mentioned that reason of size-strength (i.e., size effect) is related to the ability of the material to transfer the load smoothly across varying thicknesses [22]. They found that size effect is present for composite specimens which fail at grip region under tensile loading conditions and applying *Weibull* theory is not a good approach to determine size-strength relationship in unidirectional laminates. In a recent approach, the size effect in unidirectional composite laminates has been attempted to be alleviated using of glass/carbon hybrid specimens [23]. Despite all the mentioned efforts, the problem of size-strength is basically related to test specimen design, the factor that can drastically cause premature failure of composite laminates under mechanical loading.

According to ASTM D3039, a standard tensile specimen for fiber reinforced polymer matrix composites is recommended to have straight edges and failures region must be confined to gauge length of the specimen away from the grip region for avoiding premature failure [1]. To assure occurrence of failure at gauge length of the specimen, the usage of end tabs, which can transfer clamping force to the specimen through shear action, is specifically recommended for unidirectional laminates. Portnov et al. developed an analytical approach to find the stresses near the end tabs of a unidirectional laminates, and concluded that preventing the stress concentration near the grips is almost impossible and proper shear transfer happens if the maximum shear stresses are located at back edge of the grips [24]. Some of the efforts to solve this problem are reported herein. An early report provided by NASA recommended that the end tabs should be selected based on deformation behavior and anisotropic properties of tab material [25]. Kulakov et al. did experimental and numerical analysis, and found that orthogonally glass fiber reinforced polymer GFRP tabs with bevel angle of less than 10°, adhered with a low modulus polyurethane adhesive was

the best choice for the unidirectional CFRP laminates [26]. De Baere et al. used finite element modeling to choose between various tab geometries and materials for polyphenylene sulfide (PPS) thermoplastic laminates, and found that using similar material to that of the specimen itself can reduce stress concentration at grip region but problems regarding adhesive bonding should be considered [27]. Tahir et al. used novel aluminum tab geometry that elongated all through the specimen with hole shaped as a rounded rectangle in the middle. Their results indicated that the stress concentration near the tab was reduced up to 10% in the unidirectional thermoplastic carbon fiber reinforced polymer (CFRP) laminates [28]. Results of experiments conducted by Odegard et al. suggested that at high temperatures, the stress concentration in the grip region was alleviated, and therefore strength was not influenced even if carbon/polymerization of monomeric reactants (PMR-15) laminates failed at the grip region [29]. Kawai et al. used several strain gauges along the gauge length to show that the strain field of CFRP specimens with low aspect ratio and off axis plies was more homogenous when oblique tabs were used [30]. Another report released by Federal Aviation Administration recommended that the GFRP were better choice as the end tab materials due to their low stiffness [31]. In a recent study, Czél et al. showed that using thin carbon ply sandwiched between glass layers disregards the necessity for end tabs, thus creating no stress concentrations at grip region [32]. To the author best knowledge, most studies have focused on modifications in geometry and variety of materials to reduce stress concentration at grip region, and handful number of researches have been conducted to analyze strain maps throughout gauge length and see how successful end tabs are performing [33]. Using new full field strain measurements techniques such as digital image correlation (DIC) has never been studied and the author believe monitoring strain map variation for similar samples with different tab materials will give a valuable data about efficiency of the end tab materials.

DIC is one of the optical methods for full field strain measurement on the surface of materials. This method basically uses an algorithm to correlate consecutive images of stochastic patterns on material surface during deformation [34]. Several investigations have used DIC to analyze appropriateness of tensile test condition of composite materials such as analyzing the failure progress towards end tabs, possible slippage at end tab and clamping regions and stress concentration region which causes early failure in tensile tests [35-38]. Some researchers have used DIC combined with other monitoring techniques such as acoustic emission method to better understand the failure development inside composite materials [39-41].

Acoustic emission analysis is one of the methods that can provide a very good data about the quantity, time and rate of occurrence for various damages inside fiber reinforced laminates [42]. Yilmaz et al. in their recent investigation used acoustic emission analysis to correlate between the number of different micro-damage types and delamination susceptibility [43]. Carvelli et al. showed that initiation points of the damages inside the reinforced PPS laminates corresponded to an abrupt change in the cumulative energy of acoustic emission activity [14]. Oz et al. used acoustic emission cumulative energy results to show that the layup orientation affected acoustic emission results in composite laminates [41]. Fotouhi et al distinguished three different steps for failure of the thin ply UD hybrid laminates with the help of acoustic emission [44]. Despite presence of various studies regarding damage accumulation through acoustic emission, there is no research about effect of tab material in tensile test on damage evolution for composite laminates with various layups.

Authors believe that this is the first study to discuss the effect of tab material on strain distribution and damage accumulation at gauge length of tensile samples. In the following parts of this chapter, properties of the materials used for analysis through investigation are given. Afterwards, the experimental procedure is explained in detail regarding manufacturing of composite laminates and tabs, mechanical tests performed, damage monitoring through DIC, acoustic emission monitoring and classifying damage types. In the next part, results of tensile tests are compared, strain fields obtained for samples with various stacking sequence are given and then, acoustic emission energy accumulation is given for each laminate and correlated with the observations from DIC. Finally concluding remarks are presented to summarize the achievements of investigation.

2. 2. Materials

Unidirectional carbon prepreg composed of carbon fiber T700 12K and epoxy resin referred with the commercial code of OM10 is purchased from KORDSA with the product code of KOM10 T700 12KT UD300 37% 600 KOMP. The fiber areal weight is 300 g/m2 and the resin content is 37% by weight. The average glass transition temperature (Tg) is found to be 123±2 °C using Differential Scanning Calorimetry (DSC), DSC3+ Mettler Toledo. The glass fiber prepreg consisting of epoxy resin (OM10) and stitched unidirectional E-glass fabric

with the areal weight of 330 g/m2 is also acquired from Kordsa with the commercial code of KOM10 EGF UD330.

2. 3. Experimental Procedure

The CFRP prepregs were cut using a ZÜND G3-L3200 digital cutting machine into dimensions of 30cm x 40cm based on the desired orientations. A steel mold was cleaned properly with ethanol and 3 layers of sealer (XTEND 838) & releaser (XTEND CX-500) agents were applied to surface of the steel mold in sequence with about 20 minutes of time interval so that each layer can dry totally. The cut prepregs were stacked manually onto the steel mold and were then cured utilizing a manual hot press (MSE Teknoloji Ltd.). The curing cycle includes the following steps: (i) initially heating the press to a temperature of 80 °C, (ii) placing the steel mold (containing the stacked prepregs) in the press, (iii) applying a pressure of 3 bars for 5 mins at 80 °C, (iv) gradually increasing the temperature to 120 °C by keeping pressure at 3 bars, (v) increasing the pressure to 7.5 bars, (vi) maintaining the pressure (7.5 bars) and temperature (120 °C) for 60 mins & (vii) cooling to a temperature below 60 °C before releasing the pressure. In total, 7 CFRP laminates were produced, and each comprises 8 layers of carbon-fabric with various lay-up orientations as summarized in Table 2-1, where the zero-degree fiber refers to axial direction. The thickness of the laminates is in the range of 2.3 mm-2.5 mm.

Table 2-1. Layup orientation of prepared laminates

Short ID	Layup Orientation & Sequence
0	$[0°]_8$
15	$[15°/0°/-15°/0°]_s$
30	$[30°/0°/-30°/0°]_s$
45	$[45°/0°/-45°/0°]_s$
60	$[60°/0°/-60°/0°]_s$
75	$[75°/0°/-75°/0°]_s$
90	$[90°/0°/-90°/0°]_s$

2. 3. 1. Manufacturing of Tab Material

Two different tab materials were manufactured using the unidirectional carbon and glass fiber prepregs introduced previously with stacking sequence of $[45°/-45°]_{4s}$. This stacking

sequence is chosen as it provides a lower stress concentration for quasi static tensile test [45]. The curing process remained the same as that for CFRP laminates described above. The only difference in the manufacturing process was the use of peel plies on both the sides of laminates produced for the tabs. The main purpose of the peel plies was to ensure a rough surface of the laminates which eliminated a post-processing step of grinding the surfaces for proper adherence to the tensile specimens. Other than that, peel ply also eradicated the time required for preparing mold surfaces & assisted in easier removal of laminates from the mold.

2. 3. 2. Mechanical Testing

Six tensile test specimens were cut from each laminate with the ZÜND G3-L3200 digital cutting machine in dimensions given in Fig. 2-1, in accordance with ASTM D3039 standard. The length and width of the specimen were 25 cm & 2.5 cm, but, with the exception of unidirectional specimen for which the width was 1.5 cm instead of 2.5 cm. Depending on the dimensions of the tensile specimen, the tabs of dimensions 5 cm x 2.5 cm (or 1.5 cm) were also cut using the same digital cutter. Two sets of specimens (having 3 specimens each) were obtained; one set with the CFRP tabs & other one with the GFRP tabs. The tabs were adhered to the specimens' surface using an epoxy Araldite 2011.

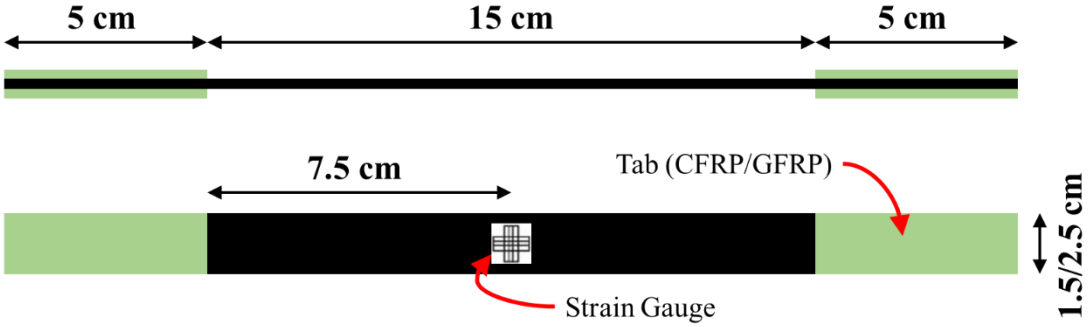

Fig. 2-1. Dimensions of tensile test specimen

Each set of specimens for tensile test was further divided into two categories based on the strain measurement and damage monitoring: 2 specimens with biaxial strain gauges and one specimen with AE & DIC (without resistive strain gauges). In former set of specimens, only strain gauge data were obtained during the tests while in the later, DIC and AE data were obtained simultaneously during the tests without using the strain gauges. Table 2-2 highlights the detailed nomenclature used throughout the chapter. The specimen ID provides the complete representation of the specimens; the first letter shows the material used for tabs,

the second number shows the stacking sequence of the specimen and the number after "-" shows the experiment number and/or condition. For instance, the specimen name "G30-1" shows that the tabs material is GFRP, the stacking sequence is $[30°/0°/-30°/0°]_s$, and the number "1" shows that only a strain gauge was used during the tensile test.

Table 2-2. Specimen nomenclature

Short ID	Tensile Test with Strain Gauge				Tensile Test with (DIC & AE)	
	Specimen ID				Specimen ID	
	CFRP-tabs		GFRP-tabs		CFRP-tabs	GFRP-tabs
0	C0-1	G0-1	C0-2	G0-2	C0	G0
15	C15-1	G15-1	C15-2	G15-2	C15	G15
30	C30-1	G30-1	C30-2	G30-2	C30	G30
45	C45-1	G45-1	C45-2	G45-2	C45	G45
60	C60-1	G60-1	C60-2	G60-2	C60	G60
75	C75-1	G75-1	C75-2	G75-2	C75	G75
90	C90-1	G90-1	C90-2	G90-2	C90	G90

For properly attaching the strain gauge, the middle of the specimen was roughened to adhere the strain gauge to the specimen. The biaxial strain gauges with the product code of C2A-06-125LT-350 (gauge factor of 2.16±1%) were provided by VISHAY Group. The tests were performed using an INSTRON 5982 universal mechanical tester with the load cell of 100 kN and speed was 2mm/min. All tests were continued until the global failure of the specimens.

2. 3. 3. Acoustic Emission (AE)

Wideband piezoelectric sensors (PICO-200-750 kHz, Mistras) were attached to one side of the specimens as depicted in Fig. 2-2 for the set of specimens for which AE & DIC data was required to be recorded. These sensors were used to sense the acoustic activity caused by the micro-damage activations occurring within the specimens. The signals obtained by the sensors were amplified through a Physical Acoustics 0/2/4 voltage preamplifier by a gain of 20dB and fed to a Mistras PCI-2 AE apparatus. The hardware parameters for AE apparatus were controlled by an AEwin PCI2-4 data acquisition software and were set to a threshold of 40 dB, hit lock-out time of 300 μs, peak definition time of 50 μs, and hit definition time of 150 μs. As a post-processing step, the recorded dataset is filtered in a Noesis 7 software, utilizing a Bessel band pass filter (20 kHz – 800 kHz). The extracted data after cleaning was clustered using K-means method in MATLAB environment as described comprehensively

in the previous works [43]. The optimum number of clusters was found utilizing a Silhouette criterion, which provides a visual understanding of the separation between the clusters. This criterion has a range of [-1,1], with clusters having values close to 1 are considered qualified efficiently based on the chosen number of the clusters. The clustering is done using two main features of the extracted data set; partial power1 and weighted peak frequency (WPF), as these two features reportedly provide a better clustering result as compared to that of any other features [46, 47]. Weighted peak frequency is the square root of multiplication of peak frequency and frequency centroid. These two features are obtained through implementation of Fast Fourier Transformation (FFT) on time domain waveform of each acoustic emission hit. Partial Power 1 shows what percent of total power in an acoustic emission wave is at the range of 0-250kHz. The approximate range of the weighted peak frequency obtained through implemented clustering algorithm for four failure mechanisms, namely; matrix cracking (MC), interface failure (IF), fiber pullout (FP) and fiber breakage (FB), are shown in the Table 2-3.

After conducting clustering procedure and determining present failure types during tensile loading condition according to a previous study stress strain curves are merged with cumulative energy release of acoustic emission activities (hits). This absolute energy is derived through applying integral of the squared voltage signal divided by reference resistance over acoustic emission waveform packet.

Table 2-3. Weighted peak frequency range for clustering

Failure Mechanism	Weighted Peak Frequency (kHz) Range
Matrix Cracking (MC)	< 240
Interface Failure (IF)	240 – 380
Fiber Pullout (FP)	380 – 520
Fiber Breakage (FB)	520 <

2. 3. 4. Digital Image Correlation (DIC):

Digital Image Correlation (DIC) was used mainly to monitor and measure the local strains over one surface of the tensile specimen. The respective surface of the specimen was speckle patterned throughout the gauge length using black and white spray paints with RAL codes 9005 and 9010 respectively as shown in Fig. 2-2. The DIC was carried out by 12M sensor system, provided by GOM (Braunschweig-Germany), calibrated in accordance with the manufacturer's directions based on a 250x200 mm calibration object. Single snap mode was adopted for calibrating the sensor with working distance of 1250 mm and camera angle of

25°. The results of calibration obtained were: calibration deviation = 0.037 pixels (limit value: 0.050 Pixels) and scale deviation = 0.002 mm (limit value: 0.022 mm). A facet and step size of 25 and 19 pixels, respectively was selected for tracking the speckle pattern during the mechanical test. To properly align, and to avoid twisting and/or bending of the specimen during the test; reference measurements were taken by DIC in a single image mode, and any discrepancies whichsoever could be present were removed before initializing the test. Moreover, the quality of the pattern was inspected using ARAMIS professional software to ensure optimum speckle pattern on surface of the samples. At the test, ARAMIS professional software was used to compute LaGrangian strains, deformation-maps, and strain-maps from the displacements of speckles. Macro damages such as large delamination within the laminates were also examined from the obtained deformation or strain maps.

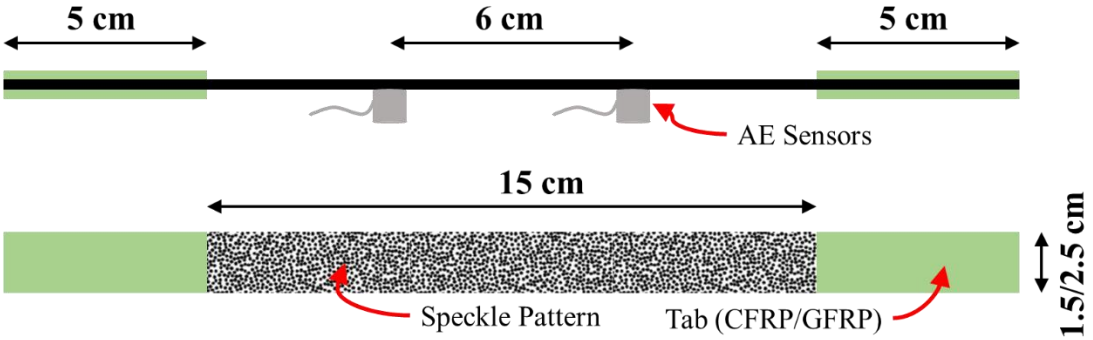

Fig. 2-2. Tensile specimen with speckle pattern & AE sensors

2. 4. Results and Discussions

2. 4. 1. Statistical Approach for Tab Material Selection

Table 2-4 represents the results of ultimate tensile strength for various specimens with different orientations and tab materials. The table contains the values of strength for 3 samples from each laminate both tested with carbon and glass tabs. This sampling size was selected based on the assumption of a margin of error equal to 15% of average strength for each laminate and 80% confidence level, therefore assuring correct statistical approach and ability to discuss standard deviation for each laminate. Two average values are reported for each configuration of laminate specifically based on tab material, i.e. carbon and glass tabs. Moreover, standard deviation for of each group of laminates is calculated and compared to get a better understanding about the effect of tab material.

As expected, highest values of strength are related to laminates with 0° fiber direction and lower values are obtained for off axis composite materials. The range of obtained strength values is between 1092 MPa for G30 specimen and 2082 MPa for C0-2 specimen. One can observe that the strength of laminates with different stacking sequences can vary drastically depending on the tab material. Deciding on the appropriate tab material merely based on the obtained strength values of test specimen is not a prudent method given that in some cases glass tabs result in higher strength while in other cases carbon tabs perform better. A suitable approach would be to consider the average values of tensile strength for each tab type. Table 2-4 presents the average values of tensile strength for each laminate where it is seen that carbon tabs give higher average values for laminates with $0°, 15°, 30°, 60°$ configuration. The average values of strength for 45° sample are almost the same and seem to be independent of tab material. For $75° \; and \; 90°$ specimens, glass tabs tend to give better average tensile strength results. Since materials used to prepare tensile specimen are cut from the same plate of reinforced laminates, their strengths in ideal conditions must be very close and very small deviation shall be seen in between different samples. This logic can be used to add an extra criterion for selecting best tab material; in other words, tab material with lower standard deviation would be a better choice for performing tensile test since it gives lower dispersal of strength for the same material. Considering this criterion, one can compare the standard deviations as seen in Table 2-4 and see that generally carbon tabs give lower deviation, thus providing less dispersion in data. Laminates with $0°, 15°, 30°, 60°$ fiber directions show considerably low standard deviation in case of using carbon tabs which show how important is type of tab material in attaining reasonable values of strength. Although the average values are similar for both tabs in specimen with 45° fiber direction, better standard deviation is attained for carbon tab. It is very interesting to notice the change in standard deviation in favor of glass tabs for $75° \; and \; 90°$ samples, hence indicating that glass tabs can be a better option for tensile test if angle of off-axis plies is more than 60°. As the angle of off-axis carbon fiber plies increases, the tensile strength of the CFRP laminate decreases, thereby causing a reduction in the stiffness difference between the specimen under load and the glass fiber tabs. Therefore, there is a less variation in the mechanical properties of the whole test specimen, causing a better performance with glass tabs when off-axis plies have a fiber angle above 60 degrees. So overall, it seems that decision about choosing the best tab material namely, being carbon or glass tabs, weighs up for carbon material in terms of statistics of mechanical responses. To elaborate on the reason for these results, it is better to use a set of mechanical assessment methods such as DIC and AE.

Table 2-4. Average & standard deviation of ultimate tensile strength of specimens

Specimen ID	σ_{UTS}	Specimen ID	σ_{UTS}	Specimen ID	σ_{UTS}	Standard Deviation		Average	
C0	1607.0	**C0-1**	2082.0	**C0-2**	1958.0	183.6	**C < G**	1882.3	**C > G**
G0	1474.0	**G0-1**	1926.6	**G0-2**	1298.3	240.2		1566.3	
C15	1301.0	**C15-1**	1280.6	**C15-2**	1305.6	10.1	**C < G**	1295.7	**C > G**
G15	1390.0	**G15-1**	1210.0	**G15-2**	1212.5	79.5		1270.8	
C30	1256.0	**C30-1**	1183.7	**C30-2**	1235.6	27.6	**C < G**	1225.1	**C > G**
G30	1092.0	**G30-1**	1248.1	**G30-2**	1151.7	56.1		1163.9	
C45	1327.0	**C45-1**	1366.9	**C45-2**	1201.4	64.7	**C < G**	1298.4	**C ≈ G**
G45	1121.0	**G45-1**	1357.2	**G45-2**	1432.1	121.6		1303.4	
C60	1206.0	**C60-1**	1231.0	**C60-2**	1327.7	48.5	**C < G**	1254.9	**C > G**
G60	1104.0	**G60-1**	1271.3	**G60-2**	1259.0	71.6		1211.5	
C75	1336.0	**C75-1**	1412.7	**C75-2**	1276.7	47.3	C > G	1341.8	C < G
G75	1386.0	**G75-1**	1386.1	**G75-2**	1296.9	39.6		1356.3	
C90	1238.0	**C90-1**	1232.3	**C90-2**	1283.6	21.5	C > G	1251.3	C < G
G90	1334.0	**G90-1**	1315.3	**G90-2**	1318.1	7.7		1322.5	

2. 4. 2. Full Field Strain Analysis for Tab Selection

Fig. 2-3 shows the strain maps results for $0°, 30°, 60°\ and\ 90°$ fiber direction laminates with both glass and carbon tabs. Since, the ultimate tensile strength (σ_{UTS}) is used as a parameter for comparing each set of specimens, the DIC images related to 60%, 80% and 100% of σ_{UTS} for a given laminate are presented which correspond to strain maps during and just before the global failure respectively. This selection of stresses ratio enables the comparison of laminates under same load carrying capability and durability, hence preventing any misinterpretation of data if comparison was made under the same stress value.

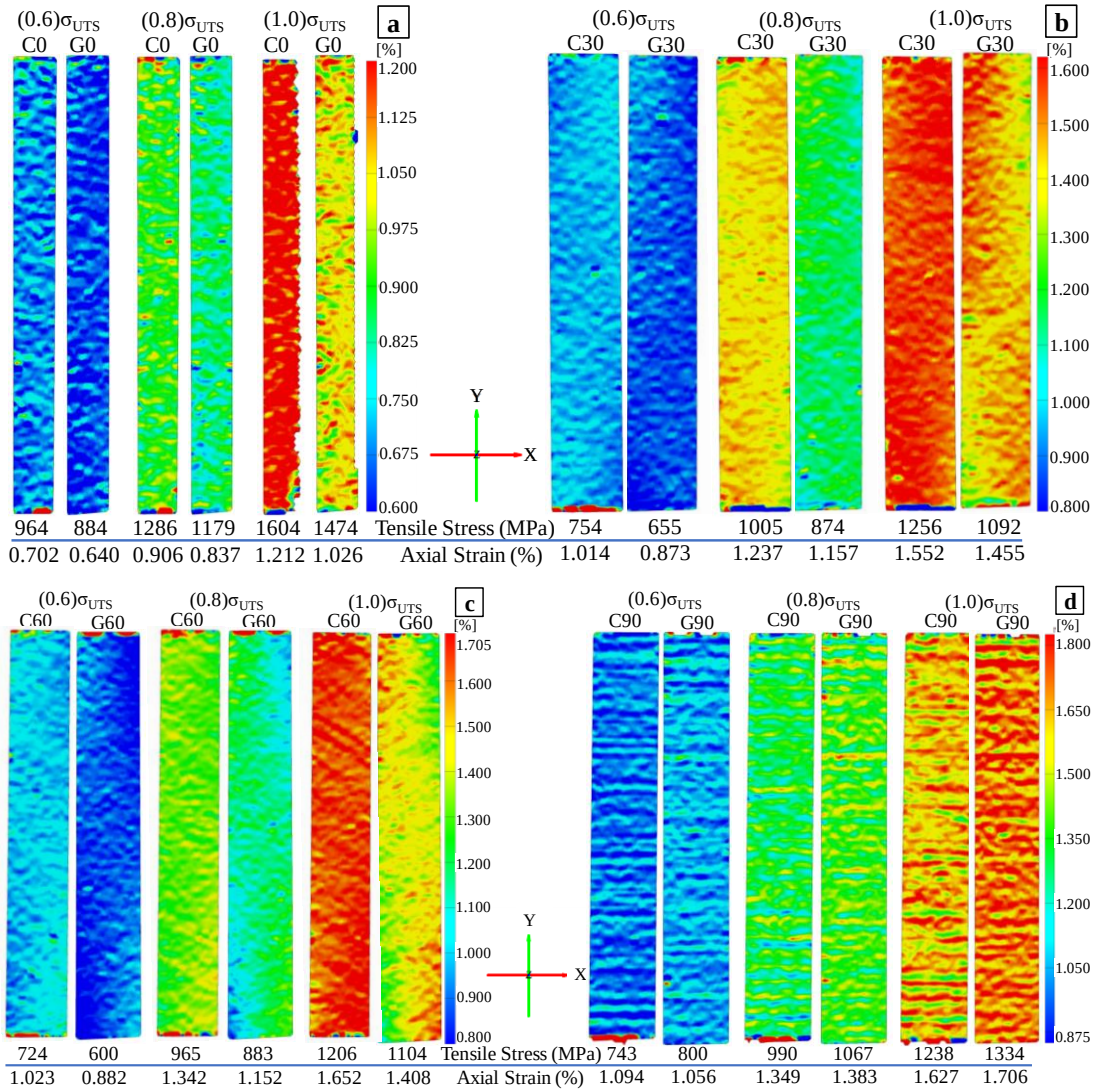

Fig. 2-3. Axial strain (ε_{yy}) field maps at (60, 80, 100)% σ_{UTS} for (a) C0 & G0, (b) C30 & G30, (c) C60 & G60, and (d) C90 & G90

Fig. 2-3(a) demonstrates the results of axial strain, i.e. ε_{yy} at various stress levels for laminate with 0° fiber configuration. In all the images, there are axial strain gradients in transverse direction, which bespeaks the occurrence of transverse damages during tests. As seen at 60% of ultimate tensile strength, the sample with carbon tab is at higher stress and strain level and has a more heterogeneous strain field throughout the gauge length. First opinion for this observation implies that there are various regions with high stress concentration for sample with carbon tab. However, at higher stress ratio, this heterogeneity disappears for sample with carbon tab and emerges for the other sample i.e., with glass tab. It is clearly seen that at 80% of σ_{UTS}, the specimen with glass tab has more diverse strain field map. This patchy appearance of strain field suggests that glass tab is not transferring the load competently to gauge length of tensile sample as compared to sample with carbon tab, thus resulting in increase of both axial and transverse strain gradients at various regions

of gauge length. Eventually, as seen for 100% of σ_{UTS}, the specimen with carbon tabs has almost uniform strain field while the sample with glass tabs indicates a wide range of strain values with certain stress concentration region. The result of this observation is that using carbon tabs provides a method to involve all material volume at gauge length, thereby enabling laminate to withstand higher stress levels. On the contrary, utilizing glass tabs hinders effective transfer of load to gauge length, and thus, stress concentration regions initiate major damages at gauge length and global failure. This observation creates some controversy regarding previous findings in literature that suggest usage of less stiff tabs for any fiber reinforced polymer composite laminates [31].

Fig. 2-3(b) also shows the strain map for 30° fiber configuration with both tab selections. None of the specimen show a significant pattern in full field strain measurement at 60% of σ_{UTS}, meaning that the strain distribution seems to be homogeneous and uniform. At higher stress value of 80% of σ_{UTS}, it is observed that strain values start to increase from edges of specimen at top and lower half of samples and advance towards the opposite edge of sample. This behavior is mainly associated with damage accumulation at plies with inclined fiber orientation i.e., 30° and transverse damage development. At final stage of loading, 100% of ultimate tensile strength, the strain field of sample with carbon tab is almost uniform and minor strain heterogeneity is seen at gauge length which indicates proper load transfer from tabs to laminate and contribution of all material volume in bearing the load. On the other hand, at 100% of ultimate tensile strength, the sample with glass tab shows the same strain trend of high strain at edges as it was initiated at lower stress levels, therefore demonstrates inefficient transfer of load from tab region to gauge length. Fig. 2-3(c) shows a very similar failure behavior and strain field map evolution for laminates with 60° fiber orientation plies. It is vividly seen that for sample with glass tab, corners of gauge length at 80% of σ_{UTS} demonstrate high strain regions, while this behavior is very insignificant for the specimen with carbon tab. This observation indicates the ability of carbon tab material to transfer load uniformly to gauge length of sample, thus showing a homogeneous strain filed at 100% of σ_{UTS}.

Fig. 2-3(d) shows a very diverse result compared to that of $0°, 30°, 60°$ configurations. It is seen that at 60% of σ_{UTS}, both samples with glass and carbon tabs demonstrate vivid transverse strain gradient patterns, which remain till final stage of test. This pattern of transverse variation of axial strain field was expected due to presence of 90° plies. Recalling that carbon fiber tab at final stages of loading in Fig. 2-3a-c gave a relatively uniform strain

distribution across the gauge length compared to glass tab, in this case, reverse observation is noted. As seen at 80% and 100% of σ_{UTS}, sample with carbon tab has more heterogonous strain map, which indicates presence of sharp stress concentrations at certain region of gauge length. Contrary to sample with carbon tab, gauge length of specimen with glass tab has smoother gradient of strains, and therefore full length of material is almost at same stress level. This observation is also consistent with data in Table 2-4 in which samples with glass tabs had less standard deviation compared to specimens with carbon tabs for 90° fiber configuration laminates.

It is evident from full field strain maps that carbon tabs provide better results for tensile tests if the configuration of plies is close to loading direction. On the contrary, it is seen that glass tabs give better results for laminates with off-axis plies closer to 90 degrees, which is consistent with the previously introduced argument in relation to stiffness variation. DIC images show that the same laminates with different tabs can withstand higher stress levels due to more uniform strain distribution. This observation is directly related to damage accumulation inside material, significantly influenced by the type of the tab material. Using acoustic emission analysis as a tool for scrutinizing failure types and their evolution is an add up to support and confirm results of mechanical tests and DIC analysis.

Typical failure images for one set of specimens (C0 & G0) are shown in Fig. 2-4. The failure mode in C0 sample is *explosive at gauge middle* (XGM) according to ASTM D3039 standard which suggests that stress concentration at gauge length region of the sample [48]. As for G0, the failure is in the form of *long splitting at middle of the gauge* (SGM) in longitudinal direction of the specimen where the failure seems to be initiating near the tabs [48]. According to Lavoie et al., the splitting in unidirectional laminates show a brush-like fracture morphology, and they stated that confinement of unidirectional plies between 90° or ±45° layers could reduce the severity of splitting [22]. The presence of end tabs with ±45° orientation in this study is assumed to lead to a have similar effect in progress of splitting whereby it can be said that carbon tabs have perfectly inhibited coarse splitting and distributed strains uniformly all through the gauge length.

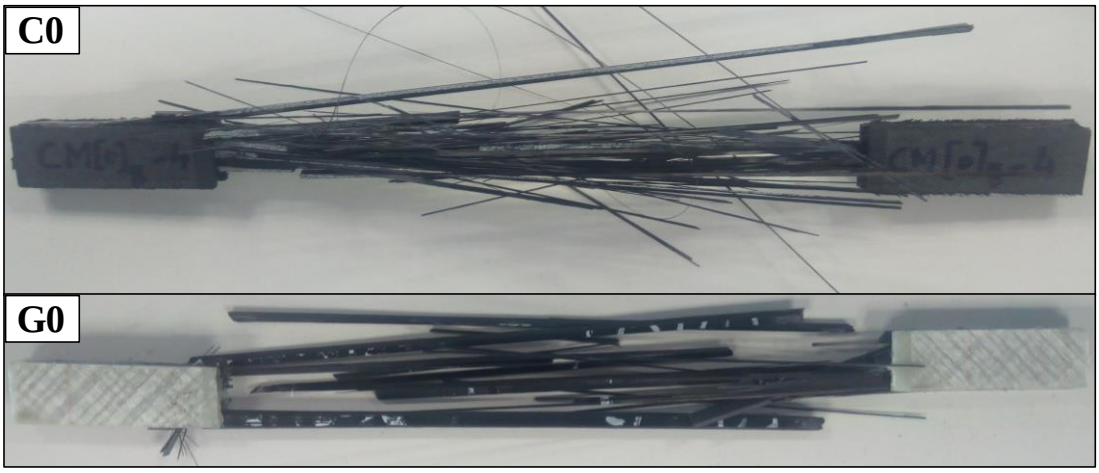

Fig. 2-4. Typical failure for C0 & G0

2. 4. 3. Damage Accumulation through Acoustic Emission Analysis

Fig. 2-5a &c, 8a & c present stress-strain curves based on the strain data of DIC images for samples with 0°, 30°, 60° and 90° fiber configurations respectively. The type of tab material associated with each curve is indicated at legend of Figures. The Fig. 2-5b &d, 8b & d show the accumulation of acoustic emission energy due to damage build up in laminates under tensile loading. In these figures the horizontal axis of plot namely, time is consistent with the strain axis of stress-strain curve above it. So, the energy released at any moment during tensile test can be attributed to the corresponding strain value. The type of end tab material and lay up configuration in these energy accumulation plots is indicated in their legend. The comparison of stress-strain curves of the specimens with carbon and glass fiber tabs reveals that there is a good initial consistency in mechanical response (stiffness) of every single laminate type regardless of tab material used. But as seen in Fig. 2-7c some erratic behavior (rapid variations) is observed for sample with 90° plies configuration and carbon tab material at stress value of above 500 MPa. This instability in strain measurements is attributed to hasty surface strain variations at gauge length which was observed as heterogenous strain maps in DIC measurements. Despite this disparity in strain measurement, overall response of 90° laminate is visible and distinguishable when carbon tabs are used.

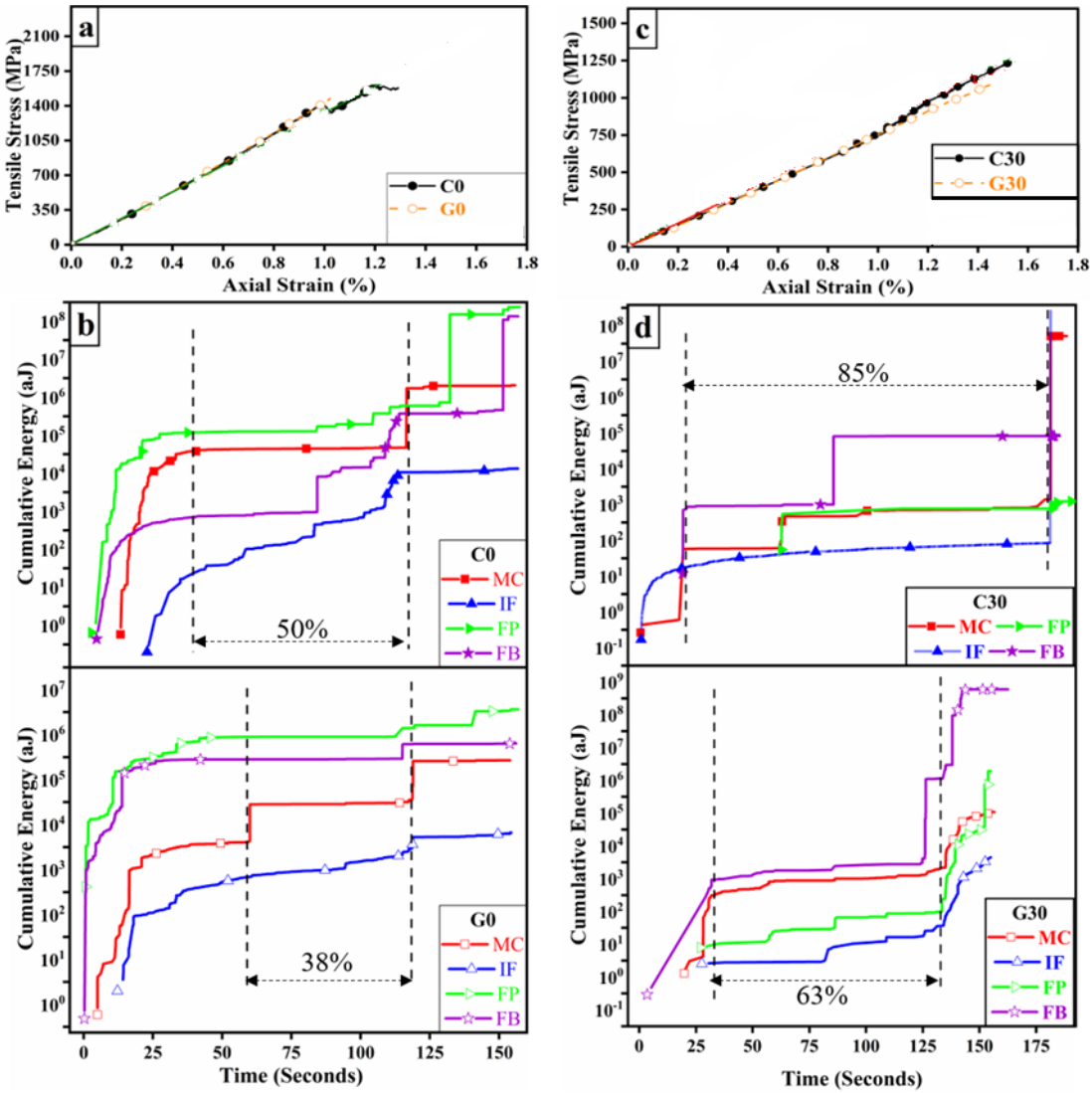

Fig. 2-5. Comparison of stress-strain curve and AE data for ((a, b) C0 & G0) and ((c, d) C30 & G30) (MC-Matrix cracking, IF-Interface failure, FP-Fiber pullout, FB-Fiber breakage)

Fig. 2-5b & d, Fig. 2-7b & d show the cumulative energy dissipation through acoustic emission process inside the laminates for associated laminates at the plots above them, therefore any abrupt changes in acoustic emission energy release rate can be attributed to the stress and strain level of which major damages happen under monotonic loading conditions. Three distinct stages of damage accumulation are distinguished for tested laminates as below:

1. Initial upsurge of acoustic emission energy in all laminates which signifies the initiation of new micro damages inside material and development of inherently present flaws at composite, such as manufacturing defects [49]. At this stage rate of energy release almost levels off i.e., the frequency of failure occurrence decreases drastically.

2. This stage is the longest period of loading regime in which acoustic emission energy release rate becomes almost negligible i.e., most damages stop building up temporarily. This reduction in energy release can be either due to crack arrest or change in the path of growing cracks which results in very small energy dissipation [50]. Growth of major cracks can be hindered when their tip reaches micro pores inside laminate and/or branching of the present cracks into minor cracks. During this material is exposed to momentary relaxation which causes strain gradients to appear between damaged and intact regions of the sample. The appropriate tab material can transfer load to larger volume of intact material through the gauge length and give more time for relaxation (i.e., uniform strain field throughout the gauge length) and thus increases the size of second stage.

   According to the previous study by authors transverse matrix cracking can directly degrade stiffness of fiber reinforced laminates, therefore it can be considered as a parameter for structural health monitoring of the laminates [43, 51]. Thus, initial level off point for matrix cracks is considered as the start point for second stage of tensile response in these laminates.
3. Third step of energy release due to acoustic emission is associated with global failure of the samples and huge increase in acoustic emission energy. It should be noted that since failure of surface plies in laminates with $60°$ and $90°$ layups is matrix dominant, first plies to fail are at surface of composite. This early failure at surface causes detachment of piezoelectric sensors from the sample at final stage of tensile test, therefore sudden energy release during global failure is not recorded completely.

Fig. 2-5b shows the acoustic emission behavior of C0 and G0 samples over time. The length of second stage for C0 specimen is almost 50% of total lifetime during tensile test while this step for G0 sample is 38%. Higher duration for C0 specimen signifies global failure of composite is delayed and carbon tab performs better compared to glass tab. This observation is consistent with the observation of DIC in Fig. 2-3a, since delay of failure development in the material corresponds with uniform distribution of load all through the gauge length i.e., C0 sample has more uniform strain distribution compared to G0 specimen at final stages of loading. As seen in Fig. 2-5b acoustic emission activity continues despite the absence of experimental strain data in Fig. 2-5a, this mismatch between mechanical response and acoustic energy release is related to major damages appearing at surface of sample which faces to DIC cameras. The damages deteriorate surface component defined on the materials surface to be analyzed through DIC, therefore no further data is processed by full field strain

measurements. It is noteworthy that despite very similar stress-strain results for C0 and G0 samples, combined usage of DIC obtained strain maps and acoustic emission analysis reveals a quite hidden fact about the end tab.

Fig. 2-5c shows the comparison of stress strain curves for laminates with 30° configuration. For C30, the change in the slope of stress-strain curve around 1% axial strain is consistent with acoustic emission energy release corresponding to the major fiber breakage (80 seconds after test initiation). C30 sample has 85% of its lifetime in second stage while G30 laminate has shorter second stage equal to 63% of total test length, therefore carbon tab enables distribution of load throughout the laminate and evens out the strain field at gauge length as observed in DIC results in Fig. 2-3b. To understand the unusual increase in stiffness of C30 sample at 1% axial strain, out of plane displacement of surface is analyzed using DIC images. As seen in Fig. 2-6 at top left corner of the gauge length positive displacement in out of plane direction occurs up to 0.05 mm. This displacement is related to a delamination at surface layer of sample which grows towards the middle of sample. According to a previous study, interlaminar shear and normal stresses are produced when in-plane loads are applied at a composites with tapered geometry (i.e. end tab region for tensile samples) [52]. These delaminations will coalesce with matric cracks and eventually cause premature failure of sample.

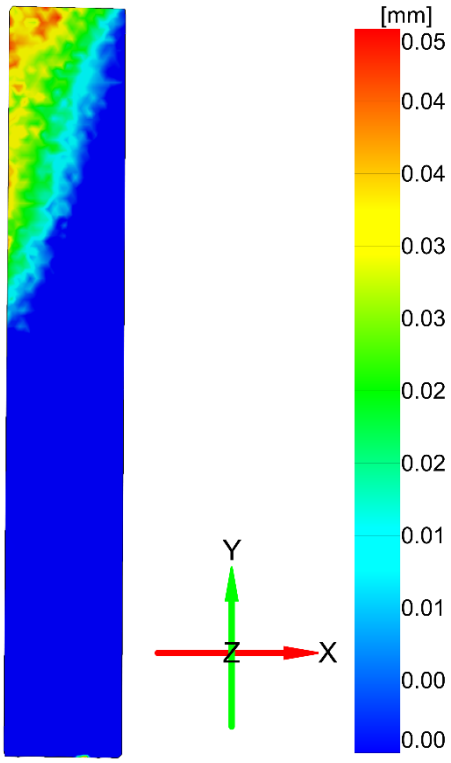

Fig. 2-6. Out of plane displacement showing delamination for C30 sample

Fig. 2-7a presents the stress strain curves with different tabs for laminate with 60° configuration. The comparison of acoustic emission energy dissipation for the two sample shows that the second stage for C60 specimen is longer, 89% of total test duration, which allows larger volume of material to bear the applied load as already observed in
Fig. 2-3c. On the other hand, G60 sample has only 58% of its test duration at second stage, therefore indicating that using carbon tabs is better when compared to glass tabs for this laminate configuration.

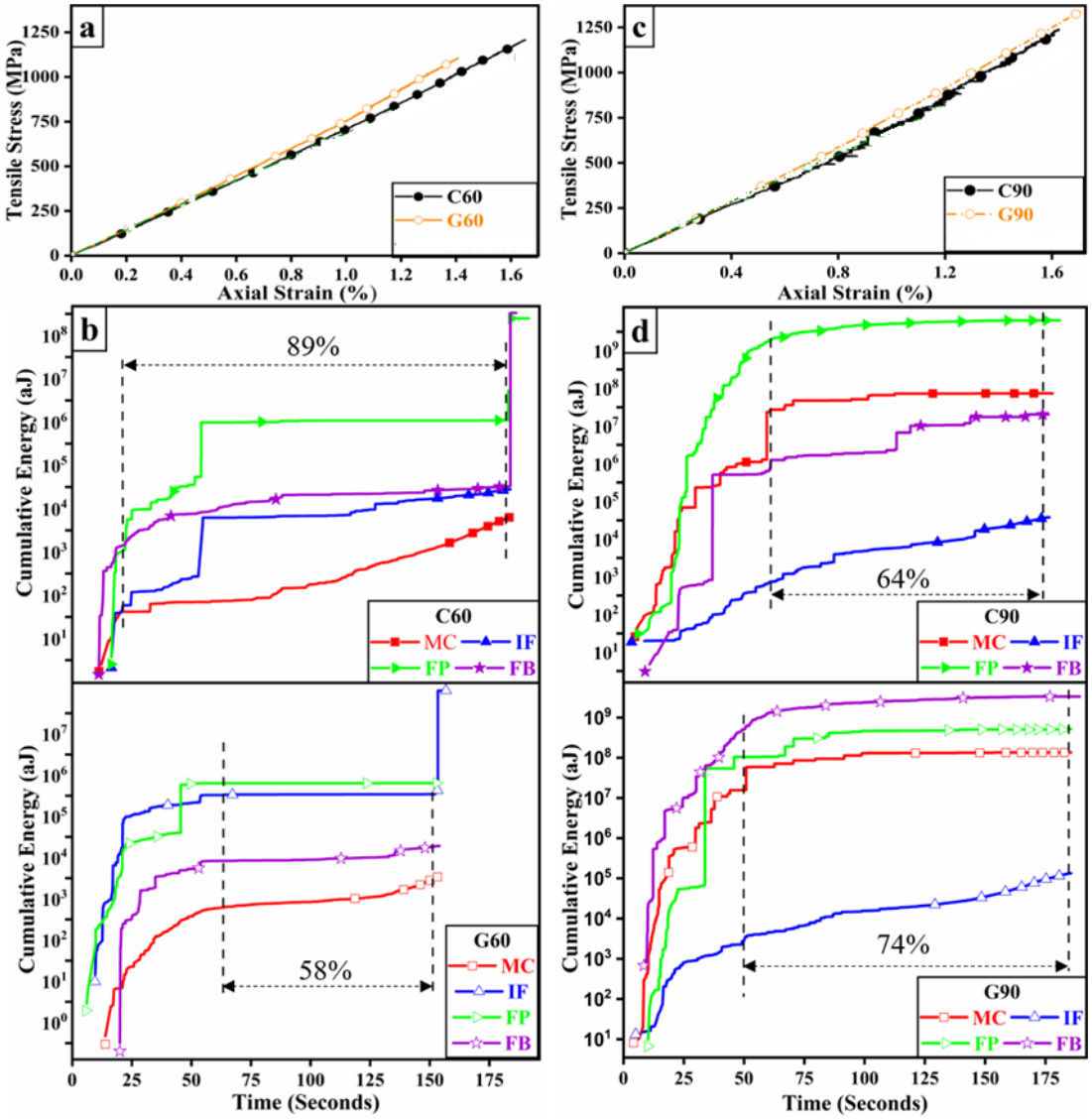

Fig. 2-7. Comparison of stress-strain curve and AE data for ((**a**, **b**) C60 & G60) and ((**c**, **d**) C90 & G90) (MC-Matrix cracking, IF-Interface Failure, FP-Fiber Pullout, FB-Fiber Breakage)

Fig. 2-7c shows the mechanical response of laminate with 90° fiber plies. Presence of 90° layers cause matrix dominant failure for the laminates, thus failure strain for C90 and G90 specimens is similar. As seen in Fig. 2-7d for the sample with carbon tab 64% of lifetime during tensile test is at second stage, hence it will have a wider range of strain distribution

at final stages of loading as seen in Fig. 2-3d. On the other hand, intermediate stage for specimen with glass tab is 74%, therefore its axial strain map will provide narrower strain values as seen in Fig. 2-3d. This behavior is expected since glass tabs are more ductile compared to carbon tabs and behave closer to matrix dominant 90° plies. Once again coupled analysis of DIC and acoustic emission has demonstrated quite different behavior of C90 and G90 samples despite their very analogous stress-strain curves.

Overall, it is evident that selection of tab material has a direct effect on damage accumulation trend in carbon fiber reinforced laminates. Tab materials that can introduce longer periods at second step of tensile loading conditions are preferred since they give less scattering in laminate strength results and give more uniform strain filed throughout the gauge length. For laminates with uniaxial orientation or with angles close to loading direction carbon laminate tabs are better choice. On the other hand, for samples with large off axis fiber directions such as 90° plies it is recommended to use glass tabs, as they provide better strain distribution and shallower damage development under tensile loading conditions.

2. 5. Conclusion

CFRP laminates with various stacking sequences are tested under tensile loading conditions and two different tabs types are used to distinguish the effect of each tab type on tensile behavior accordingly. Preliminary analysis of tensile tests reveals that utilizing carbon tabs can give less variation in tensile strength of laminates with 0°, 30°, and 60° plies, hence introducing more reliable results. Full field strain measurement images obtained by DIC system during tensile tests verifies that carbon tabs are better for abovementioned laminates. The results show that at final stages of tensile test for laminates with 0°, 15°, 30°, 45° and 60° ply configuration carbon tabs provide a more uniform strain gradient at the gauge length while the glass tabs result in a heterogeneous strain field. On the contrary to previous laminates, results of strength for laminates with 75° and 90° fiber orientation plies show less scattering of data when glass tabs are employed. The same procedure of analysis based on DIC technique shows that due to presence of off axis laminae with fiber direction normal to loading, various transverse strain gradients are visible in strain map therefore failure is controlled by matrix material. Strain distribution is more heterogeneous when using carbon tab therefore it is favorable to use glass tabs for this laminate. These DIC results imply that

smaller difference between elastic modulus of tab material and test material result in a uniform strain distribution under tensile loading condition. More investigation is done through AE energy release and defining three distinct steps of damage evolution inside laminates. Evolution of the AE energy results shows the damage accumulation rate inside the laminates under tensile loading condition. On the other hand, the regions vulnerable to damage development can be attributed to the regions with high strain gradient as their stress concentrations are high. As the rate of damage accumulation becomes larger i.e., shorter step in second stage of AE energy release, the more intense regions with strain gradient will be expected during loading. On the Contrary, if the damage development is slow i.e., longer second step in AE energy release, the material shows a relatively uniform strain field and will demonstrate higher failure strain. This means that the sample with slower damage development according to AE results, will be more uniform in strain distribution and will show higher strain at failure. Since the main physical difference between samples of same laminate has been the tab material, it is perceived that tab material influences the damage advancement in gauge region. For 0°, 15°, 30°, 45° and 60° ply configurations mechanical response of carbon tab is close to the sample itself due to akin values off elastic modulus. On the other hand, for laminates with 75° and 90° ply configuration glass tab performs better due to closer elastic modulus as to the sample. More in-depth analysis shall be conducted to find the mechanism behind different tab influence in damage accumulation, however, it is evident that combined usage of DIC and acoustic emission analysis can reveal the best choice of material as tab for tensile tests of composite laminates.

CHAPTER 3. INVESTIGATION ON INTERLAMINAR DELAMINATION TENDENCY OF MULTIDIRECTIONAL CARBON FIBER COMPOSITES

In this investigation carbon fiber reinforced laminates with different orientation layups are prepared and studied under tensile loading condition. Multiple strain measurement techniques, namely, resistive strain gauges, embedded optical sensors and digital image correlation are used to analyze stress-strain behavior simultaneously through the thickness of composite materials, and to determine the sequence of failure in different plies. Inconsistencies of strains measured through different methods is correlated with the tendency for interlaminar delamination, therefore demonstrating the ability of multi-instrument approach to describe damage progress through the thickness of multidirectional laminates. Complementary analysis through acoustic emission methods reveals that the angle of off-axis surface plies can influence the sequence of failure under tensile loading condition, and damage monitoring capabilities of acoustic emission system is directly affected by delamination tendency of surface plies. Remarkably, the delayed failure of off-axis plies is shown to be related to reorientation of these layer towards loading direction using infrared thermography method.
Keywords: Multi-Directional Laminates; Digital Image Correlation; Acoustic Emission; Strain Measurement; Thermography

3. 1. Introduction

Fiber reinforced plastics (FRP) have been extensively used in critical structural applications such as wind turbine blades, marine, aircraft and automotive components during the past few decades due to their higher specific strength and stiffness as compared to the metallic counterparts. The anisotropic nature of the FRPs further signifies their utilization which

helps to tailor their mechanical properties in accordance with the in-service predicted loading conditions. One of the approaches to facilitate such pertinent applications is to use multidirectional angle ply laminates so that the mechanical properties of the composite components in an engineering structure can be customized [53]. The design flexibility that can be achieved by using multidirectional angle ply laminates is usually accompanied with intricacy in damage types and their development procedures.

Damage initiation and propagation in fiber reinforced composites is an extremely complex process. Particularly, in case of multidirectional (angle ply) laminates, the presence of off-axis plies further complicates the process of damage origination and accumulation, thus implying that the failure types and their severity will be dependent on loading condition and material configuration i.e., lay-up of the laminate. Considerable experimental and analytical research has been dedicated to study the failure modes in multidirectional fiber reinforced composites [2-6]. Due to the presence of two constituent in FRPs, various failure modes either induced by matrix or fiber can exist in multidirectional angle ply laminates. In particular, Johnson et al. experimentally identified four major types of matrix induced cracking namely matrix microcracking, delamination, angle ply edge delamination and mode I delamination in multidirectional laminates under uniaxial tension. They showed the dependence of the active failure modes on the ply orientations [2]. Amara et al., presented an analytical study on $[\pm\theta_n/90_m]_s$ angle-ply laminated composites ($\theta = 0°$ to $90°$, n = 1 to 4, m = 1 to 4) to show the dependence of degradation in mechanical properties on the ply orientation, and the number of cross and off-axis plies during an uniaxial tension test [3]. More recently, Yuan et al. experimentally studied the active failure modes (fiber breakage, delamination, and transverse matrix failure) in angle ply laminates under tension and predicted their behavior using finite element method. In their findings the failure modes in a laminate were not only dependent on the ply orientation but also on the ply thickness and fiber volume fraction. For instance; in case of a laminate with 15° angle plies, the active failure mode transferred from an extensive fiber failure to a delamination dominated failure mode with increase in the fiber areal weight [5]. Overall, one can suggest that the first group of damages (i.e. matrix induced failures) include; microcracking, delamination (Mode I edge delamination, Mode II interlaminar shearing, and/or mixed mode delamination), angle-ply-induced edge delamination, and delamination migration which can coexist in the material while damage progresses [2, 54-56]. The matrix induced failures are usually predominant modes of damage development. However, fiber induced failures such as fiber pull-out and fiber breakage are also observed in these multidirectional laminates [47, 57, 58].

Delamination migration/relocation is crucial failure type among other matrix dominant failures, which initiates usually at the interface between two plies as an interlaminar delamination and then propagates as an intralaminar crack to the adjacent plies. This delamination migration behavior is dependent on the ply interface i.e., the directional mismatch between the adjacent plies, the interlaminar shear stresses, mechanical properties of the matrix material and, on the intralaminar crack progression [4, 6]. The delamination relocation could be observed as the propagation of a through the thickness crack. This crack either originates from a pre-existing split ply and joins up with/migrates to the adjacent plies or occurs without the necessity of previously existing ply splits through multiple kinking events [4]. The presence of multiple failure development modes and their coalescence requires in depth analysis of stress strain behavior specifically under tension loads.

A traditional stress-strain curve of carbon fiber reinforced plastics (CFRP) in tension is almost linear. It is practically impossible to obtain information related to the failure initiation and propagation merely using this curve. Furthermore, the traditional strain measurement techniques like mechanical extensometers and resistance strain gauges (SG) show several limitations, such as (i) inevitable removal of extensometer from the mechanical tester before the global failure, (ii) weak adhesion of a strain gauge to the surface of a specimen or removal of strain gauge from the specimen with surface ply delamination, and (iii) incapability to provide information about local strain gradients [59, 60] when utilized during a tensile test of FRPs. Therefore, to comprehensively understand and characterize the active failure modes (initiation and progression) in a laminate configuration, multi-instrumental experimental approach is better to be carried out during the mechanical test. Using non-destructive evaluation (NDE) techniques for such an approach will assist to recognize the in-service behavior of such multidirectional laminates in a thorough manner and give a better insight of strain evolution in local and global scale.

Utilizing NDE methods for laminated composites has gained substantial consideration over the past decade. A list of candidate techniques may include but not limited to Infrared thermography (IRT), Digital image correlation (DIC), X-ray computed tomography (CT) and Acoustic emission (AE). Single and multi-instrument NDEs arrangement is found to be employed to identify, characterize, and correlate failure in laminated composites (LCs) [41, 51, 61-64]. For CFRPs subjected to axial and transverse tensile loads, AE and IRT have been used complementarily to successfully correlate the failure modes [61] and also defined the specific sensitivity of each method regarding each failure mechanism [58, 62]. Cuadra et al. investigated the progressive damage accumulation in glass fiber reinforced polymer (GFRP)

composites subjected to static tensile and tensile-tensile fatigue loading utilizing a hybrid NDE system coupling AE, DIC and IRT. They also concluded that the cross correlation of these techniques permitted not only a more effective understanding of failure but also enhanced the reliability of each monitoring technique due to cross validation [63]. Oz et al., identified the high frequency AE events could correspond to a matrix crack by adopting multi-instrumental NDE approach coupling DIC and AE in case of a uniaxial tensile test for quasi-isotropic (QI) CFRP laminate, which also signifies the use of multi-instrument [64]. Beylergil et al. have used IRT and AE methods to reveal the effect of nonwoven polyamide-6,6 (PA 66) interlayers in increasing the interface strength of fiber-metal sandwich laminates [65].

As mentioned earlier, the inadequacy of the strain monitoring techniques through resistive strain gauges implies a necessity of utilization of alternative methods such as DIC or embedded Fiber Bragg's Grating (FBG) to observe strain evolution [9, 57, 59, 60, 66, 67]. DIC is a non-contact full-field displacement monitoring method which uses a high resolution charged coupled device (CCD) camera(s) to record series of images of a sample's surface having high contrast speckle pattern. The surface under the study is divided into several distinctive regions called "facets". Each facet region encloses subset of image pixels. Under a loading cycle, the facets on the speckle surface are tracked continuously which enable to record the progressive surface deformation. The consecutive deformed surfaces under the load are compared with the unloaded reference image utilizing a correlation algorithm to calculate full field strain. The average of the strains calculated at each facet point provide a global average strain value similar to the one obtained by a strain gauge [8]. As concluded, by Ajovalasit et al. for an off-axis unidirectional orthotropic lamina under uniaxial load; the misalignment of strain gauge and rotation of fibers towards the loading direction questions the precision of strain measurement recorded by strain gauge [59]. To answer this, Brunbauer et al recommended the use of DIC in a quasi-static tensile test after comparing the strains measured using DIC, extensometers, and resistance SGs for CFRP unidirectional (UD) laminates each having 0°, 45°, and 90° fibers. For the specimen with 45° fabric, the lower value of strain measured with SG as compared to DIC was attributed to the tendency of 45° to align with the loading direction [60]. In chapter 2, a good agreement among the average strain values from DIC and SG was achieved for various multidirectional CFRPs under uniaxial tension. But for laminate with 90° carbon fibers on the surface, transverse cracks on the surface deteriorated the speckle pattern resulting in sudden strain variations obtained by DIC [57]. Such a disadvantage of DIC method due to loss of speckle pattern quality with

an early surface failure of certain off-axis plies is a major limitation of DIC applications to FRP materials.

These superiorities and limitations related to each technique further aggravates the utilization of another strain measuring method, such as embedded FBGs, simultaneously along with DIC and SG for strain monitoring in LCs. FBGs have been widely employed as embedded sensors inside composite materials for evaluation of mechanical strain, residual cure strain, temperature, and pressure [9-11]. For unidirectional (UD) composites, embedded with an FBG, the strain values obtained from the FBG sensor during a tensile test matched perfectly with that of a strain gauge. While in case of angle-ply configurations, differences were found in the obtained strain values via both the methods [66]. Though a good agreement between the strains obtained from FBGs strain gauge is established for UD laminates, the effect of variation in grip pressure of a tensile machine could also result in the erroneous values of strains obtained through FBGs [68]. This has also been reported by Emmons et al. wherein they embedded FBGs sensors in the vicinity of grips where a higher pressure, exerted by the grips, resulted in incorrect strain measurements obtained from FBGs [67].

Author believes that this is the first comprehensive study to discuss the hybrid strain measurement results for multidirectional CFRP laminates using DIC, FBG and conventional SG techniques. Moreover, for the first-time failure modes occurring in the laminates are scrutinized through AE and IRT methods. In the first part of this investigation, materials and manufacturing technique of LCs are discussed and experimental procedure used for tensile tests is explained thoroughly. The next section describes the comparison of strain measurement results and discusses their results for their difference. Moreover, the results of damage accumulation through AE analysis are correlated with thermal images obtained through IRT monitoring. Finally, the concluding marks of the investigation are given at the end of the chapter.

3. 2. Materials

Pre-impregnated unidirectional carbon fiber (KOM10 T700 12KT UD300 37% 600 KOMP) is purchased from KORDSA, Turkey. This prepreg contained T700 type carbon fibers, having filament count of 12000, impregnated in epoxy resin available with a commercial name OM10. The areal weight of fibers and the content of resin is 300g/m^2 and 37% by

weight, respectively. Differential Scanning Calorimetry (DSC), DSC3 + Mettler Toledo was utilized to find the average glass transition temperature (Tg) to be 123 ± 2 °C.

3. 3. Experimental Procedure

3. 3. 1. Manufacturing of Laminates

A ZÜND G3-L3200 digital cutting machine and a manual hot press (MSE Teknoloji Ltd.) was utilized for cutting and curing of the CFRP prepregs, respectively, following the experimental procedure as explained in the chapter 2. The only difference in this case was that during the prepreg layup an FBG sensor was embedded within the central 0° plies. The same seven (7) layup sequences (symmetric and balanced) were considered, each containing eight (8) layers of carbon-fabric, as investigated in chapter 2. Table 3-1 shows the nomenclature of the laminate samples and layup sequences, with 0° fibers aligned to the axial direction. In sample ID, the pre-alphabet "F" represents the FBG (as these laminates were embedded with FBG sensor) while the number ahead of the alphabet corresponds to the angle of the off-axis ply.

Table 3-1. Samples names and layup orientations

Sample ID	Layup Orientation and Sequence
F0	$[0°]_8$
F15	$[15°/0°/-15°/0°]_s$
F30	$[30°/0°/-30°/0°]_s$
F45	$[45°/0°/-45°/0°]_s$
F60	$[60°/0°/-60°/0°]_s$
F75	$[75°/0°/-75°/0°]_s$
F90	$[90°/0°/-90°/0°]_s$

3. 3. 2. Mechanical Testing

In this chapter, tensile specimens were prepared (embedded with FBG sensor) in accordance with ASTM D3039 [1] standard and CFRP tabs were used to support the clamp locations of the tensile specimens, Fig. 5-1. The shape of the specimens was customized to support the FBG cable which otherwise was vulnerable to breakage during cutting of specimens as well as during the tensile test. It should also be noted that in chapter 2, the same laminates were

investigated and 6 tensile specimens from each laminate ware tested to optimize the procedure of tab selection. Based on which it was found that CFRP tabs show a better response as compared to GFRP tabs in tensile tests of such laminates. Therefore, in the present case a specimen, with embedded FBG, was considered from each laminate and CFRP tabs with the stacking sequence of $[45°/-45°]_{4s}$ were used to support the clamped locations. A resistance strain gauge was attached at the middle of one of the surfaces of each specimen following the procedure detailed in [57]. An INSTRON 5982 universal mechanical tester with a load cell of 100 kN was utilized to perform the uniaxial quasi-static tensile tests in displacement-controlled mode with a rate of 2 mm/min. All the tests were continued till the global failure of the specimens.

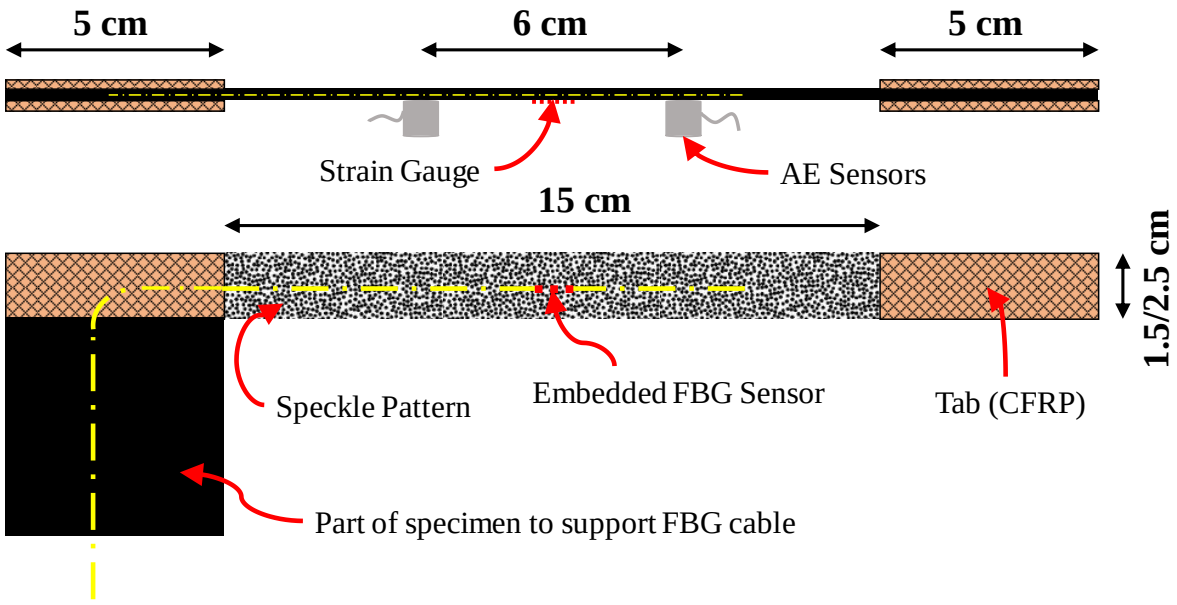

Fig. 3-1. Design of tensile specimen

3. 3. 3. Acoustic Emission (AE) and Digital Image Correlation (DIC)

Two AE sensors (6 cm apart) were attached to the same surface of the specimens where the strain gauge was adhered as shown in Fig. 3-1. The AE data was clustered based on a weighted peak frequency range corresponding to a specific failure type as depicted in Table 3-2. The opposite face of the specimens was speckle patterned for DIC measurements, Fig. 3-1. DIC, in present case, was specifically used for obtaining the average axial strain to be compared with that obtained from the strain gauge and FBG. Further details regarding the procedure of AE and DIC data acquisition and analysis that is used in the current study are already explained in detail in chapter 2.

Table 3-2. Weighted peak frequency range for clustering

Failure Mechanism	Weighted Peak Frequency (kHz) Range
Matrix Cracking (MC)	< 240
Interface Failure (IF)	240 – 380
Fiber Pullout (FP)	380 – 520
Fiber Breakage (FB)	520<

3. 3. 4. Infrared Thermography (IRT) and Fiber Bragg Grating (FBG)

An infrared (IR) camera (FLIR X6580sc), with a 50 mm lens, was placed at approximately 80 cm away from the tensile test specimen to record the surface temperatures of the specimen during the test. The IR camera has an operational temperature range from -20°C up to 3000°C with an accuracy of ±1°C. The sampling rate of 200 Hz was chosen to record the images at a resolution of 640 × 512 pixels. The recorded images were then analyzed with FLIR ResearchIR Max image analysis software.

Single FBG sensor, purchased from Technica SA, was embedded within the central 0° plies of each laminate. The gauge length and the Bragg's wavelength of the sensor were 1 mm and 1550 nm, respectively. To ensure the placement of FBG sensor at the middle of the tensile specimens' gauge length proper markings were made during the prepreg layup process. The Response of FBG sensors, during the mechanical tests, was obtained via a Micron Optics SM230 model interrogator at a sampling frequency of 1000 Hz and was saved by a Micron Optics Enlight Software. As strain is applied on composite laminate causes an elastic strain on embedded FBG, therefore change the Bragg wavelength λ_B of grating. This change in Bragg wavelength at constant temperature is related to mechanical strain ε_{app} as:

$$\frac{\Delta\lambda_B}{\lambda_B} = (1 - P_e)\Delta\varepsilon_{app}$$

Where P_e is the strain-optic coefficient of the fiber.

3. 3. 5. Set Up of Hybrid Evaluation Test

For conducting the tensile tests, the hybrid experimental setup was arranged as depicted in the schematic diagram in Fig. 3-2. To acquire the data from all the five techniques simultaneously, the proper arrangement of experimental setup was extremely crucial. The placement of equipment was done such that the speckle patterned surface of the specimen

seen directly by DIC and infrared (IR) cameras. While strain gauge and AE sensors were present on the opposite surface. It was also ensured that the DIC and IR cameras must be placed at such a distance from the specimen that, during the test due to the axial motion of the upper jaw of tensile machine, the top edge of the specimen should not disappear from the field of view of the cameras. The acquisition of data from all the instruments started at once with the beginning of the test and continued until the global failure of a specimens.

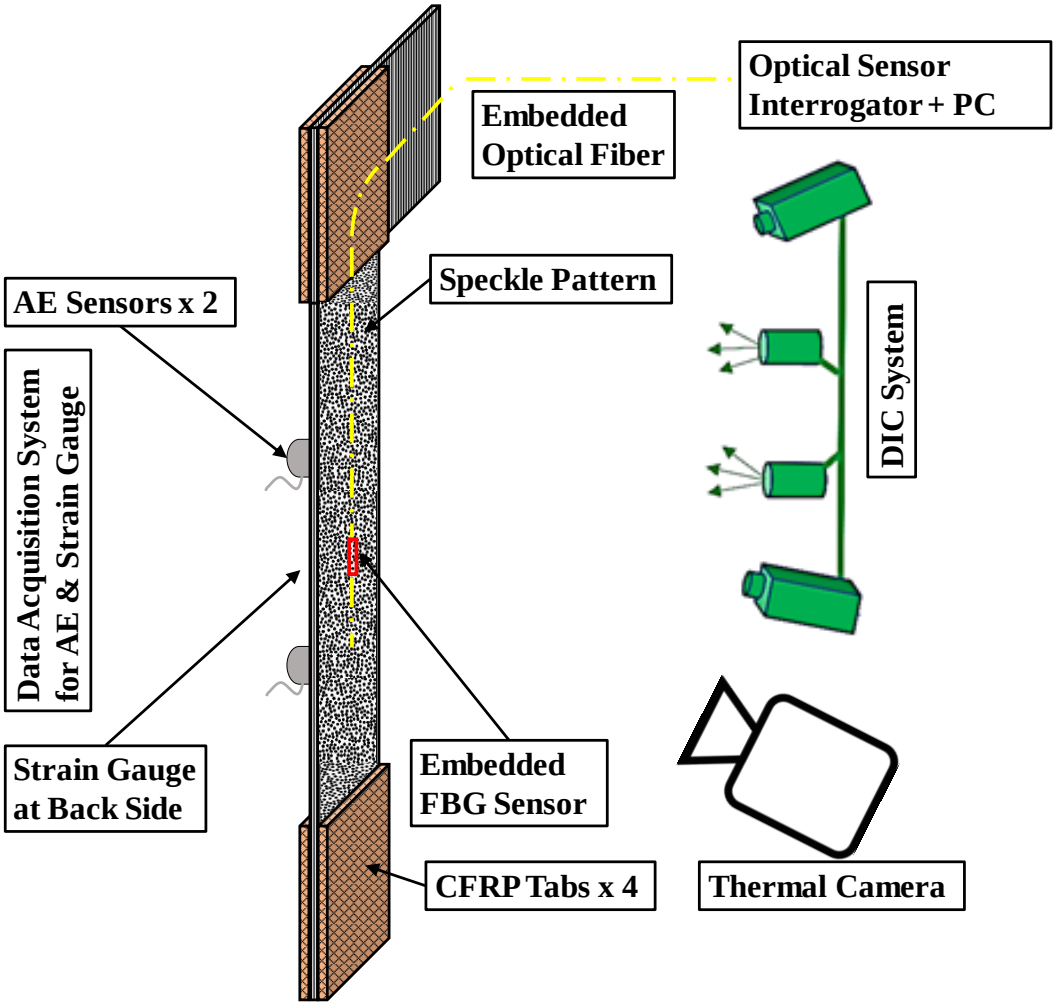

Fig. 3-2 Schematic of experimental setup

3. 4. Results and Discussion

Fig. 3-3 shows the stress strain curve obtained by Strain Gauge (SG), Digital Image Correlation (DIC) and embed Fiber Bragg Grating (FBG) for all the seven specimens. Overall a very good agreement is observed in values of strain obtained through various monitoring techniques.

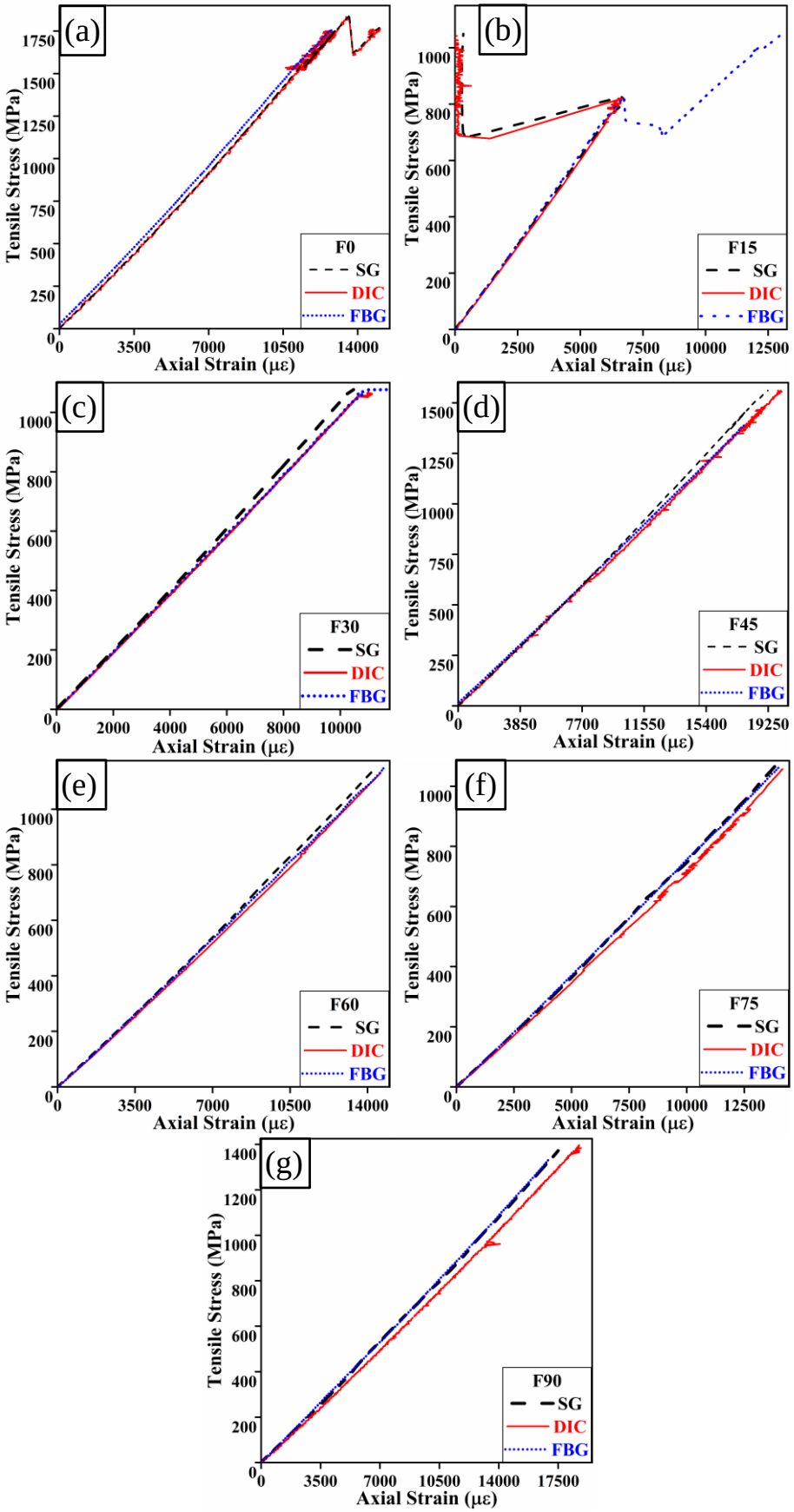

Fig. 3-3. Stress-strain curves (SG: Strain gauge, DIC: Digital image correlation, FBG: Fiber Bragg's grating sensor)

For further discussion, four samples namely, F0, F15, F45 and F90 are selected and scrutinized in detail through IRT and AE methods. The reason for choosing these 4 samples for detailed discussion is not only to examine the extreme and middle cases but also to analyze the remarkably distinct behavior of sample F15 as depicted in Fig. 3-3b. Despite the overall agreement, there exist few abrupt variations in the strain data obtained from various methods. Careful investigation of these variations by analyzing the IRT and AE data revealed either an acoustic emission activity or a temperature variation at those time intervals.

The stress strain curves obtained from different measuring methods for sample F0 **(**Fig. 3-3a) are in good agreement between different methods as the slopes of each curve are alike throughout the test. This consistency reveals identical tangent modulus value for F0 sample during tensile loading regardless of strain measurement technique. At higher stress levels of above 1500MPa, FBG sensor fails to record data while other measurement techniques continue to record the strain values until a sharp stress drop and thereafter a global failure of sample. This observation implies that the inner plies of the F0 specimen fail in advance of surface layers, however due to absence of delamination migration surface plies are preserved from damage propagation temporarily. Several studies conducted to analyze delamination migration between angled plies of CFRP laminates have found that if the direction of delamination front line at resin inter-ply region is aligned with the fiber direction of adjacent ply, then no interlaminar crack jump will occur [69]. It can be concluded that the interlaminar crack migration during damage development through delamination of inner layers in F0 specimen is not occurring, which preserves surface layers intact. Furthermore, presence of a temporary oscillation in DIC measurement prior to failure of FBG sensor shows the growth of an edge splitting as seen in thermal image of Fig. 3-5(i). This early damage at 98s (12006με) is associated with a sudden increase in total cumulative acoustic emission energy as seen in Fig. 3-4a. The energy dissipation that is measured by AE technique represents the amount of cumulative energy that dissipates during the progressive failure of the laminates which is hereafter mentioned as acoustic emission energy. In Fig. 3-4b the corresponding moment is marked as “i”, where matrix cracking, interface failure and fiber breakage occur simultaneously. The acoustic emission energy dissipation after these failures presents small increasing steps up to 13000με corresponding to maximum stress level.

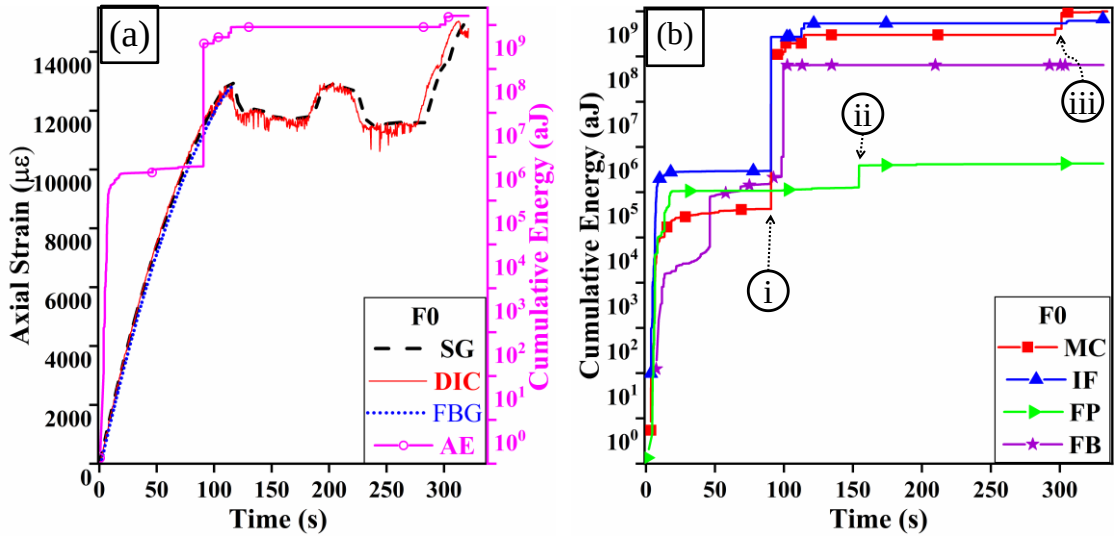

Fig. 3-4. (a) Total AE cumulative energy and axial strain with time for specimen F0 (b) AE cumulative energy of each failure mode with time for specimen F0 (MC: Matrix cracking, IF: Interface failure, FP: Fiber pull-out, FB: Fiber breakage). Note: Points (i), (ii) and (iii) are marked to show the AE activity at 98, 154.4 and 301 seconds corresponding to the thermograms shown in Fig. 3-5 (i), (ii) and (iii), respectively

At maximum stress level material loses its integrity and stress value drops, however the DIC and strain gauge continue to show consistent strain values with respect to each other up to global failure point. This period of lifetime for F0 sample shows no significant acoustic energy dissipation as seen in Fig. 3-4a and can be termed as the *semi-passive* stage of damage accumulation period. However, as seen in Fig. 3-4b at the moment (ii), a major incident related to fiber pull out is observed as per results of clustering acoustic emission hits. The corresponding thermal image as seen in Fig. 3-5(ii) demonstrates a secondary edge splitting behind the initial splitting observed in Fig. 3-5(i), which indicates lower tendency of interlaminar delamination jump in F0 specimen. An interesting observation for this second splitting is presence of a slight bending before complete fragmentation. This behavior eventually results in a pull out of this fragmented part from the bottom of the specimen and causes a considerable acoustic emission activity. Therefore, the thermal monitoring of specimen throughout the test show consistency of reliability of acoustic emission clustering and presents the advantage of hybrid monitoring systems. Another small damage that happens at semi-passive stage is matrix cracking which has been indicated as “iii” in Fig. 3-4b and its relevant thermal image is shown in Fig. 3-5(iii). Thermal image shows a significant temperature increase at top right corner of the sample which acts as a trigger for global failure of laminate and initiates consecutive splitting events at gauge length of the sample.

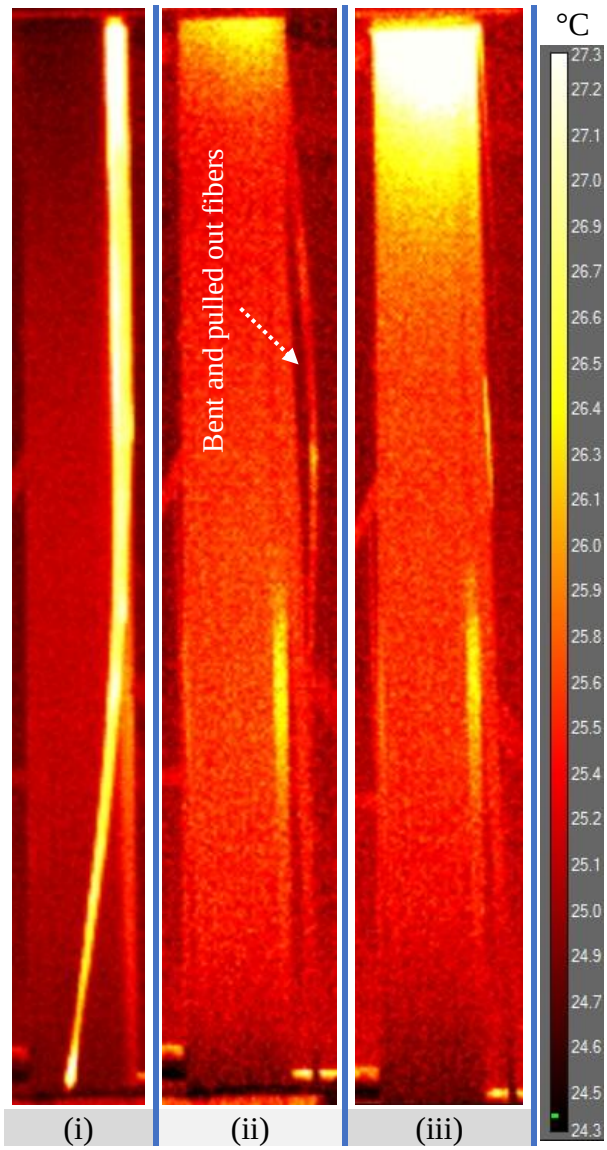

Fig. 3-5 Thermograms for specimen F0 at (i) 98 (12006με), (ii) 154.4 (11727με) and (iii) 301 (13825με) seconds corresponding to the points marked in Fig. 3-4b

As seen in Fig. 3-3b for F15 sample initial response of all strain measurement systems is similar and stress-strain curves match perfectly. However, at 800MPa surface angled plies fail since DIC and SG systems show a rapid drop in strain value to zero. Despite this initial failure, FBG sensor continues to record strain values and remarkably shows an increase in stress level, indicating capability of 0° plies at the core of sample to endure the applied tensile load. The sudden increase in strain values just after the failure of surface plies as seen in Fig. 3-6a is a result of the jerk in specimen [70]. Therefore, two main steps of failure development for this sample are early damage accumulation at surface plies and delayed damage progress into inner layers. The first step includes creation of various splits in off axis layers in which they cause delamination from free edges. An example of these delaminations that occur at the free edge of specimen is shown in thermal image of Fig. 3-7(i). As these delaminations

grow without creation of any major fiber breakage, they will cause a significant decrease in strength of material and consequent transfer of load to adjacent 0° plies.

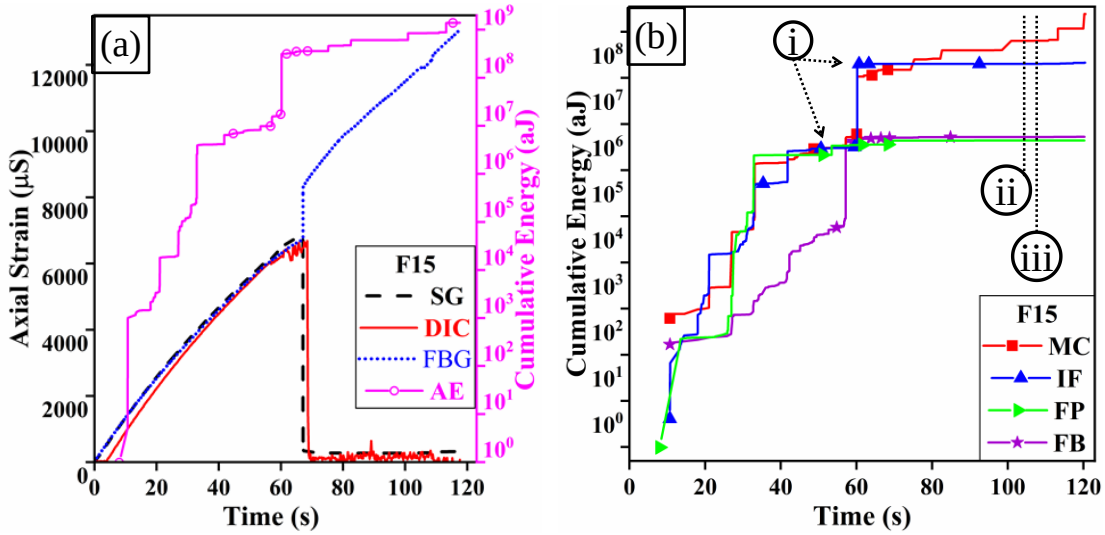

Fig. 3-6. (a) Total AE cumulative energy and axial strain with time for specimen F15 (b) AE cumulative energy of each failure mode with time for specimen F15 (MC: Matrix cracking, IF: Interface failure, FP: Fiber pull-out, FB: Fiber breakage). Note: Points (i), (ii) and (iii) are marked to show the AE activity from 50.8 to 61.3 seconds, and at 104 and 107 seconds corresponding to the thermograms shown in Fig. 3-7 (i), (ii) and (iii), respectively

The transfer of load from angled fiber plies after their failure to 0° layers is analogous to the behavior of load transfer in thin-ply fiber hybrid laminates, which can cause a pseudo-ductility behavior[71]. In these hybrid fiber laminates with pseudo ductile behavior, the energy release rate due to delamination is a critical parameter for successful transfer of load and prevention of catastrophic failure. In current laminate i.e., F15 the slow release-rate of interlaminar delamination can be attributed to lower tendency of delamination migration similar to the behavior seen in F0 sample. According to the findings of an investigation by Shi et al. possibility of delamination migration and multiple plane fracture for CFRP laminate with angle difference less than 25° between adjacent plies is very low [72]. The only difference between the F0 and F15 sample is the sequence of damage development from inner plies to the surface for the first case and surface to core layers for second laminate. This difference can be attributed to the weakness of off axis plies at surface layers which precedes any failure development in 0° plies. Acoustic emission analysis of F15 sample as shown in Fig. 3-6a shows a sharp increase shortly before the failure of the surface, which is readily distinguishable by DIC measurement fluctuation. However, SG measurements do not show any signifying data variation therefore, showing the advantage of usage of a global strain measurement technique for correct identification of failure onset point in the material.

Thermal image at Fig. 3-7(i) shows development of an inter-ply delamination between front 15° surface ply and its adjacent layer starting from left edge at upper section of the sample. This delamination is of adhesive type [58, 73] and shows a constant acoustic energy dissipation as indicated by “i” in Fig. 3-6b. As seen in Fig. 3-6b after the failure of surface plies acoustic emission activity continues just as matrix cracking, indicated as “ii” and no other failure type shows significant energy dissipation.

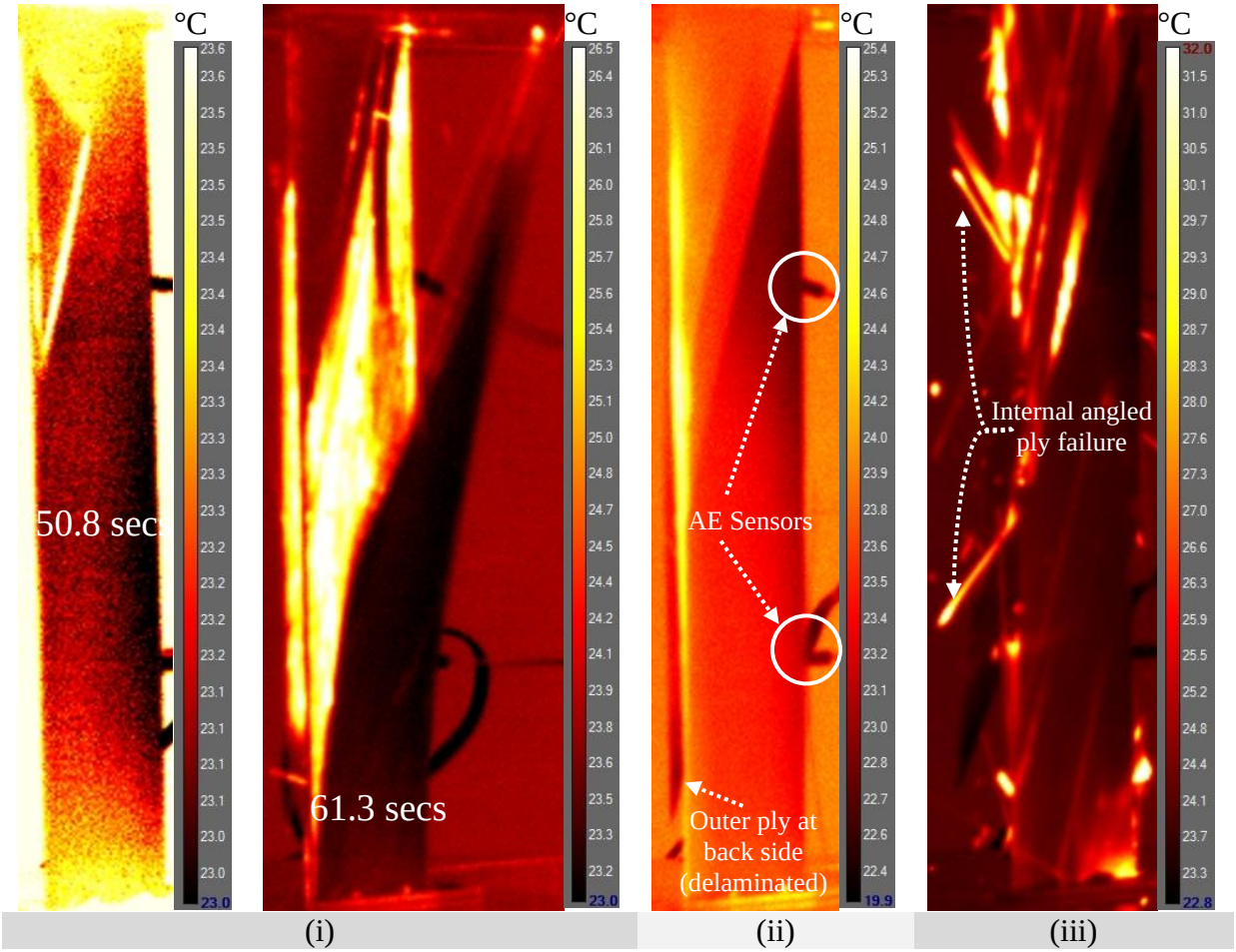

Fig. 3-7 Thermograms for specimen F15 at (i) 50.8 (5600με) – 61.3 (6453με) (ii) 104 (11855με) and (iii) 107 (11995με) seconds corresponding to the points marked in Fig. 3-6b

As seen in Fig. 3-7(i) and Fig. 3-7(ii) acoustic emission sensors are still attached to the back surface of F15specimen which has delaminated after initial failure of surface plies. This delamination has resulted in inadequacy of acoustic emission recording capability i.e., only acoustic emission data related to matrix cracking and interface failure are observed in Fig. 3-6b. Fig. 3-7(iii) indicates failure of -15° plies which are closer to midplane of laminate at final stages of tensile loading. This observation implies possible preservation of these off-axis plies sandwiched between 0° layers. It has been suggested that the failure mechanisms in multi-directional laminates involves crack initiation at off axis plies which develops into failed fiber clusters in adjacent 0° plies [74] and interlaminar delamination between off axis

layers and adjacent plies [43]. However, according to a recent investigation by Marthin et al. presence of hierarchical structure in which weaker interface material i.e., off axis plies, is surrounded by stronger interface material can have a shielding effect and prevent early failure of inner layers[75]. The delayed failure of -15° plies seen in Fig. 3-7(iii) can be related to same shielding effect of 0° layers.

As seen in Fig. 3-3d for F45 sample stress-strain curves obtained for various measurement systems shows good consistency at the beginning of test. At the 30th second of the test corresponding to 600MPa, surface strain measurement systems (SG and DIC) start to deviate from FBG results, thus indicating damage initiation and development at either surface or inner layers. As obvious form the stress strain curve of F45 (Fig. 3-3d), this initial strain data loss of the laminate is attributed to an earlier failure of FBG sensor thereby approving that the use of a strain measurement system located at 0° plies provides more conservative approach for failure analysis. This interesting observation also provides an indication of failure initiation from the inner plies. As seen in Fig. 3-8a no significant acoustic emission hit related to this deviation point is observed which implies that gradual reorientation of surface plies to align with loading direction is responsible for this mismatch onset. This ability to align with loading direction delays damage accumulation in surface plies and promotes damage initiation in 0° layers. This assumption is evident from the thermal images of Fig. 3-9(i) and (ii). It is clear that these damages cause longitudinal splitting at 0° plies, therefore providing an early failure of inner layers.

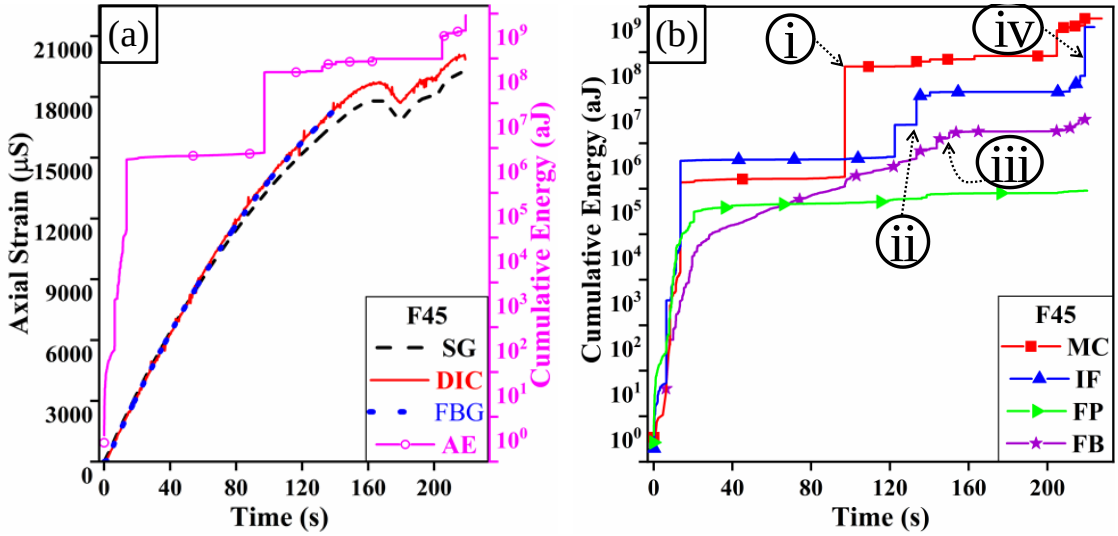

Fig. 3-8 Total AE cumulative energy and axial strain with time for specimen F45 (b) AE cumulative energy of each failure mode with time for specimen F45 (MC: Matrix cracking, IF: Interface failure, FP: Fiber pull-out, FB: fiber Breakage). Note: Points (i), (ii), (iii) and (iv) are marked to show the AE activity at 97, 133.5, 150 and 219 seconds corresponding to the thermograms shown in Fig. 3-9 (i), (ii), (iii) and (iv), respectively

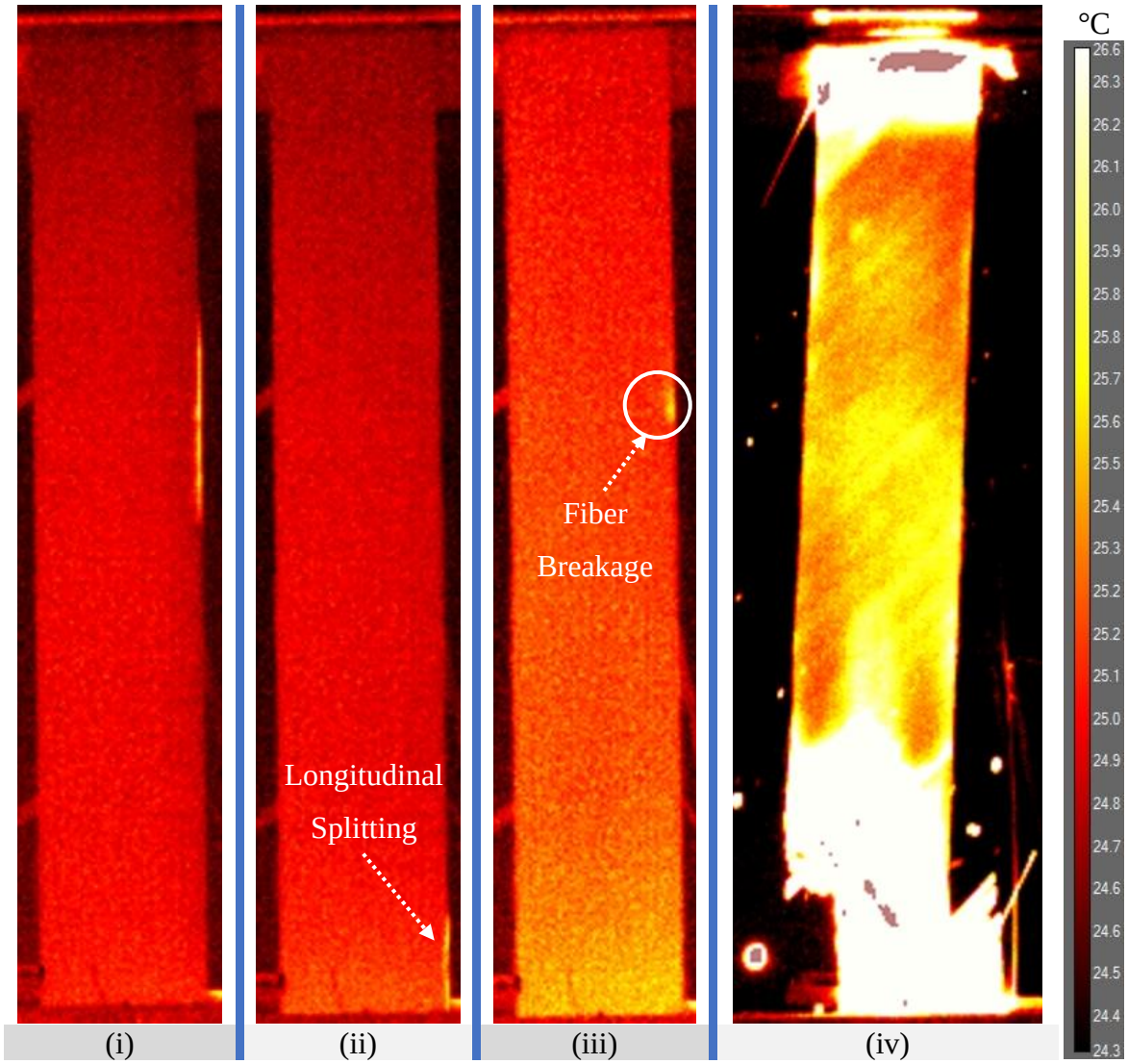

Fig. 3-9 Thermograms for specimen F45 at (i) 97 (13478με) (ii) 133.5 (16728με) (iii) 150 (17732με) and (iv) 219 (19539με) seconds corresponding to the points marked in Fig. 3-8b

Unlike previous laminates i.e., F15 and F0, the failure of one layer in F45 laminate is not followed by a subsequent load transfer and/or stress rise. It has been suggested that the presence of an angle more than 25° between the adjacent plies of CFRP laminates can result in an increase of Mode II interlaminar delamination energy release rate i.e. delamination migration [72]. This reason facilitates failure development between adjacent multidirectional plies and fosters creation of interlaminar fracture growth. Therefore, F45 laminate break apart without occurrence of any major off axis splitting at surface layers as seen in Fig. 3-9(iv). It is noteworthy to consider that alignment of off axis fiber at surface of F15 specimen occur faster as compared to F45 laminate. This easier reorientation of surface plies towards the loading direction in F15 laminate causes immediate damage accumulation in surface as splitting due to shear dominant failure. So reverse failure steps are expected for F15 and F45 samples. Comparing the thermal images shown in Fig. 3-9(ii) and (iii) with

corresponding marked points in Fig. 3-8b it can be said that the thermal activity due to longitudinal splitting depicts a line of high temperature area while fiber breakage causes an instantaneous high temperature point. Fig. 3-9(iv) shows the corresponding failure moment of sample at 219 second of the test. It is clearly seen that failure region at lower part of sample has developed in a transverse mode. This failure growth presents various delamination jumps through the thickness of this sample, therefore, indicating variation of failure mode with change in the orientation of fibers in plies.

Fig. 3-3g shows the stress strain curve for F90 sample obtained through various strain measurement techniques. From the initial moments of the test significant deviation in strain values through the thickness of laminate are observed. This early change in slope of curves is related to fast development of damages in 90° plies and increase of probability of failure in 0° layers [76]. Remarkably some of these transverse crack developments do not show a significant effect on strain values based on local measurements i.e., SG and FBG. However, full field strain measurement based on DIC can distinguish these damage developments. As seen in Fig. 3-10a and b acoustic emission energy dissipation over time show a gradual increase, i.e. small steps, which is typical for laminates with transverse fiber direction [57]. Stress-strain evolution is like F45 sample without load transfer between plies since all strain measuring systems fail simultaneously. This observation indicates presence of intraply crack growth and transverse failure morphology similar to the failures seen in woven fabric laminates[58].

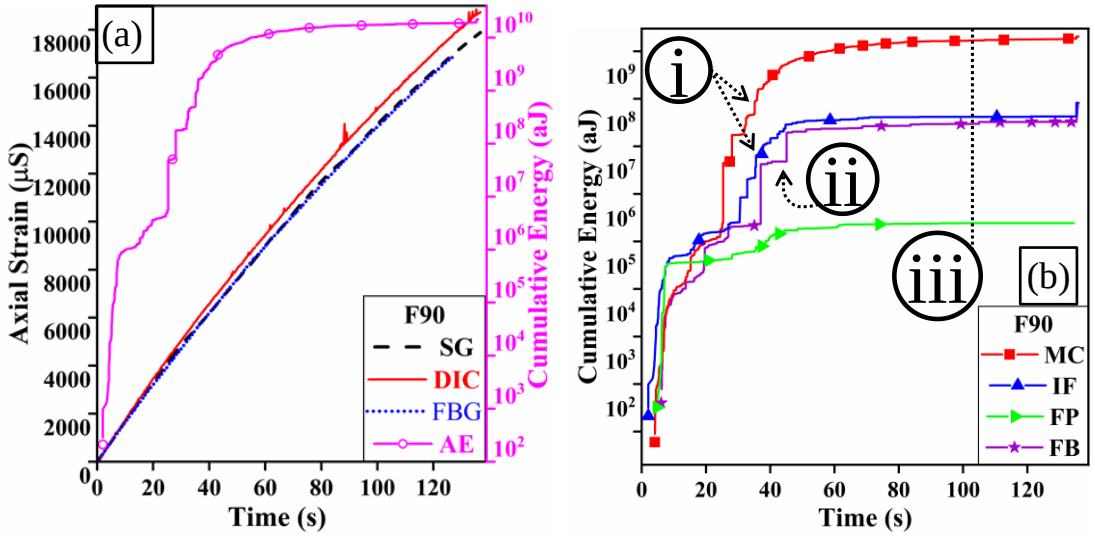

Fig. 3-10 (a) Total AE cumulative energy and axial strain with time for specimen F90 (b) AE cumulative energy of each failure mode with time for specimen F90 (MC: Matrix cracking, IF: Interface failure, FP: Fiber pull-out, FB: Fiber breakage). Note: Points (i), (ii) and (iii) are marked to show the AE activity at 35.4, 45 and 102 seconds corresponding to the thermograms shown in Fig. 3-11 (i), (ii) and (iii), respectively

Fig. 3-11(i) show initiation of a transverse crack from left edge of sample and its instantaneous growth through the width of sample. According to Fikry et al. transverse cracks in CFRP laminates with middle off axis plies start from edge and develop through the width to the other edge [77]. However as seen Fig. 3-11(ii) the initiation of another transverse crack occurs at the middle of sample width and grows to the edges of sample. This observation is not consistent with the findings of mentioned investigation which might be due to difference in stacking sequence and position of off axis plies in two studies.

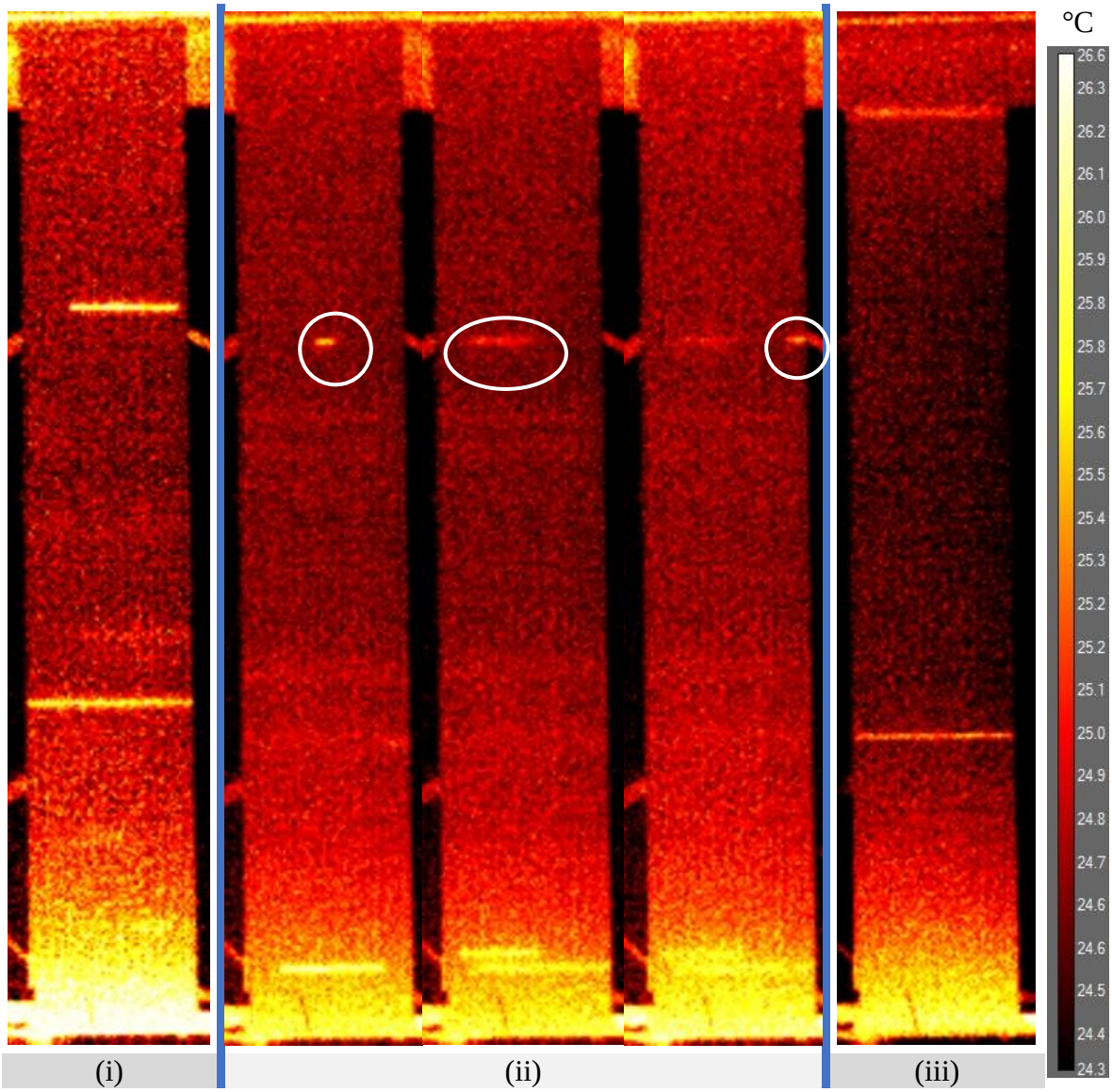

Fig. 3-11 Thermograms for specimen F90 at (i) 35.4 (5670με) (ii) 45 (7058με) (three sequential images) and (iii) 102 (15468με) seconds corresponding to the points marked in Fig. 3-10b

Thermal image corresponding to 102s (15468με) of the test reveals a transverse crack which does not show any relevant data obtained through acoustic emission or strain measuring

systems. This observation shows the advantage of using a hybrid monitoring system in detection of defects.

To summarize the observations obtained based on various damage monitoring systems and present the failure sequence for each laminate, Table 3-3 is provided as follows:

Table 3-3. Failure description for each laminate

Laminate	Failure Description
F0	Stress-strain curves for various measurement systems shows similar trend approximately up to the maximum stress. Despite the occurrence of several longitudinal splitting from the edges of the sample, the integrity of specimen is preserved till global failure.
F15	The first major failure of the material occurs at surface due to the edge angle ply delamination. However, the inner layers of the specimen remain almost intact and global failure of the sample occurs at higher stress levels.
F30	The global failure of the sample happens due to the rapid growth of an edge angle ply delamination. This delamination propagates through the thickness immediately after its initiation followed by the complete failure of the composite material.
F45	The microcracks along the fibers at surface angle plies are accumulated and result in matrix induced delamination at upper and lower parts of the sample as seen in thermal images. These delaminations grow rapidly and provoke global failure of the composite material.
F60	Sample failure occurs after the accumulation of matrix microcracking along the fiber direction at angled surface plies. Subsequent delamination of the surface plies is followed by an abrupt growth of crack through the thickness and global failure of the material.
F75	The failure starts similar to F60 sample through matrix micro cracks, however these micro cracks in surface layers occur at lower stress levels as compared to F60 sample. Micro crack initiation is also evident from early disruptions at DIC data. The micro cracks result in matrix induced delamination at the surface of the sample and consequent global failure of the material.
F90	From the very beginning stages of loading transverse matrix cracks at surface plies occur which are evident from early change of slope related to DIC in stress-strain curve. These micro cracks coalesce along the width of the sample as seen in the thermal images and sudden failure of the laminate takes place with the growth of macro cracks through the thickness.

3. 5. Conclusion:

The failure behavior of multidirectional CFRP laminates under tensile loading condition is monitored using DIC, SG, FBG sensor coupled with AE and IRT methods. A very good agreement in the values of strains is attained between different methods, however some discrepancies are seen which are well defined by using thermal camera and acoustic emission

analysis. The following conclusions are drawn on the benefits of utilization of hybrid strain monitoring and damage characterization techniques:

- For F0 sample, a *semi-passive* region for acoustic emission energy release is observed which is followed by an abrupt failure of sample through a sequence of longitudinal splitting. This behavior also presents lack of delamination migration through the thickness of the specimen which is also confirmed by IRT. For F15 sample, abrupt shift of strains obtained from DIC and SG imply a failure being initiated at the surface plies. On the other hand, the delayed failure effect of -15° inner plies for F15 laminate, as observed in IRT images, can be related to shielding effect of 0° layers. Early failure at inner 0° plies for F45 laminate as compared to 45° layers can be related to reorientation of off-axis fibers which tend to align with loading direction, therefore causing migration of crack through the thickness without delamination. The reorientation of surface plies is also evident from the acoustic emission analysis which shows no energy release due to damage development at early stages of the test. Monitoring the failure of F90 sample reveals that global strain measurement technique, DIC, is able to distinguish transverse crack growth while local strain measurement methods are not reliable methods for this purpose. The results of intra-ply crack growth and transverse failure are similar to those reported in [58]. Unlike the results of the other investigators, IRT reveals the possibility of crack initiation from center and consequent growth to the edges of specimen.
- It is evident that techniques such as AE and IRT, provide a more realistic approach towards damage characterization (initiation and propagation). Although AE registers and classifies the damage type, but its validation is supplemented by IRT as witnessed in all the configurations discussed. Moreover, it is shown that in the case of unexpected disintegration of one or more of the systems particularly during the mechanical tests of multi-directional FRPs, multiple monitoring systems can be advantageous. For example, in the case of sample F15, after the sudden detachment of AE sensors, IRT system remained active and provided the necessary data for damage monitoring and analysis during the test.

CHAPTER 4. A NOVEL HYBRID DAMAGE MONITORING APPROACH TO UNDERSTAND THE CORRELATION BETWEEN SIZE EFFECT AND FAILURE BEHAVIOR OF TWILL CFRP LAMINATES

Despite the presence of numerous studies about size effect in composite materials, controversy still exists regarding the relation between mechanical behavior and size of the laminates. Therefore, in this study, a comprehensive experimental approach using combined structural health monitoring techniques namely, acoustic emission, digital image correlation and infrared thermography is conducted to elucidate the physics behind size effect in twill woven carbon fiber reinforced polymeric composites. Laminates with different thicknesses are produced and tested under tensile and in-plane shear loading conditions. In depth analysis of the acoustic emission data shows that an increase in the thickness of laminate changes the fraction of microdamage related to fiber failures. Moreover, a noticeable stagnation period in acoustic emission activity prior to global failure is observed for thick samples which is negligible for thin specimens. Furthermore, analysis of damage accumulation rate via acoustic emission technique is cross validated with digital image correlation and thermography for tensile and shear test results. The full field monitoring results indicate the inverse relation between the thickness of the laminates and damage growth rate. The combined usage of damage monitoring techniques shows that thicker laminates experience slower damage growth dynamics as compared to those of thin laminates, thereby, assisting to understand the size effect in laminated composites.

Keywords: Twill CFRP, Size-effect, Micro-Damage, Digital Image Correlation (DIC), Acoustic Emission (AE), Infra-red Thermography (IRT)

4. 1. Introduction

In recent years, carbon fiber reinforced polymer composites (CFRPs) have been widely used in many prominent applications. Their significant properties such as high strength to weight ratio, superior stiffness, good resistance to corrosion, and enhanced mechanical performance have given them a noteworthy place in the turbine, marine, aerospace, and automobile industries [57, 58]. The ever-increasing need for the application of CFRPs has led to extensive investigation and analysis of their mechanical properties in different conditions. Composite parts are generally designed based on properties and behaviors that are observed for laboratory-scale samples. Since most of the mechanical tests are carried on the samples with standard size and dimensions, being able to integrate these laboratory results into the real-life components is of great importance [78, 79]. Taking all this into account, the question that comes to the attention is to what extent the size of a material can be a factor affecting its mechanical properties.

Failure in materials under loading condition initiates from their weak points i.e., defects, therefore, the possibility of having flaws in large structures is higher as compared to that of a small one. In other words, the strength of material is affected by the size of the tested specimen, and one can expect to observe an inverse relationship between material strength and its volume [80]. This phenomenon, known as the size effect, has often been assumed to be deleterious and destructive with the increase in size. The size effect is an elaborate and versatile topic for composite materials due to the presence of numerous processing (manufacturing) parameters and inherent complex nature of fiber reinforced laminates. The process parameters and manufacturing conditions are factors that can add further complexities to size effect [21, 81]. Mehdikhani et al. [82] indicated that 1% increase in voids due to the manufacturing process results in 10% to 20% reduction in tensile strength of laminate composites. On the other hand, higher probability of finding manufacturing defects for large scale composites structures is evident for their poor mechanical behavior. Therefore, the size effect in composite materials is also dependent on the scale of production. In other words, individually manufactured small components might not indicate the same properties of the specimens cut from a larger structure, which in turn introduces additional complexity in the size effect analysis. In an early study [83] the mechanical performance is shown to be directly affected by the production process and size effect, however, recent

research highlighted that the changes in mechanical performance are majorly dependent on size effect [84].

A preliminary overview of relevant literature indicates the importance of eliminating the risk of disastrous failure induced by significant reductions in the strength of larger components and the necessity of proper characterization of composites via small scale specimens [85, 86]. Moreover, the importance of size effect in fiber reinforced polymer-based laminates has been uttered several times [22, 84]. Some of these investigations are briefed in the following paragraphs.

Sutherland et al. [79] investigated the scale and size effects in unidirectional laminates and indicated that statistical strength theory may be a helpful approach to quantify this phenomenon. They analyzed both unidirectional glass fiber reinforced epoxy and unidirectional carbon reinforced epoxy composites using factorial based and statistically designed experiments. Although they concluded that this approach is an efficient technique in terms of providing thorough information in the composite materials field, no detectable trends were found for tensile and flexural strengths. These findings along with the characterization of failure modes confirmed that the manufacturing parameters are inseparable from the thickness effect, i.e., size effect. Using detailed statistical analysis, they indicated that the change in hand layup manufacturing scale can significantly alter the mechanical performance of the final composite component, and a deeper understanding of the real trend between size effect and material properties can be obtained accordingly. In another comprehensive study, Sutherland et al. [83] investigated the size and scale effects of woven roving composites used in marine structure, which were manufactured through hand lay-up process. By studying the tensile behavior of glass reinforced polyester composites, the authors observed that tensile strength of woven fabric laminates tended to decrease with increasing laminate thickness. The reduction, however, was attributed to the effects of scale of production rather than a genuine size effect (i.e., lower quality specimens are obtained when a thicker laminate is produced). Otherwise stated, the resultant scale effect from the manufacturing of woven roving E-glass reinforced polyester laminates is critical in the mechanical performance of the material and requires extra attention as compared to size effect issue. It was concluded that manufacturing variations were the main reason for observed thickness effect and that manufacturing processes for coupon specimens should closely mirror those used to produce the composite structure.

The effect of thickness on tensile properties of GFRP laminates after exposure to high temperature was investigated by Ashrafi et. al. [84]. By performing a multifaceted study,

they characterized the effect of different factors such as sample thickness (size effect) on post-exposure to the high-temperature mechanical performance in glass fiber reinforced polymer composites. A decrease in strength in the composites with lesser thickness was observed by researchers. They concluded that size scale in terms of thickness is one of the parameters that result in a change in the mechanical behavior of high temperature operated fiber reinforced polymers. Jackson et al. [87] investigated size and scale effects on tensile and flexural behavior of composite laminates. The authors concluded that size effect becomes significant for composite beams under flexural loading, as the load, displacement, and strain at the failure point increases. However, they reported that the elastic properties of composites did not show any dependency on the size factor. Furthermore, Kellas et al. [88] showed that as the number of layers in laminate increases, strain decreases significantly at the failure point. Although these studies clearly indicate the importance of the size effect by comparing the strength and strain at failure for composite material, they do not investigate the issue from the damage growth perspective.

Progressive failure in fiber reinforced laminates occurs due to gradual damage accumulation, therefore monitoring damage growth in composite materials can shed light into new aspects of size effect. Structural health monitoring techniques such as Infrared thermography (IRT), Digital image correlation (DIC), and Acoustic emission (AE) are among the common methods that have been utilized for identification, characterization, and correlation of failure in laminated composites [41, 51, 61, 64, 89]. Munoz et al. [62] correlated failure modes in glass fiber reinforced polymers (GFRP) composites subjected to axial and transverse tensile loads using AE and IRT techniques. Cuadra et al. [63] applied static tensile and tensile-tensile fatigue loading to investigate the adaptability of AE, DIC, and IRT techniques for characterization of the progressive damage accumulation in GFRP composites. Their results indicated that a better understanding of failure is accomplished via the mutual correlation of the results obtained from these techniques. There are many comprehensive studies on synergic application of these techniques for damage analysis in composite materials under various loading conditions. However, to the best of authors' knowledge no specific investigation has focused on using these monitoring methods for scrutinizing size effects under various loading conditions.

This research provides a comprehensive study on the size effect in laminate composites by recruiting two techniques namely, AE analysis and passive IRT. The effect of thickness on tensile and shear behavior, failure modes, distribution of stress and strain, and damage accumulation is investigated thoroughly for samples with different thicknesses. The first

section of the chapter provides information on the material, manufacturing process, and experimental procedure used in this study. Strain measurements are discussed and compared in the next part of the chapter. Furthermore, damage accumulation from AE analysis is correlated with the results obtained from IRT to find out the effect of size on materials behavior. Finally, the last section presents the conclusion of this research.

4. 2. Materials

The raw material is purchased from KORDSA, Turkey as pre-impregnated (epoxy based) Twill woven carbon fabric. The prepreg is designed for autoclave or press curing. The product code of the prepreg as provided by the manufacturer is “KOM10 T700 HSCF TW600 40% 1250”. The specifications of the prepreg are given in the Table 4-1.

Table 4-1. Prepreg specifications

Resin	Fiber Type	GSM	Resin Content	Width of Roll (Weft)
OM10	T700 HSCF 12KT	600	40 wt. %	1250 mm

4. 3. Experimental Procedure

4. 3. 1. Manufacturing of Laminates

The lifetime of the prepreg according to the manufacturer is 1 year at -18 °C, therefore, the uncured prepreg is kept at this temperature inside an industrial fridge. To cut the fabric to desired size for fabrication of laminates, the prepreg roll is first placed at +4 °C for a day, then it is brought to room temperature for 12 hours. This procedure prevents sudden creation of water droplets on the surface of prepreg, therefore avoiding deterioration of prepreg due to humidity. The prepreg fabric is then cut to dimensions of 40 cm x 40 cm using a ZUND G3-L3200 digital cutter. The curing table (mold) for autoclave production is cleaned using ethanol and acetone, and a release agent is applied on its surface before laying up the cut prepreg fabrics on it. The stacking sequences shown in Table 4-2 are used to manufacture the laminates with different thicknesses.

Table 4-2 Configuration of twill laminates

Short ID	Layup Sequence and Orientation	
TW4s	$[0/90]_{4s}$	$[warp/weft]_{4s}$
TW6s	$[0/90]_{6s}$	$[warp/weft]_{6s}$
TW8s	$[0/90]_{8s}$	$[warp/weft]_{8s}$

The prepreg lay-ups of all the laminates are then confined by using a single sheet of vacuum bag. The vacuum bagging scheme for the curing of the laminates in the autoclave is shown in Fig. 4-1. After vacuum bagging, a debulking process is carried out for 30 mins.

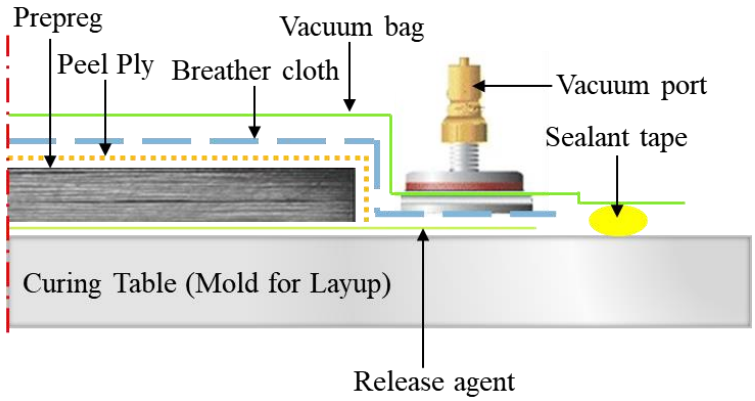

Fig. 4-1. Vacuum bagging scheme for Twill CFRP prepreg

The curing cycle of prepreg was carried out in an ASC autoclave using the recommendations of prepreg's manufacturer in the following sequence: (1) apply full vacuum (1 bar), (2) apply 7 bar gauge autoclave pressure, (3) reduce the vacuum to a safety value of 0.2 bar when the autoclave pressure reaches approximately 1 bar gauge, (4) heat-up at 1 – 3 ℃ per minute to 120°C, (5) hold at 120°C 60 minutes ± 5 minutes, (6) cool at 2 – 5 ℃ per minute, and (7) vent autoclave pressure when the component reaches 60°C or below. The thickness of the cured laminates is measured to be 4.83 mm, 7.30 mm, and 9.87 mm for laminates TW4s, TW6s and TW8s, respectively.

4. 3. 2. Sample Preparation for Mechanical Tests

According to ASTM D3039, the maximum recommended thickness of a tensile specimen standard is 2.5 mm [1]. However, in the present case, the thickness of the TW8s laminate is approximately 10 mm. However, the ISO 527-4 standard "Type 1B specimen" [90], allows a maximum thickness of 10 mm for tensile specimens. Hence, the tensile tests are conducted according to the ISO 527-4 standard where the end-tabs for "Type 1B specimen" geometry are not required as seen in Fig. 4-2. The V-notch in-plane shear tests are also performed

according to the ASTM D5379 [91] standard testing procedure and its relative specimen preparation methods. The specimens are cut with a Poysan B5490 3-axis milling machine.

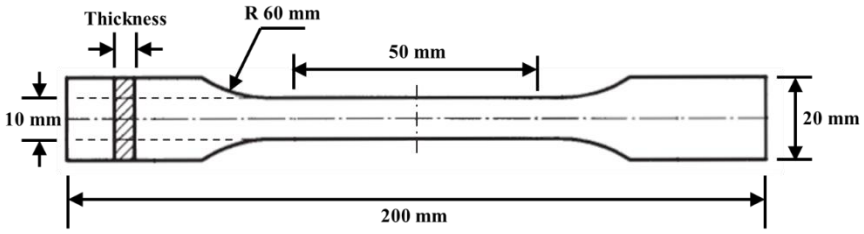

Fig. 4-2. Design of tensile specimen based on ISO 527-4 standard [24] (Thickness of laminates TW4s, TW6s and TW8s is 4.83 mm, 7.30 mm, and 9.87 mm, respectively)

The cut tensile and shear specimens from each laminate are grouped into two groups. While resistive strain gauges are used only for three of the specimens from each set during the mechanical tests, the remaining two specimens of each group are studied under a hybrid monitoring test setup. Here the term hybrid test setup corresponds to in-situ data acquisition by using AE, IRT and DIC (for shear tests) during mechanical tests. The detailed nomenclature of the specimens and their relative test setup are given in Table 4-3. The setup of hybrid experimental setup for mechanical test, the adhesion of strain gauge (SG) and AE sensors to the specimen, and calibration of DIC and IRT are reported comprehensively in chapter 2, 3 and in this article [58]. Moreover, the details of clustering AE hits are given in chapter 2.

Table 4-3 Specimens' Nomenclature

Short ID	Tensile Specimens				Shear Specimens				
	With Only SG		with AE, IRT & SG		with only SG			with DIC, AE, IRT & SG	
TW4s	T4-1	T4-2	T4-3	T4-4	S4-1	S4-2	S4-3	S4-4	S4-5
TW6s	T6-1	T6-2	T6-3	T6-4	S6-1	S6-2	S6-3	S6-4	S6-5
TW8s	T8-1	T8-2	T8-3	T8-4	S8-1	S8-2	S8-3	S8-4	S8-5

4. 4. Results and Discussion

4. 4. 1. Tensile Test Results

The failure of all the tensile samples occurred abruptly at maximum stress level with no apparent macro-damages observed. The maximum tensile strength, average and standard deviation of tensile strength, are shown for each sample in Table 4-4. The average tensile strength increases from 868 MPa to 917 MPa with an increase in the number of fabric layers

from 8 to 16. The average tensile modulus remained ~64 GPa (± 1.92) for all the samples regardless of their thickness implying that materials elastic constants are not varying as consequence of size difference. Moreover, the fiber volume fraction, being 54.63 % (± 0.26) also remained the same for laminates with different thicknesses. These observed trend conceivably imply a direct effect of thickness on the tensile strength of the woven CFRP composites. On the contrary, reduction of standard deviation with thickness increase suggests a less deterministic value of strength for thinner specimens. The more deterministic strength value for thick laminates can be correlated to slower failure progression inside the thicker woven fabric laminates [92]. To explicitly propose and understand the observed phenomenon it is essential to further investigate the effect of the thickness variation on mechanical response via analysis of damage initiation and/or propagation. For which, two specimens from each laminate are tested under tensile loading with inclusion of AE and IRT. In the discussion here, the results of a specimen from each laminate are scrutinized keeping in mind that its mechanical response must represent the average mechanical response of each laminate i.e., the maximum strength of the specimen must be near or equal to the average strength of that laminate. Such a specimen is hereafter referred as representative specimen and the results of acoustic emission and infrared thermography of these representative samples are presented in the subsequent sections.

Table 4-4 Maximum Tensile Strength of Specimens

Maximum Tensile Strength (MPa)								Average Tensile Strength (MPa)
Sample ID	Tensile Strength	Sample ID	Tensile Strength	Sample ID	Tensile Strength	Sample ID	Tensile Strength	
T4-1	885	T4-2	845	T4-3	881	T4-4	861	868 ± 18
T6-1	898	T6-2	897	T6-3	882	T6-4	896	893 ± 8
T8-1	915	T8-2	920	T8-3	911	T8-4	924	917 ± 6

4. 4. 1. 1. Acoustic emission (AE) analysis of tensile specimens

The AE data is clustered based on k-means clustering technique utilizing the procedure mentioned in several articles [47, 57, 93] where the AE parameters namely partial power 2 (PP2) and weighted peak frequency (WPF) are used to cluster the AE data. Herein PP2 is the portion of the power spectrum between 300-600 kHz expressed as a percentage out of the whole spectrum, i.e., 0-1000 kHz. The WPF is the square root of the product of peak frequency and frequency centroid for each acoustic hit. The representative clusters, after employing the clustering procedure, for samples T4-4, T6-4, and T8-4 from the

corresponding three laminates namely TW4s, TW6s & TW8s are shown in Fig. 4-3(a), (b) and (c), respectively. According to previous study by authors the lowest frequency range corresponds to matrix failure while the highest frequency set of data is related to fiber failure in laminated composites [57]. Moreover, the cluster in between the other two classes can be related to interface failure incidents [94]. Therefore, the three observed AE classes in Fig. 4-3 are classified as matrix cracks (MC), interfacial failure (IF) and fiber breakage (FB) based on WPF ranges <160 kHz, 160-360 kHz and >360 kHz. The normalized average fraction of AE hits, for three mentioned failure types, is also given in Fig. 4-3(d). The normalized average fraction of AE hits for each failure type, for a specific laminate, is calculated by averaging the fractional number of AE hits of each failure type obtained from each sample. As seen in Fig. 4-3(d) the dominant failure in all the laminates is the fiber failure. An appreciable effect is a sudden increase in the normalized average fraction of AE hits of fiber failure from TW6s to TW8s, which implies that failure mode of laminates shows drastic change after certain thickness. This could be the result of a greater number of load-carrying fibers in the longitudinal (axial) direction as compared to the ones on the transverse direction with increase in the thickness. This implication is adopted from [43], where it is shown that the increase in the number of off-axis plies reduced the dominance of failure mode from fibrous to interfacial and/or matrix-based. More fiber damage also implies a more efficient load transfer to fibers [95] resulting in better damage tolerance as depicted from the highest strength values for the thickest laminate. It is also noted that with increase in the thickness from TW4s to TW6s, the average hit fraction for matrix cracks and fiber failure did not change substantially for the representative specimens T4-4 and T6-4. But the interfacial failure amount has increased which also endorses the increase in failure strength of T6-4 specimen as compared to T4-4. Overall, it is unearthed that the lowest energy failure mechanism i.e., matrix cracking is more active in the thinnest laminate as compared to that in the thicker ones. With increase in thickness, AE results show that the extent of matrix cracking is reduced while more delamination failure with an intermediate energy release mechanism between matrix cracking and fiber failure is observed [92]. This means a higher strength value for thicker specimens. To be able to further comment on the effect of varying thickness the AE cumulative energy curves are also analyzed to unearth more reasonable resolve to the variations in the tensile strength values with changing thicknesses.

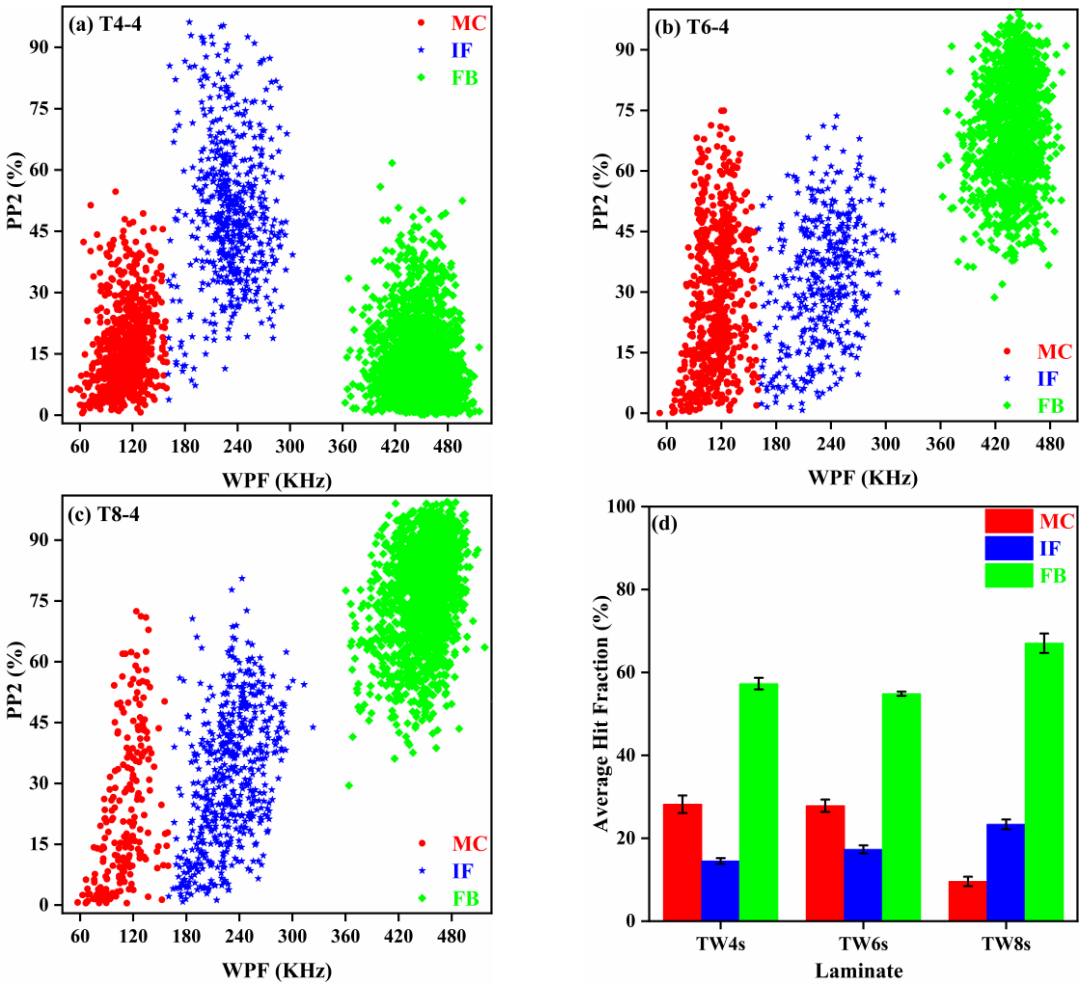

Fig. 4-3. Representative k-means clusters for tensile Samples (a) T4-4, (b) T6-4 and (c) T8-4 from laminates TW4s, TW6s and TW8s, respectively, and (d) Average hit fraction for three failure types for each laminate (MC: Matrix cracking, IF: Interface failure, FB: Fiber breakage)

The accumulation of AE energy, as the failure progresses, and the tensile stress with time are shown in the Fig. 4-4(a), (b) and (c) for representative specimens T4-4, T6-4, and T8-4 from laminates TW4s, TW6s and TW8s, respectively. In all the AE energy graphs, the AE events before the first 25 seconds are neither used as indicators of progressive damage nor as initiation points for micro-damages since the damage imparted below this time is insufficient to affect the linearity of the corresponding tensile stress vs time curves. Upon the loading, one can see that damage activities start simultaneously nevertheless their amount is negligible given the fact that it does not cause any drastic change in the slope of tensile stress vs. time curve. The presence of fiber breakage damage type together with other two damage modes at early stage of the experiments can be justified by analyzing the IRT data. A significant initial upsurge (between 25-40 seconds) in cumulative AE energy could be attributed to the initiation of micro-damages inside the material [96] causing a recognizable change in the slope of the stress vs time curve. This early active period of AE activity could

also be the materials initial vigorous response to the applied loads which certainly becomes weak with increasing loads [57] till the occurrence of the final catastrophic failure.

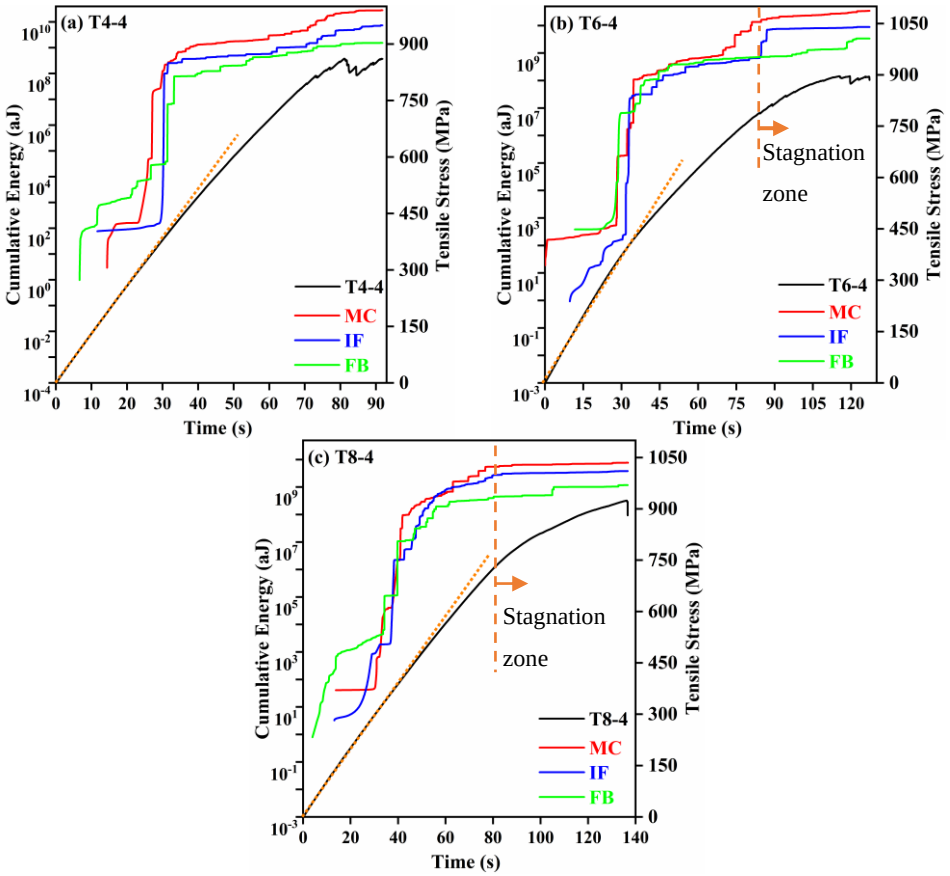

Fig. 4-4. Cumulative AE energy and tensile stress vs. time for specimens (a) T4-4, (b) T6-4 and (c) T8-4 (MC: Matrix cracking, IF: Interface failure, FB: Fiber breakage)

The comparison of cumulative AE energy vs time and stress vs time curves for samples T4-4, T6-4, and T8-4 (Fig. 4-4(a), (b) and (c)) reveals critical details about the effect of thickness variation on progressive damage failure. For instance, the first significant AE energy release in T4-4, T6-4, and T8-4 is at about 25-, 28- and 32-seconds representing matrix cracking; simultaneous matrix-cracking and fiber failure; and simultaneous matrix-cracking and interface failure; respectively. The progressive damage in T4-4 propagates and at about 30 seconds a subsequent strong AE energy release is seen depicting interface and fiber failures at the same time. For T6-4, the subsequent high AE energy release is influenced majorly by interfacial effects at 33rd second of the test. For T8-4, the second strong upsurge in AE energy is observed at about 41 seconds showing all the three failure types instantaneously. Corresponding to this second rise in cumulative AE energy, a distinct change in the linearity of stress vs time curves could be observed after 30, 33 and 40 seconds for T4-4, T6-4, and T8-4, respectively. Although at first it seems that these variations in the linearity of the stress vs. time curves are not very sizable but they do provide strong evidence towards the increase

in the tensile strength with increase in the thickness of the laminates. However, the gradual microdamage accumulation seen as small steps in AE energy continues up to higher stress levels as the thickness of laminate is increased. In other words, after a certain stress level, particularly in T6-4 and T8-4 samples, the acoustic emission activity shows a constant energy level which indicates major load being carried via high stiffness constituent (fibers) and less matrix cracking or interface failure to release the strain energy. This causes a stagnation of damage at the later stages of the test and this zone is specified here as a "stagnation zone". The size of this stagnation zone is longest for T8-4 while it is not apparent in T4-4. For T6-4, the extent of this damage stagnation is intermediate between T8-4 and T4-4. Therefore, the strength of material increases by stagnating the damage due to: (1) a more effective transfer of load to the fibers and, (2) more fibers in the composite system aligned with loading direction for thick laminates as compared to thinner ones.

4. 4. 1. 2. Infrared thermographic (IRT) analysis of tensile specimens

The IR thermograms for the representative samples T4-4, T6-4, and T8-4 from the laminates TW4s, TW6s and TW8s are shown in Fig. 4-5 to Fig. 4-7, respectively. Overall, there seems a good agreement between the AE activity and the IRT results at various points in time. There are few activities which are detected by AE sensors but are not seen by the IR camera and vice versa. This minor mismatch is attributed to the additional thickness of these laminates as compared to that of a thin laminate. The analysis of IR thermograms is discussed in comparison with the AE events for each representative sample in the upcoming text.

In the thermogram shown in Fig. 4-5(a), for sample T4-4 at 11 seconds, no non-uniform temperature fluctuations are seen which advocates the same argument as proposed in the discussion of AE activity stating that the AE events within first 25 seconds do not correspond to micro-damage initiation or propagation. A similar uniformity in temperature distribution is observed for other laminates as well below 25 seconds, therefore the thermal activity above 25 seconds is taken into further discussion. The initial matrix-cracking event for sample T4-4 at 25 seconds in Fig. 4-4(a) is seen as a transverse matrix-crack at upper-right side of the specimen in thermal image of Fig. 4-5(b). Although a significant amount of AE energy is related to this damage, it is not very well pronounced in the relative thermogram. The reason of this disparity could be: (1) as seen in the thermogram this matrix crack is in close vicinity of the AE sensor causing a higher rise in the AE energy and (2) it is possible

that the crack initiated towards the backside of the specimen thus fading the rise in temperature on the surface seen by the thermal camera.

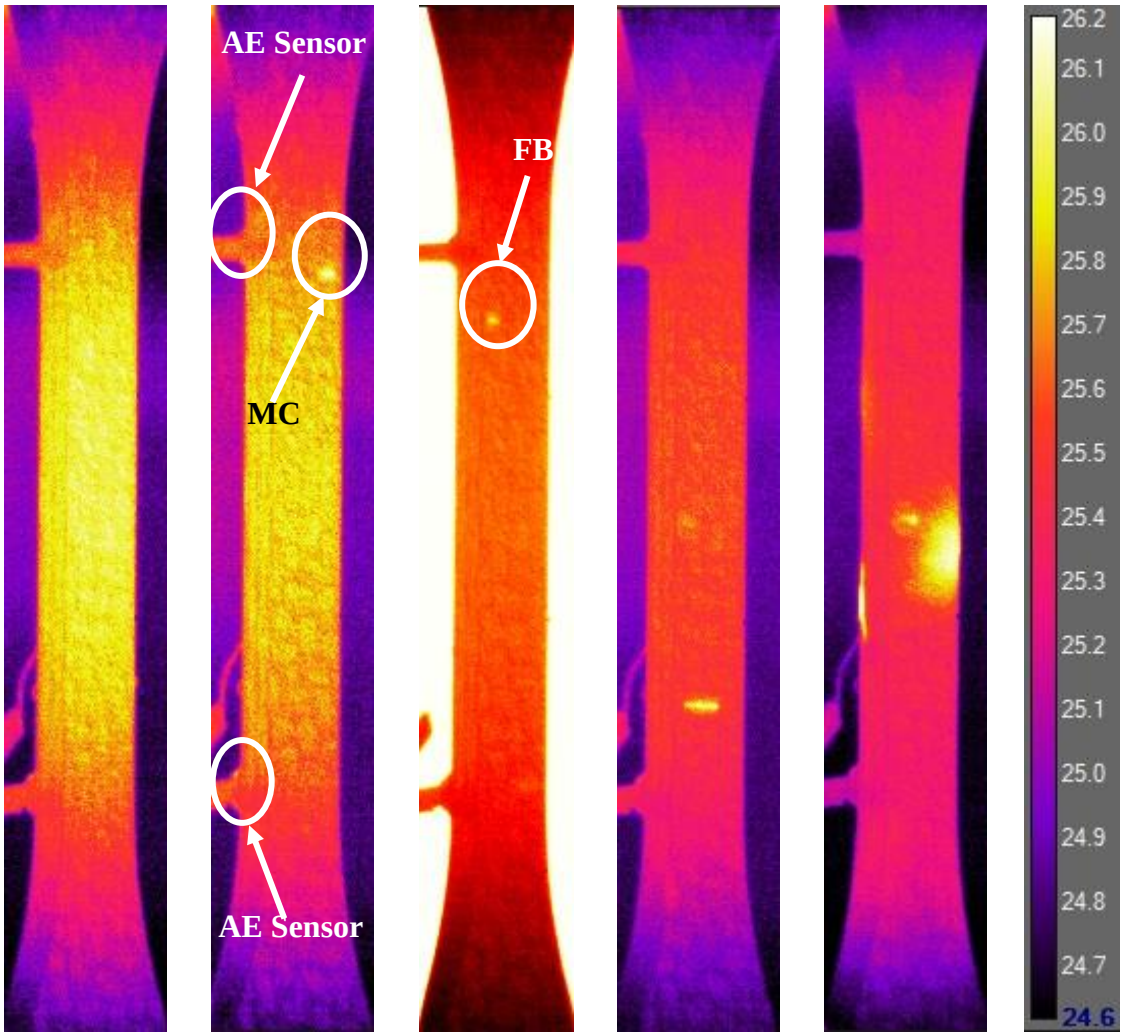

(a) 11 seconds (b) 25 seconds (c) 31 seconds (d) 32 seconds (e) 72 seconds

Fig. 4-5. Thermograms for representative specimen T4-4 from laminate TW4s at (a) 11 seconds, (b) 25 seconds (c) 30 seconds, (d) 33 seconds and (e) 72 seconds (MC: Matrix crack, FB: Fiber breakage/failure)

In agreement with the AE activity, the fiber failure and transverse matrix-cracking at 31st and 32nd second are seen clearly in the thermogram shown in Fig. 4-5(c) and (d), respectively. An important observation to be noted here is that the fiber failure activity, being a shot-lived activity, in the IRT analysis typically emerges as a bright spot of high temperature region unlike a matrix crack and/or delamination [94]. A temperature rise caused by a matrix crack or a delamination, unlike thermal variation due to a fiber failure, does not vanish instantaneously but causes a distribution of temperature in the vicinity of the main failure event by heat transfer to the surrounding areas. Therefore, in the subsequent thermograms after a matrix crack or a delamination the slow dissemination of temperature could be observed easily. But in case of fiber failure, the subsequent thermograms (Fig.

4-5(d) in this case) do not show any indication of the preceding activity (Fig. 4-5(c) in this case). Moreover, matrix carks mostly appear as a stripe (transverse or longitudinal) of high temperature while delamination could be classified by visual flakes or peel-off of the material. This is evident from Fig. 4-5(e), where the multiple failures (IF, MC) occurring concurrently are shown in the thermogram at 72 seconds, which is in line with the AE observations in Fig. 4-4(a).

For sample T6-4 the initial fiber breakage/failure event at 28 second is noticed in the AE energy graphs of Fig. 4-4(b) as well as the thermograms shown in Fig. 4-6(a). Interestingly the matrix cracking event as detected by AE activity at the same time is not observed in this thermogram, which implies that the matrix cracking event could have occurred towards the other side of the sample and due to unconventional thickness of the specimens it is not spotted on the side of the specimen facing the thermal camera.

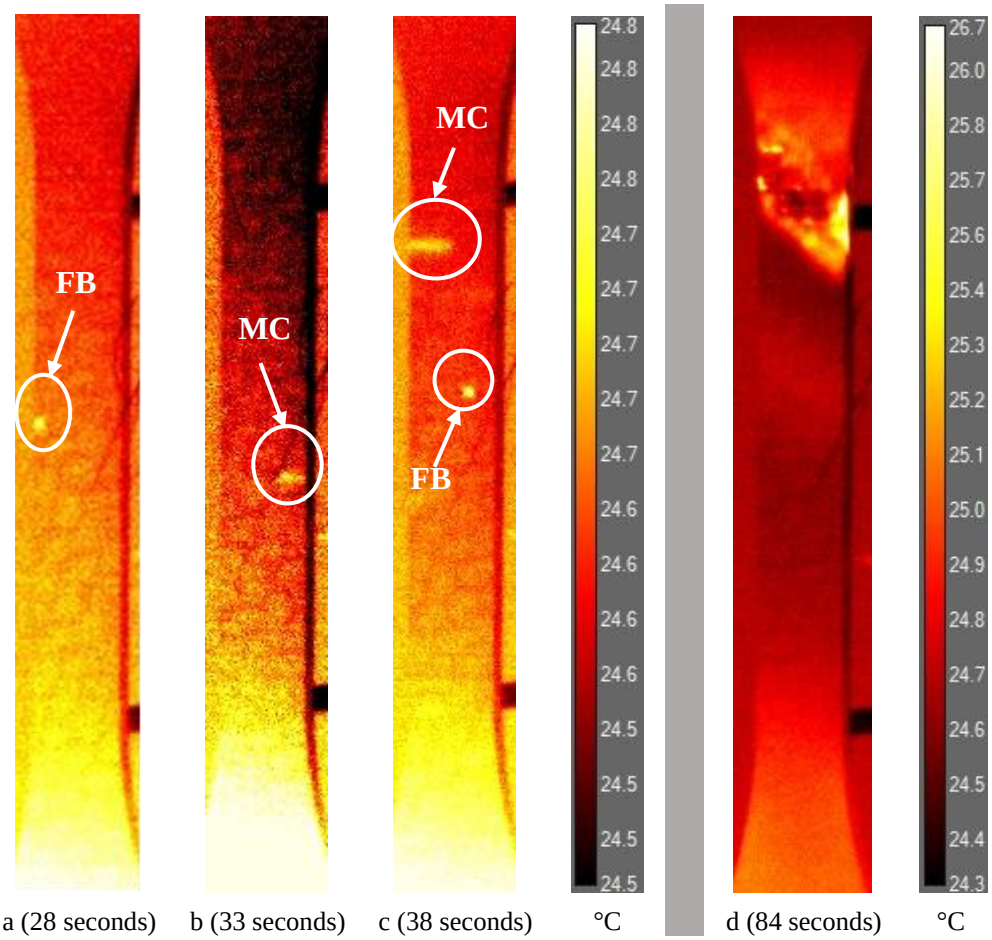

a (28 seconds) b (33 seconds) c (38 seconds) °C d (84 seconds) °C

Fig. 4-6. Thermograms for representative specimen T6-4 from laminate TW6s at (a) 28 seconds, (b) 33 seconds (c) 38 seconds, and (d) 84 seconds (MC: Matrix crack, FB: Fiber breakage/failure)

Moreover, the event marked as fiber failure is attributed to the previously mentioned argument that the fiber failure activity mostly appears as a high temperature speck. To further

unveil this, the matrix cracking and fiber failure events are depicted in Fig. 4-6(b) and (c), which are in-accordance with the AE activity in Fig. 4-4(b). Both events could be distinguished vividly in these thermograms, and the apparent difference between the matrix crack and fiber failure event is also prominent. As pointed out earlier, the interface failure appears as flakes of high temperature region, caused by internal ply splits, ply peel offs, or interlaminar cracks, as shown in the thermogram Fig. 4-6(d). By comparison of this observation with interfacial failure events obtained from AE at the same time, one can presume that the failure has occurred at the first few layers of the specimen. It is worth to note here that the absence of a certain activity in AE or IRT directs to the requirement of a multi-instrumental approach to be able to fully understand the damage initiation and accumulation.

The thermograms of the sample T8-4 also provide similar observations as that of the sample T4-4 and T6-4. For instance, in the thermogram shown in Fig. 4-7(a) at 41st second of the test, a faded high temperature dispersed flake is possibly a matrix crack in-accordance with the AE energy release shown in Fig. 4-4(c) at 40th second, which is categorized as initial matrix-cracking event. The difference in the time of the appearance of the high temperature region and AE energy release event could be explained by considering the thickness of this sample which is 9.87 mm. It is possible that the damage could have occurred at the far end or middle of the thickness of the specimen. This possibility is predicted from: (1) the fadedness of high temperature line caused by dispersion of heat while travelling from far end of the sample, where the damage could have occurred, to the surface visible to the thermal camera and (2) by the higher amount of AE energy release, suggesting the presence of the damage near the AE sensor which is attached on the other surface, not visible to the thermal camera. As pointed out earlier that a fiber failure is a short-lived activity, and one such event is shown in Fig. 4-7(b) and (c) at 55.8 seconds and 56 seconds. A bright high-temperature spot of fiber tow breakage is noticed at 55.8 seconds which is in-agreement with the AE energy release, classified as fiber failure, at the same moment (55-56 seconds) shown in Fig. 4-4(c). A sequential thermogram, soon after the appearance of the bright spot, is taken at 56 seconds (Fig. 4-7(c)) and the high temperature spot vanishes. These attributes of this failure are convincingly enough to characterize it as a fiber failure event. So far, the comparison of thermograms for laminate with different thicknesses reveals that the thermal activities attributed to fiber failure increases accordingly as the thickness of material increases. This observation suggests that the major failure progress in thick composite samples occurs due

to fiber breakage and as depicted in Fig. 4-3(d) fiber failure fraction increase for thicker samples.

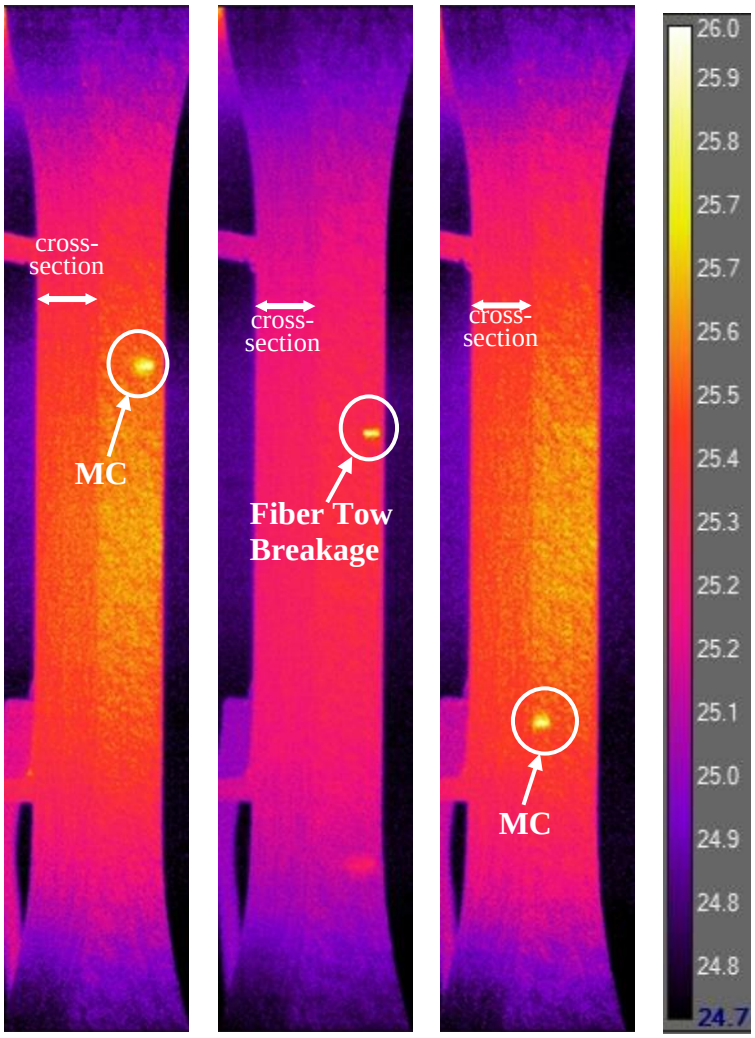

Fig. 4-7. Thermograms for representative specimen T8-4 from laminate TW8s at (a) 40 seconds, (b) 55.8 seconds and (c) 56 seconds (MC: Matrix Crack)

4. 4. 2. Shear Test Results

The maximum shear strength at maximum load, average and standard deviation of shear strength at maximum load, for the set of specimens in which SG is used, are shown in Table 4-5. There is an increase in the shear strength with increase in the thickness. The shear strength of laminates TW6s and TW8s increased 14.7 % and 22.5 % as compared to that of the laminate TW4s with an increase in thickness from 4.83 mm, for TW4s, to 7.30 mm and 9.87 mm for TW6s and TW8s, respectively. Like tensile tests, there is a decrease in the standard deviation of the shear strength values with an increase in the thickness from which

one can propose that for more deterministic results in shear tests, a thicker specimen is recommended.

Table 4-5 Maximum Shear Strength of Specimens

Maximum Shear Strength (MPa)										Average Shear Strength at Max Load
Sample ID	Shear Strength	Sample ID	Shear Strength	Sample ID	Shear Strength	Sample ID	Shear Strength	Sample ID	Shear Strength	
S4-1	94.1	S4-2	95.8	S4-3	89.8	S4-5	89.7	S4-5	91.0	92.1 ± 2.7
S6-1	106.1	S6-2	105.1	S6-3	103.5	S6-5	107.1	S6-5	105.9	105.6 ± 1.4
S8-1	112.3	S8-2	111.7	S8-3	112.3	S8-5	113.1	S8-5	114.5	112.8 ± 1.1

The in-plane shear stress-strain curves for the three representative specimens S4-5, S6-5, and S8-5 from laminates TW4s, TW6s and TW8s are given in Fig. 4-8, wherein two segments of mechanical response from each sample can be distinguished. The initial linear portion of the mechanical behavior indicates the elastic deformation followed by a non-linear region. According to recent studies [51, 93], the initiation of non-linear behavior in the in-plane shear test of woven composites signifies the accumulation of micro-damage between the notches of samples. The coalescence of these micro-damages results in creation of transverse matrix cracks followed by debonding between matrix/fibers. The comparison of shear stress-strain curve in the linear region shows an increase in the shear modules with thickness increment which asserts that the matrix-controlled shear behavior of the composites at the linear region is affected by the presence of more reinforcing element i.e., carbon fibers, in the thicker samples.

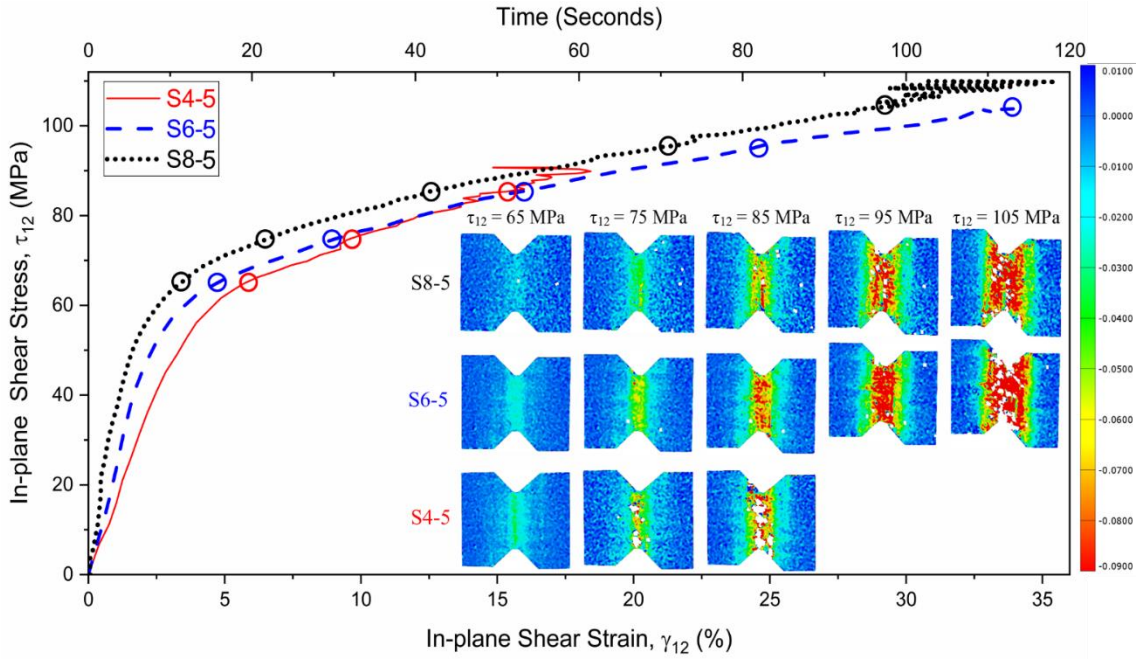

Fig. 4-8. In-plane shear stress vs strain with DIC full field shear strain maps (ε_{xy}) at specified stress levels for samples S4-5, S6-5, and S8-5

4. 4. 2. 1. Acoustic emission (AE) analysis of shear specimens

Fig. 4-9(a), (b) and (c) show AE clustered data for the representative specimens S4-5, S6-5, and S8-5 from laminates TW4s, TW6s and TW8s, respectively. The results of K-means clustering, for the shear tests, shows three distinct clusters associated with three different failure mechanisms, which are classified with respect to their WPF ranges: 80–190 kHz, 200–320 kHz, and 370–570 kHz [93].

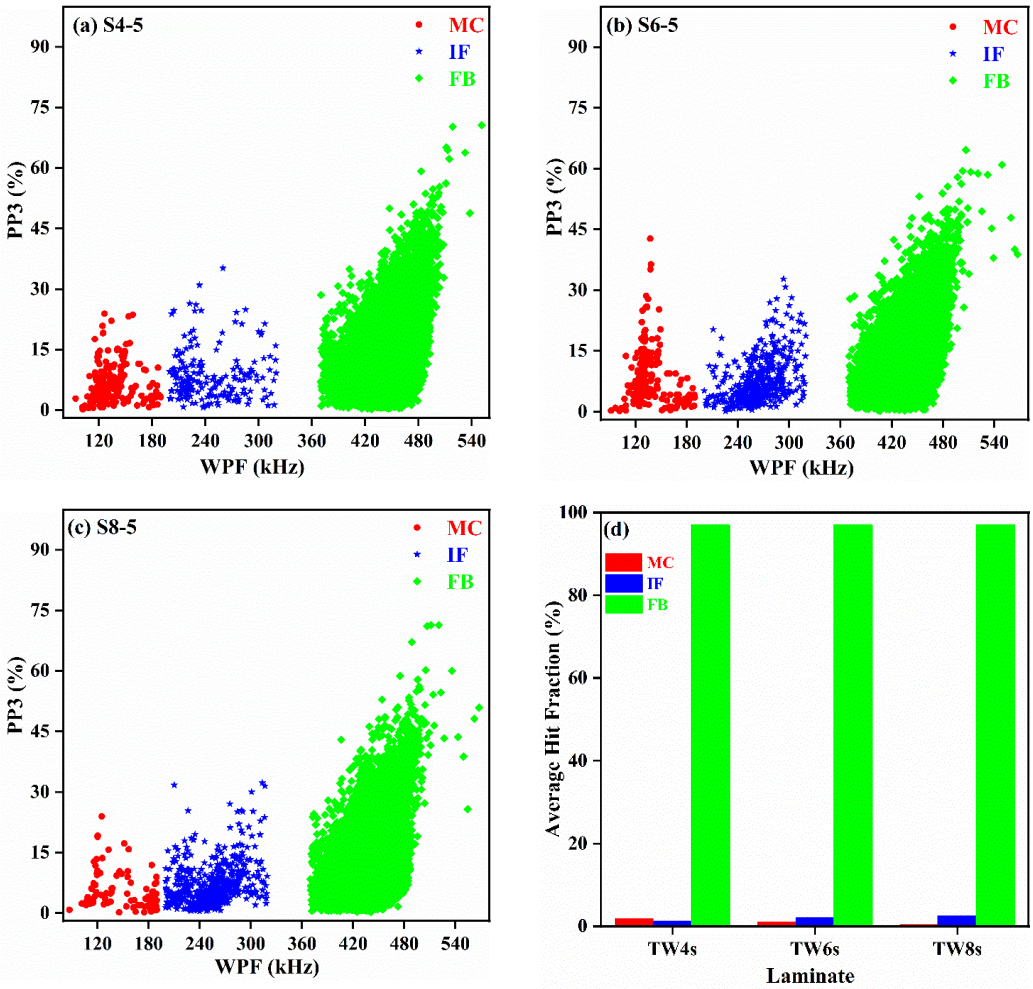

Fig. 4-9. Representative k-means clusters for V-notch shear samples (a) S4-5, (b) S6-5 and (c) S8-5 from laminates TW4s, TW6s and TW8s, respectively, and (d) Average hit fraction for three failure types for each laminate (MC: Matrix cracking, IF: Interface failure, FB: Fiber breakage)

As given in detail for tensile samples, these clusters are associated with three main failure mechanisms of: matrix cracking (MC), interface failure (IF), and fiber failure (FF), respectively. Here PP3 is the portion of the power spectrum between 600-1000 kHz expressed as a percentage out of the whole spectrum, i.e., 0-1000 kHz. The normalized average fraction of AE hits, for three mentioned failure types, is also given in Fig. 4-9(d), where it is observed that high frequency acoustic hits, i.e., fiber failure governs the whole

failure in these laminates under in-plane shear loading. It is observed that there is approximately 1-3 % increase in the average fraction of interfacial or delamination failure with increase in the thickness. A negligible amount of matrix cracking is observed in all the samples particularly in the case of thickest laminate being only about 0.5 %. Although the trend is similar to that of tensile test specimens, but these numbers do not lead to any decisive rationality to explain either the damage propagation or the thickness effect, under in-plane shear loads, for the examined twill laminates. This result indicates that AE study should be further supported by DIC and IRT to reveal the size effect in twill under in-plane shear loading.

The Cumulative AE energy and the corresponding in-plane shear stress variation for specimens S4-5, S6-5 and S8-5 taken from laminates TW4s, TW6s and TW8s are shown in Fig. 4-10(a), (b) and (c) respectively. As proposed while discussing the damage progression in tensile specimens, the initial 25 seconds of the AE energy release could be ignored as no significant micro-damages take place within the material during this starting period. This implication is valid since Yilmaz et al. showed that microdamage saturation and growth between the notches of in-plane shear composite samples starts at the transition point of linear to nonlinear region on the stress-strain curve [51]. Such a transition point for woven fabric specimens in this investigation occurs at ~25 seconds which means that major acoustic emission activities related to stiffness degradation of the material will appear after this moment. As shown in Fig. 4-10(a) around 25 seconds the first major micro-damage for sample S4-5 appears concurrently as a matrix crack and interface failure. For sample S6-5, the first micro-damage at or after 25 seconds could not be classified very prominently. On the contrary, transverse matrix crack and interfacial delamination appear simultaneously as the first major micro-damage for sample S8-5 as evident from Fig. 4-10(c) approximately at 27^{th} second. These observations suggest that the failure starts, in these laminates, with simultaneous matrix crack and delamination followed by extensive fiber rupture events. As seen in the average AE hit fraction data (Fig. 4-9(d)), with an increase in the thickness, the tendency of delamination appears to be increased. This could be explained by carefully observing the initial increase in the energy release rate of interface failure from sample S4-5 to S8-5. Since matrix material controls the shear response of composite materials at nonlinear [97] region, the higher amount of matrix in thick composites can facilitate load transfer to fibers and thereby increase the probability of interface failure events as compared to thinner laminates. Furthermore, there is a decrease in the AE energy release of matrix cracking events with increase in thickness which also suggest the same corollary.

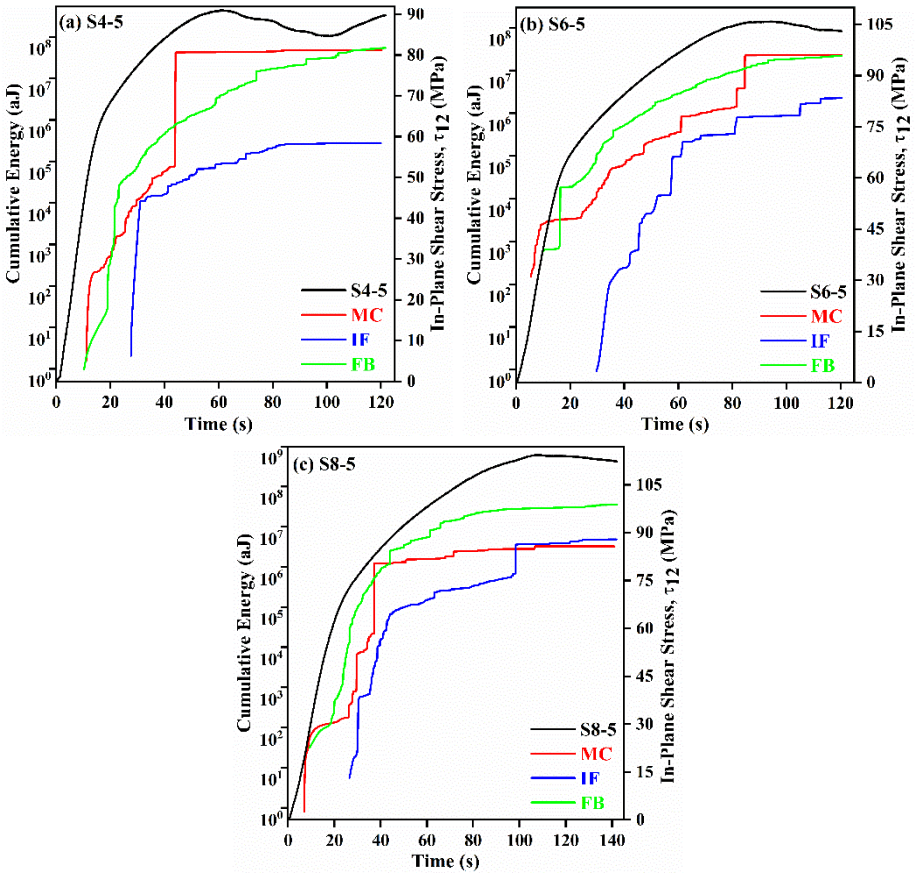

Fig. 4-10. Cumulative AE energy and in-plane shear stress vs. time for specimens (a) S4-5, (b) S6-5 and (c) S8-5 (MC: Matrix cracking, IF: Interface failure, FB: Fiber breakage)

4. 4. 2. 2. Full field strain maps (digital image correlation) of shear specimens

The full field shear strain maps at specified stress levels are shown in Fig. 4-8 for laminates with different thicknesses. At τ_{12} = 65 MPa, the shear strain distribution for the thickest specimen (S8-5) seems uniform while for the samples S4-5 and S6-5 a high strain gradient region between the notches is observed which indicates the presence of micro-damages with the start of the non-linear region on the stress-strain curve. A similar prominent strain gradient, for S8-5, emerges at τ_{12} = 75 MPa while the strain gradient for the sample S4-5 and S6-5 expands beyond the gauge length of sample due to micro damage saturation between the notches. For sample S4-5, the strain map is partially lost suggesting the coalescence of micro-cracks into macro-cracks which deteriorates surface speckle pattern further at τ_{12} = 85 MPa via macro-crack formation. The strain gradient for S6-5 and S8-5 seems almost identical at τ_{12} = 95 MPa, with partial loss of speckle pattern within the v-notch region. But at τ_{12} = 105 MPa, the disintegration of strain map for S6-5 is way more than that of the sample S8-5. These observations from the DIC strain maps evidently reveal that with the

increase in the thickness, the laminate could sustain higher in-plane shear loading. Moreover, the appearance of strain gradient at the initiation of non-linear behavior of stress-strain curve not only confirms the proposition that the micro-damages are initiated at this point but also supports the explanation of damage progression shown in the AE energy release curves, Fig. 4-10.

4. 4. 2. 3. Infrared thermographic (IRT) analysis of shear specimens

The temperature difference (ΔT), the difference between the average temperature in IRT thermograms at a specific time and the room temperature, during the shear test for the representative samples S4-5, S6-5, and S8-5 from the laminates TW4s, TW6s and Tw8s, respectively are shown in Fig. 4-11. The IRT thermograms as insets 1-7 at various specified points are also available in the same figure and will be discussed either in comparison with AE and/or DIC data or based on the abrupt events prompted in the temperature curve. An obvious observation from the temperature difference curves is that for initial 20-25 seconds all the curves remain horizontal without showing any significant change in temperature. This initial period is the same time in which no micro-damage was collected via AE sensors as discussed in the cumulative AE energy curves. During this initial period, a uniform temperature distribution is observed in the whole specimen like the observations made in the DIC analysis where it was shown that the shear strain distribution remains uniform within this initial period. The point at which these temperature difference curves for each sample start to increase correlates to initiation of nonlinear response under in-plane shear loading condition and microdamage accumulation within the gauge length of the samples. It is worthy to note that the inflection point occurs earliest for the thinnest laminate and farthest for the thickest laminates. The first three insets 1,2, and 3 are thermograms for sample S4-5, S6-5 and S8-5 at inflection points corresponding to 23, 26 and 31 seconds, respectively.

The IRT thermogram numbered 4 in Fig. 4-11 is correlated to matrix cracking and delamination events observed for sample S4-5 at about 42 seconds in Fig. 4-10(a). At about 55 seconds, the change in the slope of the temperature difference curve of sample S4-5 is seen and the thermogram (inset-5) is observed where a temperature gradient is observed. It can be argued that the changes in the slope or abrupt steps in the temperature curves obtained from IRT analysis can be utilized as an indication of micro-damages accumulation in the composite laminates. A similar observation is noted for the inset-6 for sample S4-5. Thermal

images alone are not enough to predict or classify the type of damage occurring, therefore, another damage monitoring technique like AE must be utilized simultaneously if the classification of the damage modes is essential. For S6-5, the inset-7 correlates to the change in the slope of the temperature curve and as well as to the AE energy release as shown in Fig. 4-10(b) classified as a matrix crack.

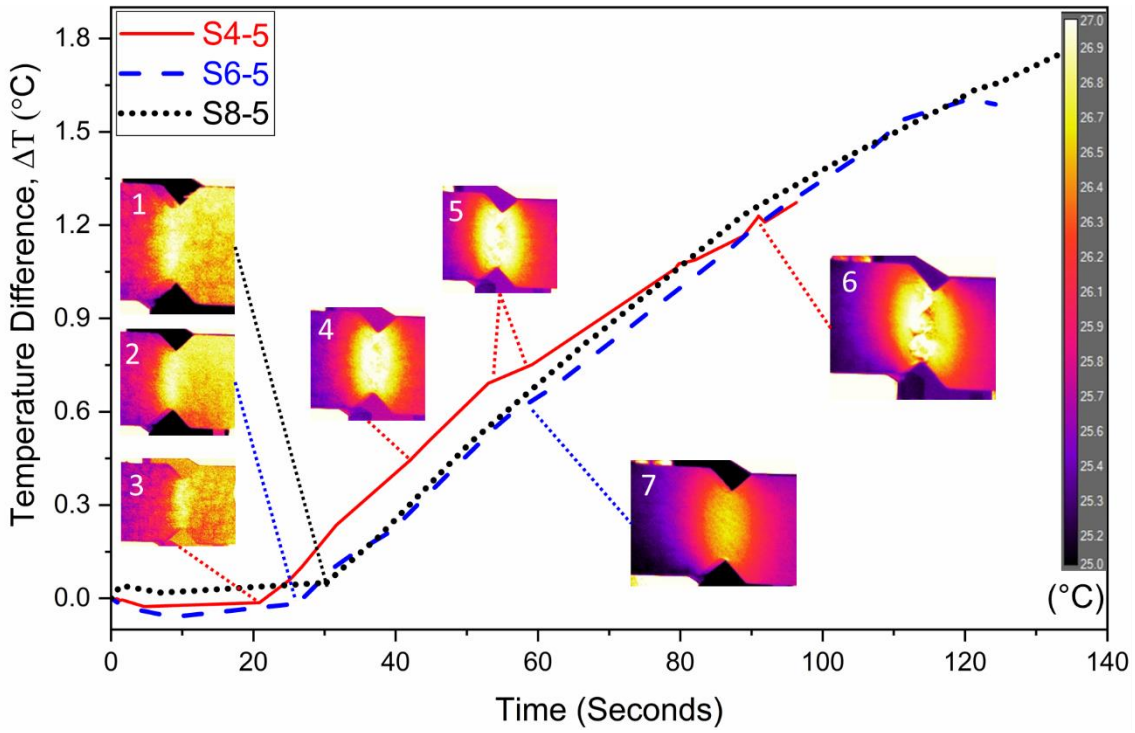

Fig. 4-11. Temperature change ΔT vs. progression time of the shear test with irt thermograms at specified points (Inset 1 belongs to S8-5, Insets 2 & 7 belong to S6-5, Insets 3,4,5 & 6 belong to S4-5)

To summarize, the complementary results obtained via AE, IRT and/or DIC justify the increase in both tensile and shear strength with increase in the thickness of the twill woven CFRP laminates. The initiation of damage is successfully identified by AE and is further validated by the appearance of (1) non-uniform temperature distribution in IRT thermograms and (2) the heterogeneity of strain field distribution in DIC. These observations directed to the earliest slope change of stress vs. time curve and the earliest significant AE energy release in the thinnest laminate as compared to that in the thicker ones for both tensile and shear tests. Moreover, in case of shear tests, creation of high strain gradient in DIC full field strain maps and the slope change of temperature difference vs. time curve from IRT results are observed very early in the thinnest laminates as compared to those of thicker ones. With regards to damage accumulation from AE energy release, the longest stagnation zone for the thickest laminate exhibited the most delayed failure progress. It is evident that employing

structural health monitoring techniques can reveal the physics behind the size-effect in twill CFRPs.

4. 5. Conclusions

In this study, the size-effect that is the influence of thickness variation on the mechanical properties (tensile and shear) and failure dynamics is studied comprehensively by utilizing hybrid test setup. With an increase in thickness from 4.83 mm to 9.87 mm, the tensile strength and shear strength showed an increase of 49 MPa and 20.7 MPa, respectively. Statistically, the results of mechanical tests revealed to be more scattered for thinner laminates indicating a more deterministic strength values for thicker laminates.

Utilizing AE, IRT and DIC for micro-damage analysis under tensile and/or shear loading revealed that micro-damage initiation point is observed earliest in the thinner laminates as compared to the thicker ones.

From AE results, in tension tests, one can conclude that as the thickness increases, the failure due to delamination becomes more active ascertaining a slower damage progression in thicker laminates as the energy required for delamination dominated failure is higher than that of the matrix failure. A stagnation zone is defined for AE energy release rate which is found to be longest for the thickest laminate and shortest for the thinnest one.

The identification of damage type from IRT thermograms, complemented by AE activity, is proposed. It is concluded that a matrix crack appears as a high temperature line which takes more time to disappear as compared to that of a bright high temperature spot caused by fiber breakage event.

Failure dynamics in case of shear tests are also controlled pre-dominantly by fibers. Like tensile test, with increase in thickness the extent of delamination failure rises but not as significantly as in the tensile case. The heterogeneity of DIC strain maps in v-notch region for in-plane shear test samples shows that the damage saturates more rapidly for thinner laminates.

CHAPTER 5. STRESS CONCENTRATION, STRENGTH PREDICTION, AND FAILURE ANALYSIS OF PLAIN-WEAVE CFRP WITH TWO INTERACTING NOTCHES

Composite structures with holes have been utilized in different applications, e.g., swash plates, adaptor plates, and repair patches. These notches reduce the structural performance of the composite plates. In a woven composite plate with two interacting holes, the orientation of the holes affects the stress concentration factor (SCF) and strength of the laminate. The SCF determined by Finite Element Method (FEM) shows that the structural performance of the sample with a single hole is improved through drilling one more hole along the loading direction. The main purpose of this chapter is to investigate the interaction numerically and experimentally between two holes, oriented at different angles, when the woven plate is subjected to tensile load. The location of the processing zone/critical region depends on the configuration of the holes. The processing zone and characteristic distances are established for each sample combining the FEM and Digital Image Correlation (DIC) techniques. Point stress criterion (PSC) and Extended-PSC (EPSC) methods are utilized to predict the final failure strength of specimens. The failure progression under the influence of interaction between the two holes is investigated by Infrared Thermography (IRT). Moreover, to complement the IRT and mechanical results, fractographic analysis is conducted. It is shown that a delamination dominated fracture along loading direction takes place in samples with two holes while a transversal matrix dominated failure is observed for the single notch specimen.

Keywords: Plain-Weave Composite, Interacting Holes, Finite Element Method, Digital Image Correlation, Thermography Analysis

5. 1. 1. Introduction

Textile composites have been utilized in the automotive, aerospace, and energy industries due to their outstanding properties (i.e., specific strength and stiffness) as primary and secondary structural materials. Three different kinds of textile laminate including twill, plain and satin weaves were represented in Fig. 5-1 are used widely in different applications. These applications contain various parts, which need to be joined together to create larger assemblies to obtain the final design. Notwithstanding the favorable physical properties, composites are susceptible to failure under loading with complicated damage behavior, which is rather different from isotropic materials. Therefore, more computations would be required to analyze the performance of these materials. This behavior becomes more complex for the designs containing notches or holes which lead to the reduction in strength due to the stress concentration in their vicinity [7]. Thus, in order to achieve design with superior structural response, it is required to understand the failure mechanics and behavior and of these materials. Significant amounts of research have been conducted on the strength and stress concentration of the composite plates including notches. In a former work, Lin et al. [98] investigated the effect of adding a second hole to the first elliptical notch on the stress distribution of the laminated composites.

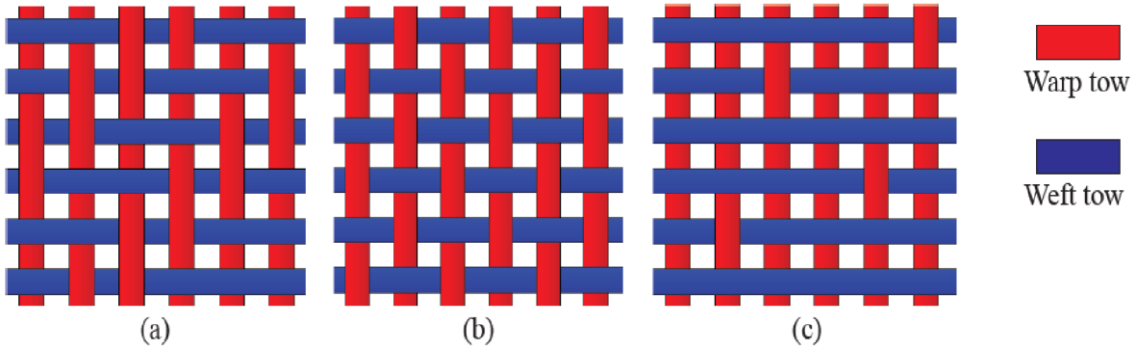

Fig. 5-1. Three well-known woven composites (a) Twill weave, (b) Plain weave, (c) Satin weave

Chang et al. [99] studied the effect of positions and diameter of the holes on the maximum failure load of the composite laminates. Whitney et al. [100]applied stress criteria to predict the strength of the laminated composites including through the thickness discontinuities. Paul et al. [101] employed finite element method (FEM) to calculate the stress concentration factors in thick fiber laminated composites including two holes. Xu et al. [102] computed stress distributions around multiple loaded holes in finite composite laminated plates subjected to arbitrary loads. Xu et al. [103] used the complex potential approach to

investigate the strength of the composite plate with multiple elliptical holes. Green et al. [104] investigated the effect of hole diameter, ply, and laminate thickness on the tensile strength of composite with notch. Atas et al. [105] scrutinized the failure modes of laminated composite plates with two parallel circular holes subjected to traction forces. Also, Karakuzu et al. [106] predicted the failure load and bearing strength in a composite plate with two parallel circular holes. Additionally, Karakuzu et al. [107] studied the effect of hole locations on the failure behavior of glass-epoxy laminated composite plates subjected to a traction force. Ghezzo et al. [108] sought the minimum distance at which no interaction of notch occurs within the area between two holes. Attar [109] conducted numerical as well as analytical analysis to study the stress distribution in a unidirectional laminate with two serial pin-loaded cut-outs. Kazemahvazi et al. [110] utilized an experimental program to calculate the residual strength of glass fiber reinforced vinyl-ester laminates including holes. Habib et al. [111] analyzed the variation of the stress concentration factor with respect to the distance between two holes for composite laminates with three different materials. Yeh et al. [112] investigated the influences of notches' sizes and relative positions on stress concentration factors for an anisotropic plate. Sen et al. [113] examined the effects of stacking sequences and joint geometry on the failure response of two serial bolted joints in composite laminates. Mao et al. [114] used a complex variable method to investigate the bending problem of a composite plate containing multiple elliptical holes. Amaro et al. [115] performed both numerical and experimental studies to assess the influence of single and two holes on delamination induced by low velocity impact on glass/epoxy composite laminates. Ubaid et al. [116] studied the effect of hole distance on the stress concentration factor of carbon fiber reinforced polymer laminate with multiple interacting holes. Maksymovych et al. [117] employed optimization for the shape of the holes existing in the composite plate for reducing the stress concentration in the vicinity of the cut-outs. Jhanji et al. [118] conducted an experimental study assessing the impact of combination of cut-outs with different shapes on the ultimate tensile strength. Cai et al. [119] presented an analytical approach to optimize the hole shapes with different areas under biaxial loads at infinity. Ozaslan et al. [120] applied EPSC method to determine the characteristic distance and critical stress for two interacting holes. Liu et al. [121] developed an FEM model to realize failure analysis of a double-hole cross-ply laminate in tension. Solis et al. [122] studied the effect of holes distance on the damage evolution of the composite plate. Turan et al. [123] investigated the failure loads and failure modes of composite laminates including two serial pin loaded holes in unidirectional carbon fiber/epoxy composite laminates for different stacking sequences.

On the other hand, there have been limited research in the notched woven textile composites specifically with two interacting holes. Pandita et al. [124] utilized digital photogrammetry to investigate the strain pattern for woven fabric composites with either circular or elliptical cut-outs. Toubal et al. [125] utilized electronic speckle pattern interferometer (ESPI) approach to study the strain distribution in a woven fabric composites plate containing circular hole. Xu et al. [126] predicted the strengths of woven textile composite with notch utilizing the cohesive zone model. Taheribehrooz et al. [127] developed a User Material (UMAT) subroutine to solve for the characteristic length in the notched woven composite laminates. Ozaslan et al. [128] studied the stress distribution around the hole of 2x2 twill weave plate with a hole applying the Lekhnitskii's model together with Tan's finite width correction factor. These studies have not been limited to the tensile test. The compressive tests have also been conducted recently. In a recent effort, Zhang et al. [129] conducted a failure analysis for a woven composite plate with notch manufactured by 3D printed technique. In another recent work, Pathakokila et al. [130] investigated the fatigue life of plain weave E-glass/epoxy composite laminate including a hole in the center of the plate and two interacting off-axis circular holes at different angular positions.

Addressed in this chapter is the investigation of the stress concentration factor and strength prediction of plain weave carbon fiber composite material plates with single and two interacting hole(s), in which the interaction occurs when the distance between hole centers is set to 1.5 times the hole diameter, in different orientations under tension. Digital image correlation (DIC) integrated with the passive infra-red thermography (IRT) technique is applied to understand the failure behavior of fabricated samples. To the best of the authors' knowledge, there has not been any experimental study to address the physics behind failure dynamics due to the interaction between two holes in plain-weave Carbon Fiber Reinforced Plastics (CFRPs). Further, the prediction of the failure strength as well as investigation of the failure progression of plain-weave CFRPs with single and/or two interacting hole(s), scrutinized with the usage of DIC and IRT simultaneously, has never been investigated. The FEM analysis is conducted to study the effect of additional hole and their orientation on stress concentration in the vicinity of the holes. Utilizing the correlation between the DIC, IRT and FEM, the stress distribution and strength prediction under tensile loading condition are demonstrated. The critical region of each sample is also estimated, for the first time, by the DIC technique. It is shown that placing the two holes in the longitudinal direction parallel to the applied load decreases the stress concentration factor around 20% and increases the

strength in comparison to the plate with a single hole. Finally, the effect of the orientation of the holes on the damage behavior is also complemented through optical microscopy.

5. 2. Experimental Setup and Numerical Modelling

5. 2. 1. Material

The raw material coded as "KOM10 T700 HSCF 12KT PL600 40% 1250" is procured from KORDSA, Turkey as pre-impregnated plain weave carbon fabric. The prepreg is designed for autoclave or press curing and is composed of high strength carbon fiber (HSCF) T700 12KT and epoxy resin referred to the commercial code of OM10. The fiber area weight and resin content are 600 g/m^2 and 40% by weight, respectively. The average glass transition temperature (T_g) is found to be 123 ± 2 °C.

5. 2. 2. Manufacturing of Plain Weave CFRP laminates

The curing of prepreg is carried out in an ASC autoclave under manufacturer's recommended curing cycle in the following sequence: (i) apply full vacuum (1 bar) (ii) apply 7 bar gauge autoclave pressure (iii) reduce the vacuum to a safety value of 0.2 bar when the autoclave pressure reaches approximately 1 bar gauge (iv) heat-up at 1 – 3 °C per minute to 120 °C (v) hold at 120 °C 60 minutes ± 5 minutes (vi) cool at 2 – 5 °C per minute (vii) vent autoclave pressure when the component reaches 60 °C or below. The employed stacking sequence and the obtained nominal thickness of the laminates are $(0/90/0)_s$ and 3.636 mm, respectively. It should be noted the "0" and "90" are the "warp" and "weft" directions of the fabric, respectively.

5. 2. 3. Mechanical Testing

A Poysan B5490 3 axis milling machine is utilized to cut the specimens. For the material's mechanical characterization tests, tensile specimens (five for each longitudinal and transverse directions) and v-notch shear specimens (five specimens for G_{12}) are cut

according to ASTM D3039 [1] and ASTM D5379 [91], respectively. The tensile specimens with hole(s) are cut to the dimensions given in Table 5-1, in accordance with ASTM D5766 [131]. For the specimens with two holes, three different hole orientations, without changing the hole diameter (D) and distance between the centers of holes, are considered. For the holes oriented in transverse and parallel to the loading direction, an angle (θ) was specified as θ = 0° and θ = 90°, respectively. While, the third hole orientation was obtained by rotating the holes, in the plane of specimen, to θ = 45°. The schematic view of the specimens' geometry is represented in Fig. 5-2.

Table 5-1. Specimen dimensions (all dimensions in mm)

Sample	Short ID	Length	Width	Hole diameter	Thickness	Hole angle
Unnotched	-	250 ± 0.1	36 ± 0.1	6	3.636 ± 0.05	-
Single notch	1H	250 ± 0.1	36 ± 0.1	6	3.636 ± 0.05	-
Two-holes transverse	2H0	250 ± 0.1	36 ± 0.1	6	3.636 ± 0.05	0
Two-holes 45	2H45	250 ± 0.1	36 ± 0.1	6	3.636 ± 0.05	45
Two-holes longitudinal	2H90	250 ± 0.1	36 ± 0.1	6	3.636 ± 0.05	90

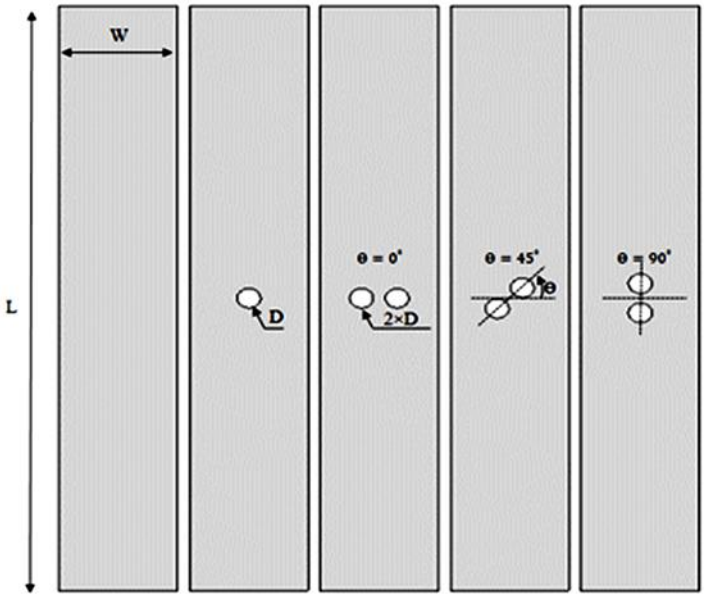

Fig. 5-2. Schematic view of specimens

All the specimens are tested on an Instron 8853 universal testing machine with a load cell of 250 kN (alignment calibrated) and at speed of 2 mm/min. ASTM D3039 and ASTM D5766 standard are utilized for performing the tests for un-notched and notched plates, respectively. For tests with notched laminates, DIC and IRT are employed simultaneously to monitor damage progression, the test setup for which is shown in Fig. 5-3.

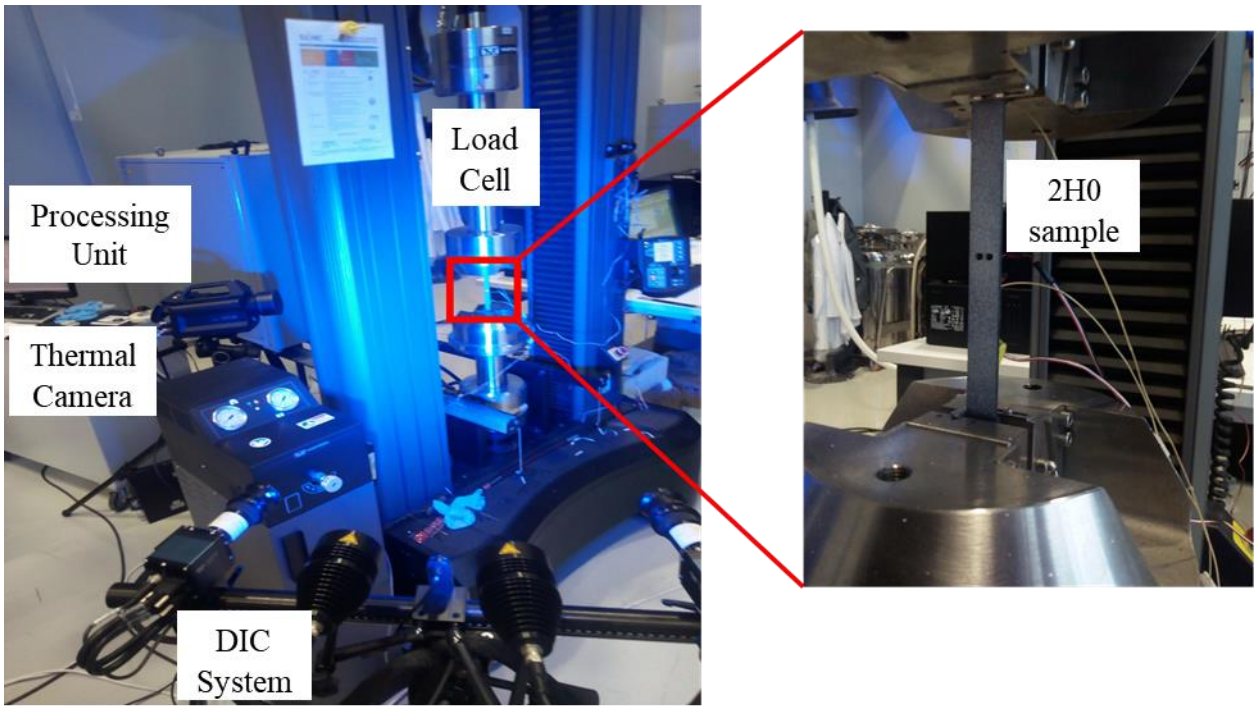

Fig. 5-3. Experimental setup including DIC cameras, IRT camera, load frame coupled with painted test sample

In order to achieve the material properties, five samples are tested to verify the repeatability. Material properties of plain-weave samples are given in Table 5-2 wherein the E_{11} and E_{22} are longitudinal and transverse modulus, ν_{12} is Poisson ratio, and G_{12}, is the in-plane shear modulus, which meanwhile represent the orthotropic material properties.

Table 5-2. Average material properties of the fabricated plain-weave specimens

$\boldsymbol{E_{11}}$ (MPa)	$\boldsymbol{E_{22}}$ (MPa)	$\boldsymbol{\nu_{12}}$	$\boldsymbol{G_{12}}$ (MPa)
61835 ± 949	53846 ± 1183	0.1	3607 ± 377

5. 2. 4. Digital Image Correlation (DIC)

Digital Image Correlation (DIC) is mostly utilized for monitoring and measuring the local strains throughout the tensile specimen [57, 58]. GOM (Braunschweig Germany) 12 M sensor system is employed for this purpose. Black and white paint spray is utilized for creating speckle pattern on the gauge length of the sample. The sensor is calibrated by 200 × 150 mm calibration plate, which is instructed by the manufacturer. The results of calibration showed 0.03 pixels calibration deviation and 0.0018 mm scale deviation, which are between upper and lower bound values provided by the manufacturer. Pattern quality analysis is conducted applying the ARAMIS software before the initiation of the

experiments. GOM inspect software is utilized to carry out the analysis of the obtained results.

5. 2. 5. Infrared Thermography (IRT)

Infrared Thermography (IRT) is a Non-Destructive Test method which detects infrared energy emitted from an object, changes it to temperature, and shows an image of temperature distribution [94, 132]. Passive IRT is used in this study to record the temperature of the sample during the mechanical testing. Surface temperature distribution of the specimen is recorded during the test with an infrared camera (FLIR X6580sc) containing 50 mm lens which is placed at ~70 cm away from the tensile test specimen. The operational temperature range of the IRT camera is from -20 °C to 3000 °C. The sampling rate of 150 Hz is chosen to record the images at a resolution of 640×512 pixels. FLIR Research IR Max image analysis software is employed for the analysis purpose.

5. 2. 6. Fractography

The gross macroscopic fracture morphology is examined to compliment the findings of IRT. The fracture surfaces are also analyzed utilizing stereo microscope to identify the principal damage features of the fracture areas around the hole(s). The fractography results are discussed to support and elaborate on the difference between the strength of the examined samples.

5. 2. 7. Numerical modelling

The numerical analysis is conducted via the commercial FE analysis package: ABAQUS/Standard 2017. Ply-by-ply approach is applied while assigning material orientations with orthotropic mechanical properties to each lamina based on the stacking sequences of the fabricated plane-weave containing 6 plies. An 8-node linear brick, reduced integration, and hourglass control elements are utilized for all the cases. To achieve more accurate results in the area of interest (region in the vicinity of the holes), the mesh size is reduced around it. A very fine mesh is applied near the hole to get the stress gradient. The

mesh convergence study, shown in Fig. 5-4, for the plate with two holes in longitudinal direction (2H90) revealed that the mesh size around the hole should be set to 0.06 or less. Therefore, 0.06 mm element size is chosen.

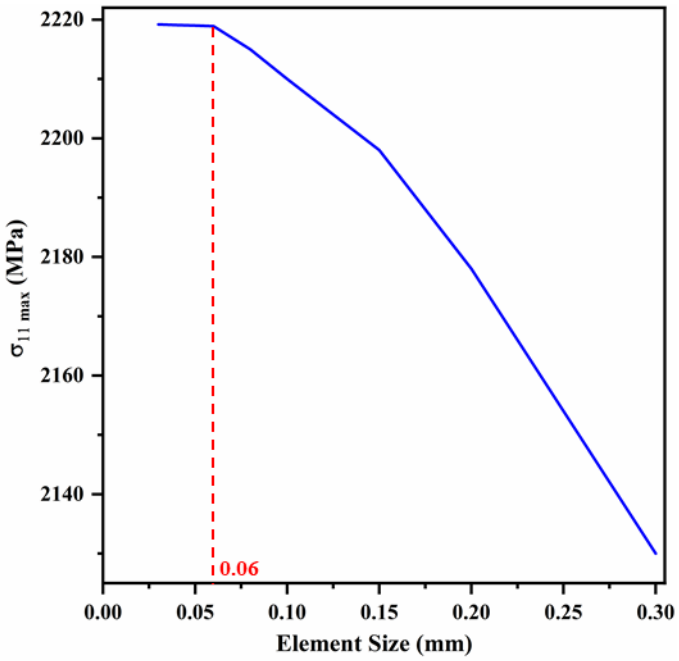

Fig. 5-4. Mesh convergence study ($\sigma_{11\ max}$ is the maximum tensile stress at vicinity of a hole)

The FEM model contains 336096 number of elements with 395430 nodes for all the cases. Fig. 5-5 shows the model as well as the boundary conditions based on the testing machine grips. The tension load is applied to the right-hand side, and it is free in loading direction only while the left-hand size is fully clamped which are compatible with the experiment.

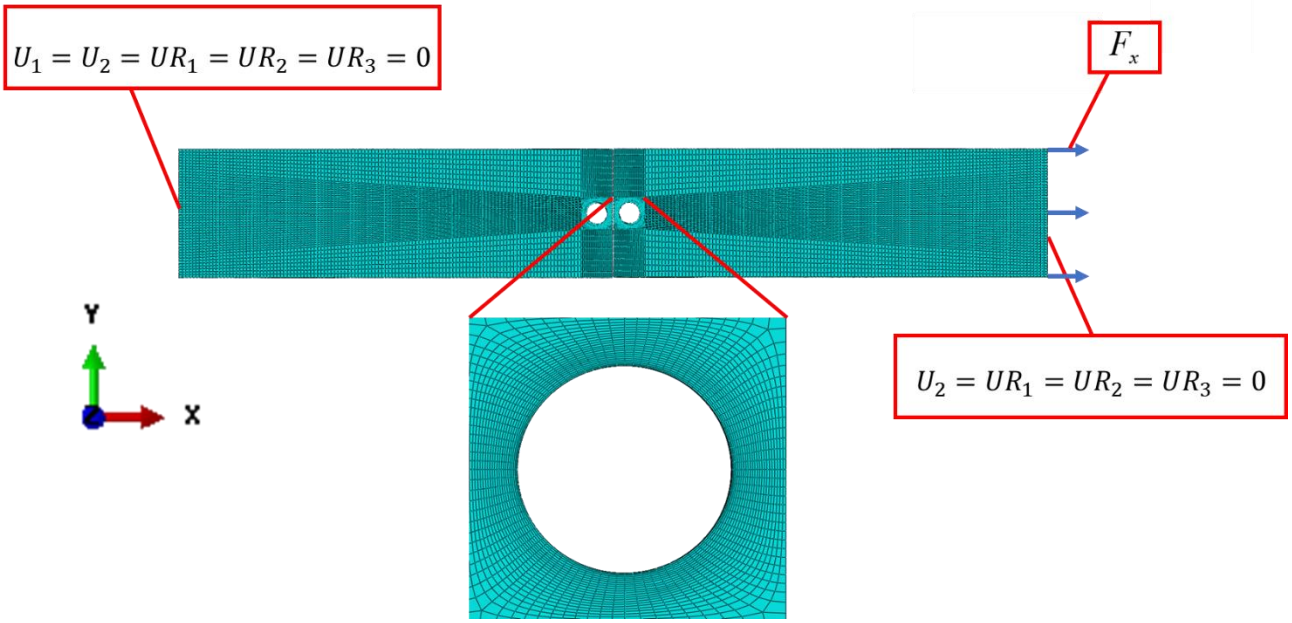

Fig. 5-5. FEM model and applied boundary conditions together with the close-up view for the mesh resolution around a hole

The finite element method (FEM) is first verified with experimental results in terms of stress-strain behavior. The comparison of FEM and average experimental result for the un-notched specimens in terms of overall laminate stiffness is represented in Fig. 5-6. The numerical modelling result is in good agreement with the tensile test outcome.

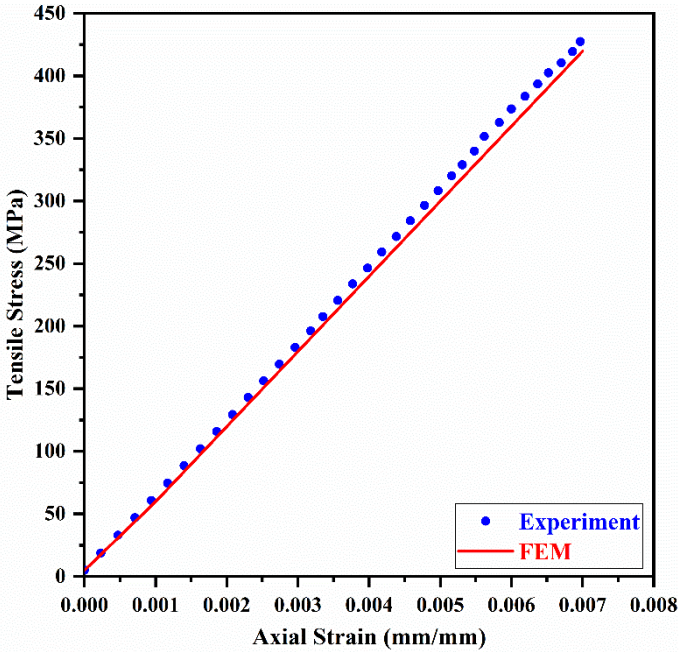

Fig. 5-6. Comparison of FEM and average experimental result for the plane-weave plate without notch

5. 3. Results and Discussion

In this section, the results of the numerical simulations are compared with those of experiments, obtained through using digital image correlation as well as the thermal camera analysis. Fracture behavior of all specimens is discussed later by employing the stereo microscopy analysis to investigate the effect of hole orientation.

5. 3. 1. Mechanical Test Results

Average tensile strength values for five (05) specimens from each configuration with their corresponding standard deviation are shown in Fig. 5-7. The bar graph includes the values of strength for un-notched laminate and notched laminates with different hole(s) orientations. Standard deviation of each group of laminates is calculated and compared to

have a better understanding about the accuracy of the results which is represented as error bars. As expected, the highest value of strength is for laminate without a hole while among the notched samples, the 2H90 and 2H0 has the highest and the lowest tensile strength, respectively.

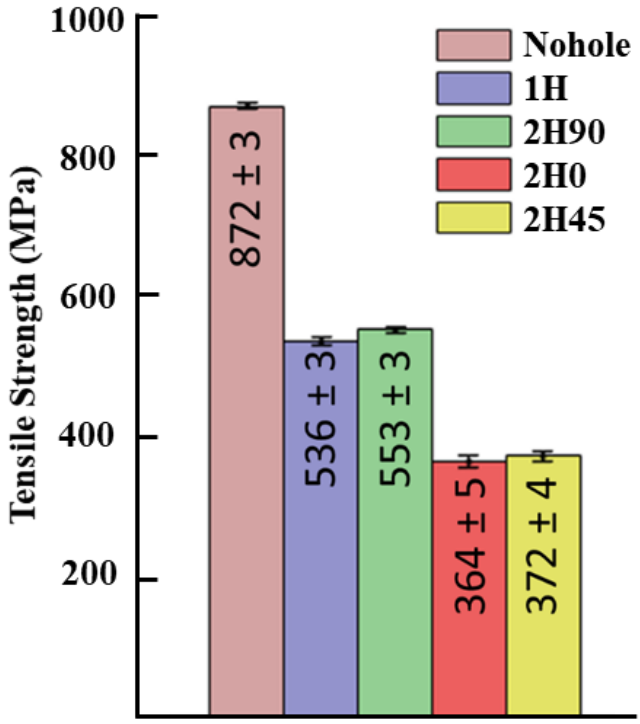

Fig. 5-7. Average Tensile strength values of all the specimens with their corresponding standard deviation

5. 3. 2. Numerical Analysis

The numerical analysis is conducted to calculate the characteristic distance as well as subsequently predict the failure strength of the specimens. First, the SCF, which is the ratio of the maximum average stress to the remote stress should be found for all the specimens. The axial stress distribution (σ_{11}), at the failure load of each specimen, in the loading direction for the sample with; single hole (1H), two holes in transverse (2H0), two holes at 45° (2H45) and two holes in longitudinal (2H90) are shown in Fig 8 (a), (b), (c) and (d), respectively. It should be highlighted that the (σ_{11}) is plotted for each specimen in its own failure load.

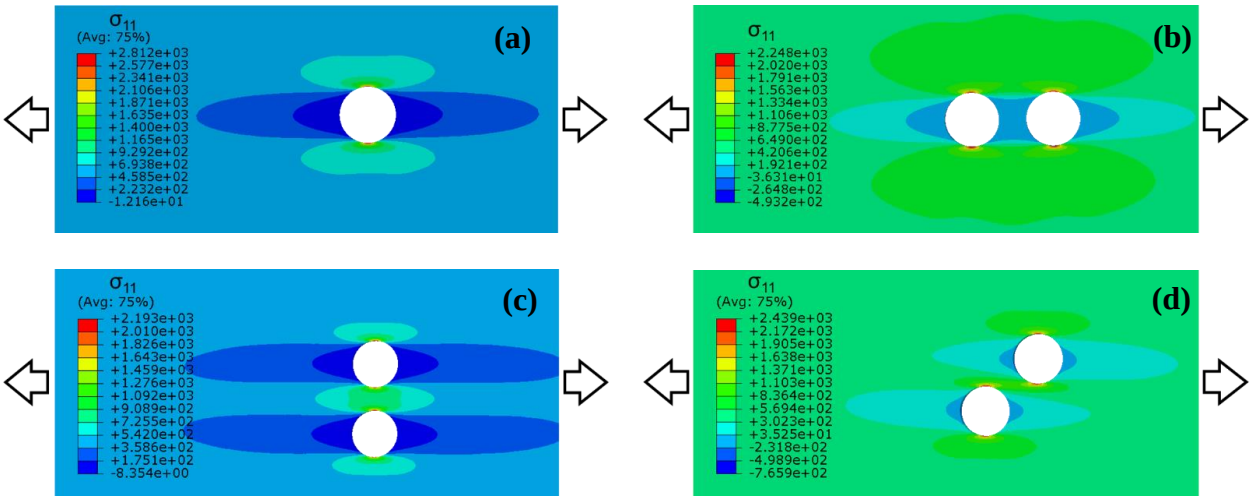

Fig. 5-8. Stress in loading direction for final failure of (a) 1H, (b) 2H90, (c) 2H0, and (d) 2H45 (Arrows points to the loading direction)

The SCF for the 1H sample is 30% less than that of the sample 2H0. While SCF for 2H90 is the least among all samples. Also, the woven plate 2H45 has the highest SCF among the others. The SCF for this case is around 22% more than the single hole case. On the other hand, 2H90 has the least SCF with approximately 22% less than that of the 1H sample. It suggests that the design with longitudinal holes is the best among all manufactured samples in terms of its load-bearing capacity. The SCF for all the specimens is shown in Table 5-3.

Table 5-3. Stress concentration factor for different notched plates

Specimen	1H	2H90	2H0	2H45
SCF	5.3	4.16	6.03	6.48

In case of a plate with a single hole under a tensile load, the processing zone/critical region is along the horizontal line joining the periphery of the hole to the edge of the plate and most of the stress is also distributed along this line. In case of two holes, depending upon the distance between the holes and orientation of the holes, this region could either exist in-between the holes or towards the outer periphery of one of the holes. For the specific case of interacting holes, distance between the holes is 1.5 times of the notch diameter, the placement of the critical region is dependent only on the hole orientation. To predict the failure strength of the composite plate with hole, the Lekhnitskii formula is altered to apply the point stress criterion (PSC) [100] as following:

$$\sigma^{\infty} = \frac{\sigma_0(0, r+d_0)}{\frac{1}{2}[2+(\frac{r}{r+d_0})^2+3(\frac{r}{r+d_0})^4-(K_t-3)[5(\frac{r}{r+d_0})^6-7(\frac{r}{r+d_0})^8]]} \quad (1)$$

wherein K_t, the stress concentration factor is obtained through the FEM, r is the radius of hole, and d_0 is the characteristic distance.

It is worth to note that even though these formulas do not take into account the size of the hole, due to the equivalent size of the holes in all specimens, there is no requirement to analyze the hole size in this study. The material properties in Cartesian coordinates are calculated utilizing the Force-Strain coupling matrix. Fig. 5-8 also provides an indication about the critical region; wherein higher stress is concentrated and the failure initiates and propagates along this region [120]. The critical region for samples 1H and 2H90, is located at the outer periphery of the hole(s), while for samples 2H45 and 2H0, it is located in-between the holes.

The stress along the loading direction is plotted on a horizontal path created from the outer periphery of hole to the edge of the specimen in 1H laminate, and for 2H0 sample, the axial stress distribution is plotted along a path created between the two holes as shown in Fig. 5-9. According to the PSC method, the characteristic distance is the distance from the edge of the hole where the stress in the loading direction reaches to the strength of the unnotched composite plate. The characteristic distance d_0 = 1.32 mm is calculated using the axial stress distribution curve, obtained by FEM, around the hole for 1H sample as depicted in Fig 9. The strength of 2H90 sample could be predicted using Eq.1 by putting values of (r), (d_0), and failure strength of unnotched sample and SCF of 2H90. For the sample with the critical region/processing zone between two holes, the study in [120] proposed an extended form of PSC (EPSC) method, which could be adopted to predict the failure strength of 2H45 laminate. According to this proposed EPSC approach, the extended characteristic distance (d_0') is found to be 1.66 mm at the intersection point of stress distribution curves of 1H and 2H0 sample as represented in Fig. 5-9. At this extended critical distance, a new strength value is defined as an extended strength ($\sigma_0' = 800$ MPa). The strength of 2H45 sample is predicted applying Eq.1 utilizing d_0' and σ_0' and SCF of 2H45 as calculated by FEM.

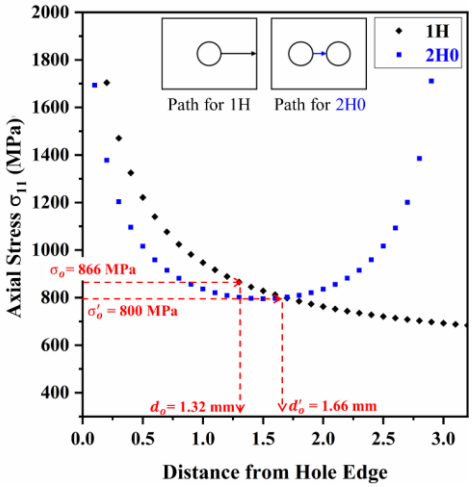

Fig. 5-9. Averaged stress distributions of single hole and transverse holes

5. 3. 3. Critical Region Determination by DIC

As indicated by the SCF achieved by FEM the critical region for 2H90 is located on the outer periphery of the holes while for 2H0 and 2H45, it seems to be between the two holes. To further validate this proposition, DIC is employed to identify the critical region wherein two points are considered on DIC surface within 1.3 mm in between the holes and at the periphery (towards the edge of the specimen) of one of the holes, as depicted in the insets of Fig. 5-10. The axial strain obtained from these points and the average total axial strain obtained from the DIC strain field are compared for each of the three specimens with two holes (2H0, 2H45, 2H90) as shown in Fig. 5-10. For specimen 2H90, the strain at point1 is comparatively more linear than that at point2 whereas it is relatively linear at point2 for specimen 2H0 and 2H45, which approves that the critical region is located at the outer peripheries of the holes for 2H90, and in-between the holes for 2H0 and 2H45 [120].

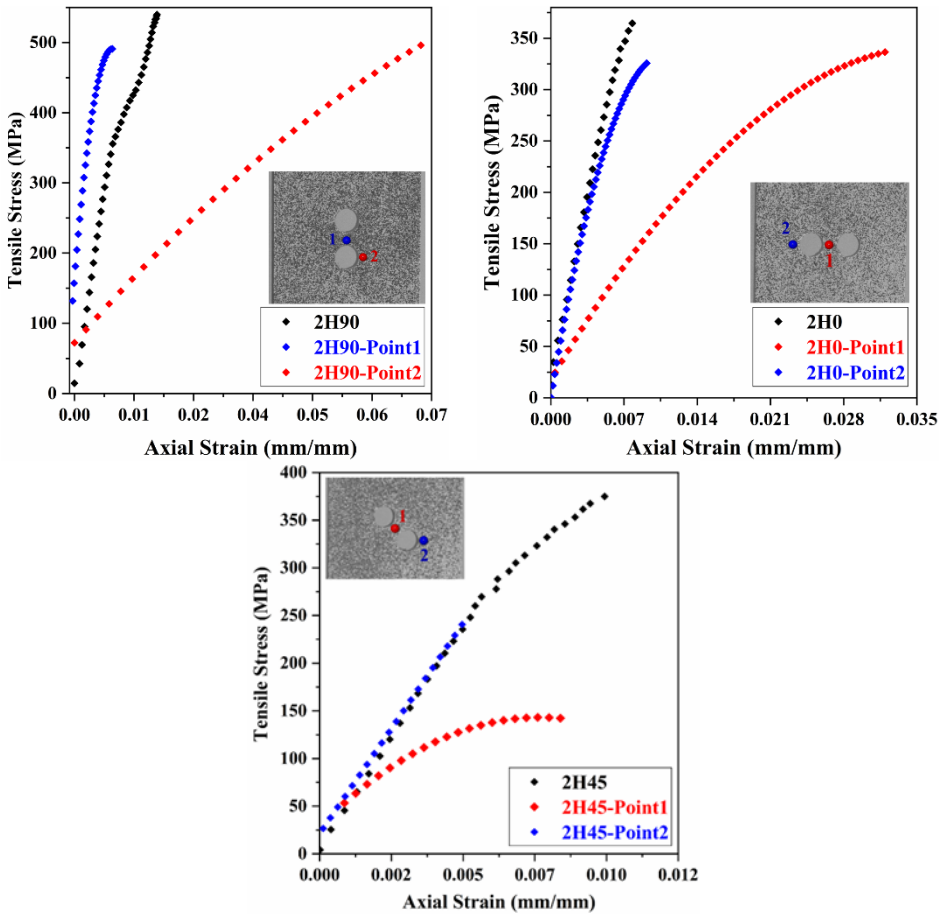

Fig. 5-10. Processing zone/critical region determination utilizing DIC experimental data.

As mentioned earlier the PSC and proposed EPSC methods are used for predicting the strength of notched laminates for which, apart from un-notched failure strength, the determination of the characteristic distance is a prerequisite. It is worth mentioning that the

characteristic distance has been calculated from FEM. However, in the present study, an experimental approach based on the DIC data is proposed to determine the characteristic distance. The DIC directly provides the strain map which means one can get the strain at any point of the region of interest at any time. The strain field around the hole for 1H specimen is obtained by constructing a section line, along the width, from the periphery of hole to the edge of the specimen. This experimentally obtained strain field (axial ε_{11} and transverse ε_{22} strains) around the hole could be converted to axial stress distribution σ_{11} around the hole, by assuming the overall mechanical properties to be orthotropic under the plane stress condition [133], utilizing the following equation:

$$\sigma_{11} = \frac{E_{11}\varepsilon_{11}}{\left(1-\nu_{12}^2\frac{E_{22}}{E_{11}}\right)} + \frac{\nu_{12}E_{22}\varepsilon_{22}}{\left(1-\nu_{12}^2\frac{E_{22}}{E_{11}}\right)} \qquad (2)$$

The axial stress distribution around the hole for 1H and 2H0 specimens obtained from Eq. 2 are shown in Fig. 5-11. It should be noted that the axial stress is based on the strain obtained by DIC, and a possible non-uniformity in the strain values could have affected the behavior of the curves. Nevertheless, this did not influence the intended characteristic distances values, d_0 and d_0', which are achieved by PSC and EPSC approaches as obvious in Fig. 5-11. The values of these distances are well compatible with those obtained via FEM.

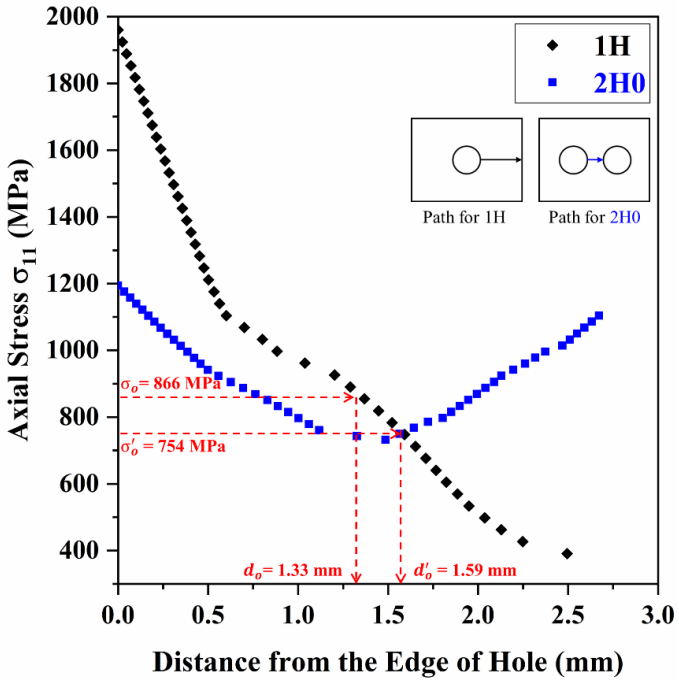

Fig. 5-11. Averaged stress distributions and characteristic distance of 1H and 2H0 (DIC)

The prediction of failure strength employing PSC and EPSC method for sample 2H90 and 2H45, respectively is shown in Table 5-4. The prediction for specimen 2H90 (processing

zone on outer periphery of holes) achieved by FEM and DIC are in a good agreement with the value obtained by experimental result. The comparative study between experimental and FEM/DIC shows that the proposed EPSC method [120] for 2H45 (processing zone in between holes) is not applicable. The reason of which could be attributed to the difference of material system and/or stacking arrangement. A more in-depth understating should be devised to utilize such criterion in different materials systems.

Table 5-4. Strength prediction by PSC and EPSC [120] approach

Strength Prediction for 2H90 (PSC Approach)					Strength Prediction for 2H45 (EPSC Approach)				
Experimental (MPa)	FEM (d_0 = 1.32 mm)		DIC (d_0 = 1.32 mm)		Experimental (MPa)	FEM ($d_0' = 1.66\ mm$)		DIC ($d_0' = 1.59\ mm$)	
	Value (MPa)	Error (%)	Value (MPa)	Error (%)		Value (MPa)	Error (%)	Value (MPa)	Error (%)
553	583	5.4	584	5.5	372.5	663	78	620	66

5. 3. 4. Progressive Failure Analysis by IRT

For the specimens, 1H and 2H90, with the critical region ascertained at the periphery of the hole(s), towards the edge of the specimen, the failure initiation and propagation are also expected in the same region. IRT thermograms of representative samples of 1H and 2H90 are shown in Fig. 5-12 and Fig. 5-13, respectively. In accordance with the SCF values, the initial axial split, as depicted by high temperature longitudinal lines, occurred at a lower stress level for specimen 1H as compared to that of the specimen 2H90 (462 MPa vs. 528 MPa), as shown in Fig. 5-12(a) and Fig. 5-13(a), respectively. After this initial delamination, several such events are observed, particularly for 2H90, on both edges of the holes which are not shown here for brevity. The important point to be noted here is that the length of the axial split is longer for 2H90 specimen, certainly due to interaction of holes, as compared to 1H specimen. These axial splits provide a crack-blunting or stress relieving effect [134, 135], thereby delaying the onset of catastrophic failure by stress-redistribution. Although, the longitudinal splits are observed in 1H specimen but the crack blunting effect is not as much pronounced as in the case of 2H90 specimen. This is ascribed to two factors: (1) the higher initial SCF for 1H than that of 2H90 and (2) the shorter axial splits size in 1H0 than that of 2H90. As the load increases, the extent of damage also increases and the temperature distribution around the hole(s) just before the maximum stress level reveals another beneficial effect of the interaction between the two holes. It is observed that for 1H specimen, the distribution of temperature is more spread in the transverse direction from the hole

periphery to the edge of the specimen (Fig. 5-12(b)), confirming a weaker crack-blunting effect.

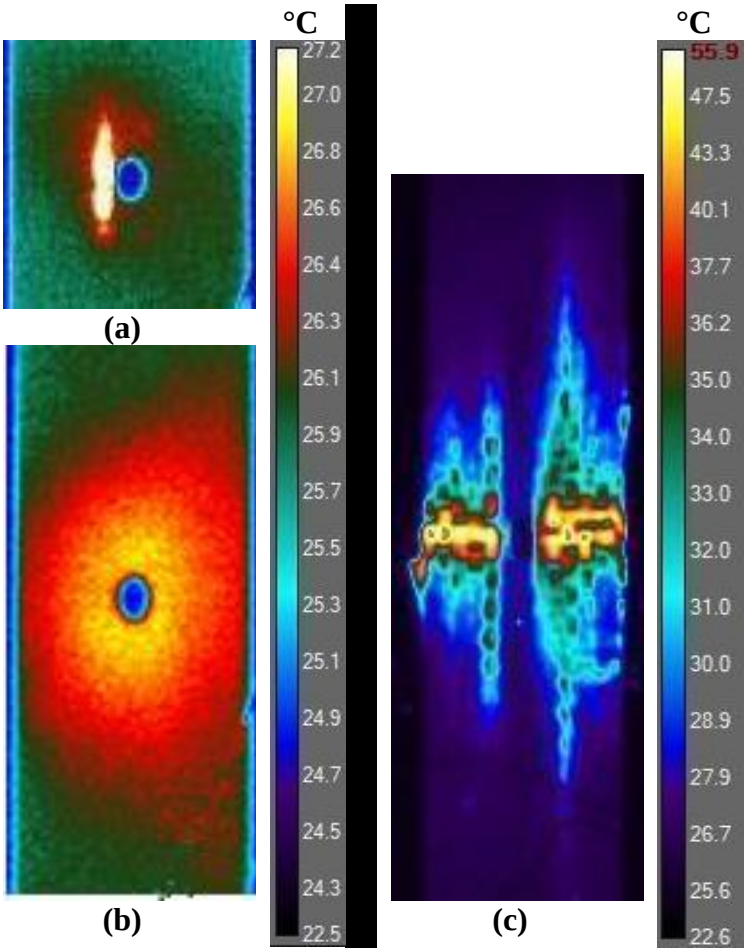

Fig. 5-12. IRT thermograms for sample 1H showing (a) initial delamination (462 MPa), (b) temperature distribution around the hole (523 MPa) and (c) final failure (528 MPa)

However, for 2H90 specimen, the remarkable behavior of the interaction of two holes is seen, where the temperature distribution around the holes remains confined to a smaller portion of the specimen's width (Fig. 5-13(b)). Moreover, due to the presence of the two longitudinal holes, the temperature distribution is advanced more along the longitudinal direction as compared to that of the 1H. This observation is consistent with the earlier attributed crack-blunting effect which ascertains that the stress concentration is effectively redistributed to reduce the transversal matrix cracking. The IRT thermogram for specimen 2H90 at maximum stress level, Fig. 5-13(c2), reveals a triangular temperature distribution which provides an evidence of delamination along the length of longitudinal splits at the peripheries of both the holes, which is also confirmed by the complementary DIC image, Fig. 5-13(c1). In addition to this, 2H90 specimen does not fail abruptly at the maximum stress, 540 MPa, but continues to transfer the load until the final catastrophic failure at a lower stress of 529 MPa, Fig. 5-13(d). The reason of this effect is attributed to the reduction

in the effective cross-section of the sample and the final failure occurs by fiber-cracking and delamination. On the contrary, the 1H specimen fails catastrophically at the maximum stress of 528 MPa, as revealed in Fig. 5-12(c). The damage in 1H sample evolved with successive ply splits around the hole and any other feature, apart from an imbalanced stress distribution around the hole, is not observed. The unsymmetrical stress distribution eventually resulted in a delamination dominated failure on one side of the specimen as shown in Fig. 5-12(c). These observations again approve the effectiveness of the stress concentration blunting effect in 2H90 specimen.

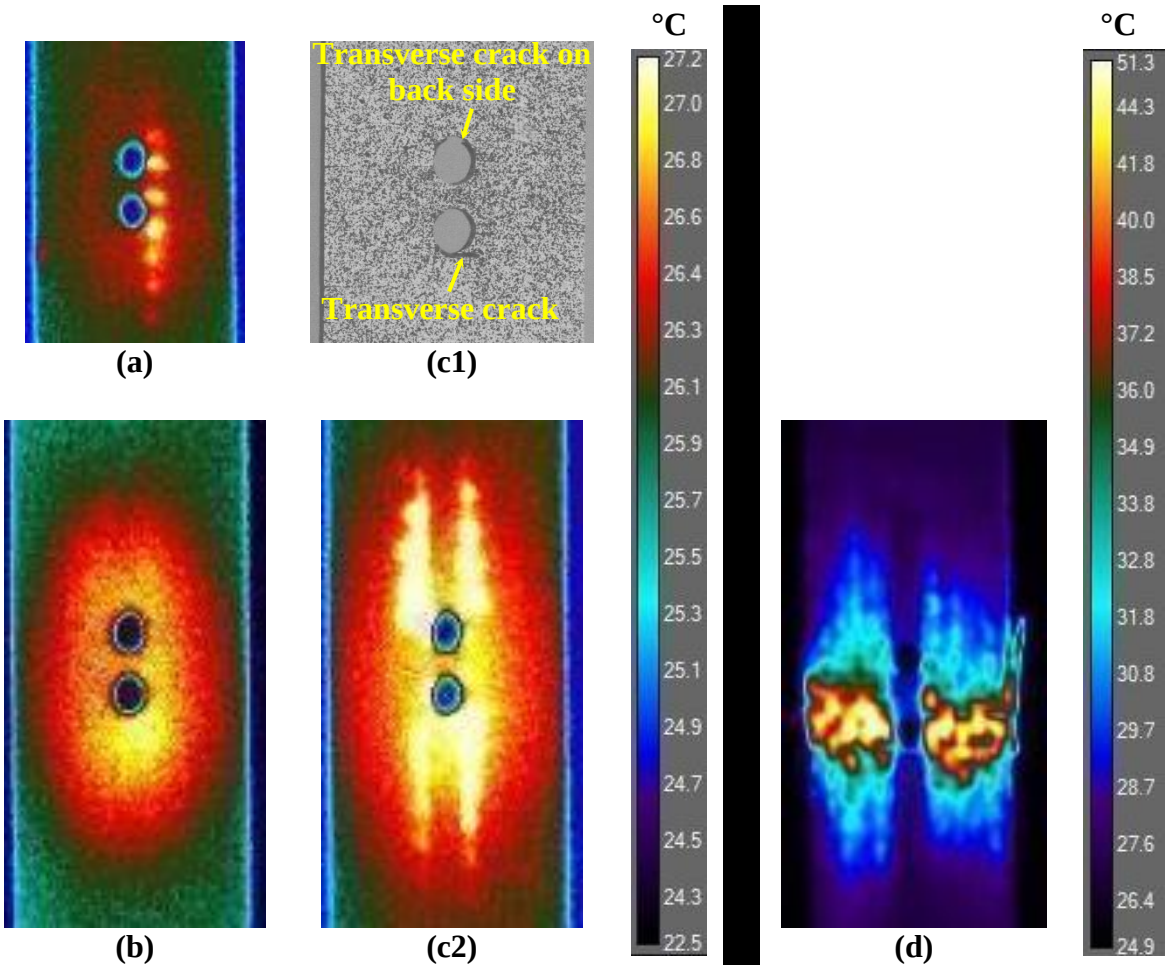

Fig. 5-13. IRT thermograms for sample 2H90 showing (a) initial delamination (528 MPa), (b), (c2) temperature distribution around the hole before and at maximum load (540 MPa), respectively, (d) final failure (529 MPa) and (c1) complimentary DIC image at max load

For the 2H0 and 2H45 specimens for which the critical region is determined in-between the holes and the SCF values are 6.03 and 6.48, respectively, one should suspect that the specimen with the higher SCF value should exhibit a lower final strength and vice versa. However, a complete contradiction is seen here i.e., the average maximum strength of 2H0 is 364 MPa which is less than the average maximum strength of 2H45 being 372 MPa. To understand this anomalous characteristic, it is crucial to investigate the failure dynamics in

these laminates. In order to do that, the IRT is employed, and very interesting findings are unveiled. Firstly, as depicted in Fig. 5-14(a) and Fig.15 (a), the initial failure for 2H0 and 2H45 occurred at 309 MPa (at 57.5 seconds) and 235 MPa (at 41.8 seconds), in agreement with the SCF values. The complementary images Fig. 5-14(b) and Fig.15 (b), taken from DIC, also show the initial damage of the outer surface ply. These DIC images also show that the initial failure is along the line joining the centers of the holes, in-accordance with the stress distribution around the holes obtained from FEM.

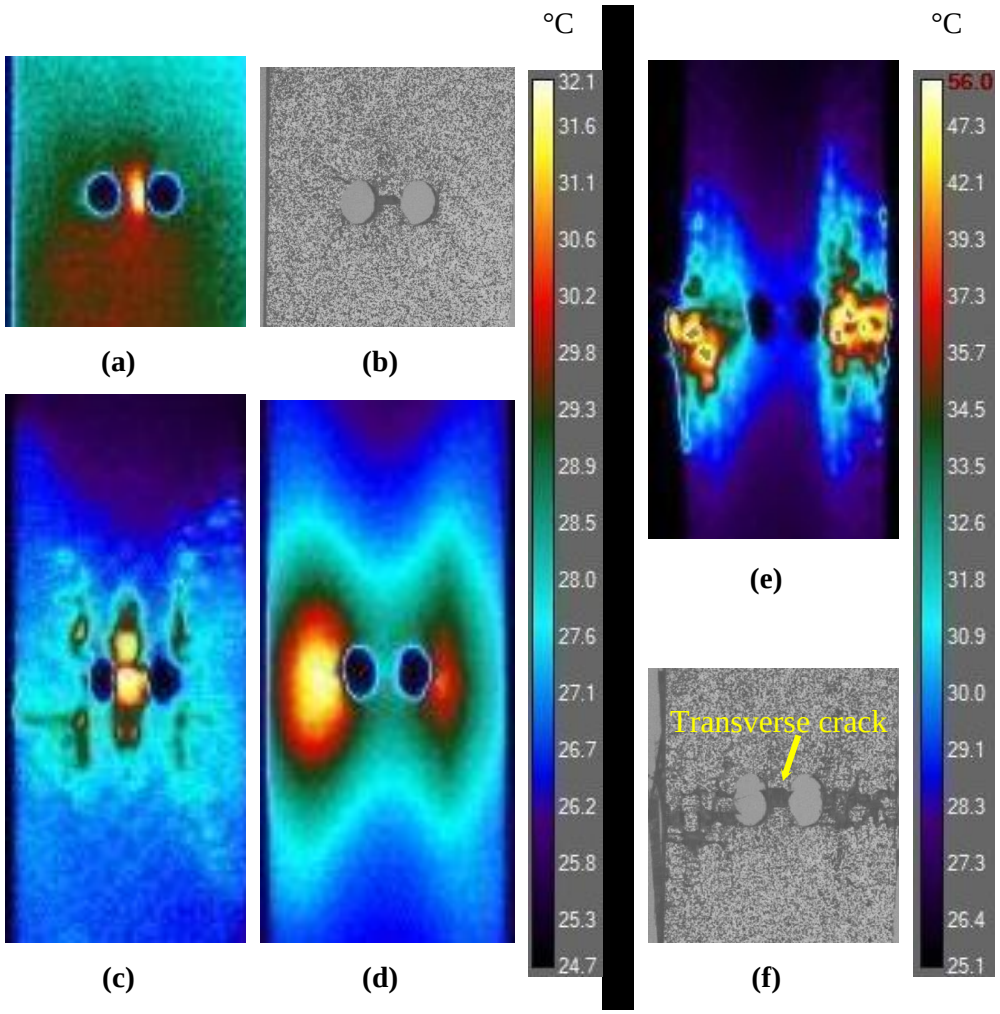

Fig. 5-14. IRT thermograms for sample 2H0 showing (a) initial delamination (309 MPa, 57.5 seconds), (b) complimentary DIC image after first failure, temperature distribution (c) at maximum load (368 MPa, 76.7 seconds), (d) before final failure, (e) at final failure (339 MPa, 89.5 seconds) and (f) complimentary DIC image after failure

After the initial failure, the specimen 2H0 continues to carry the load in a traditional manner such that the processing zone/critical area remains in between the two holes. Eventually, as seen in Fig. 5-14(c), the specimen reaches its maximum strength of 368 MPa (76.7 seconds) with the damage, as expected, being mostly accumulated within the central area of the holes. On the other hand, for 2H45, the initial failure opened an entirely unconventional failure

progression phenomenon. Thereby, after the first delamination event in-between the holes, the progression of failure does not remain confined to the central portion between the two holes. But instead, the failure progression continues at the outer edge of the two holes as depicted from the delamination events shown in Fig. 5-15(c). The most probable reason for this transformation, of the working zone from the central region between the holes to the outer periphery, could be the effect of the orientation of the holes. This could be explained by carefully observing the initial failure in Fig. 5-14(b) and Fig. 5-15(b) wherein it is clearly visible that the initial failure in 2H0 is perpendicular to the loading direction while in 2H45 the initial crack has propagated at an angle of 45°.

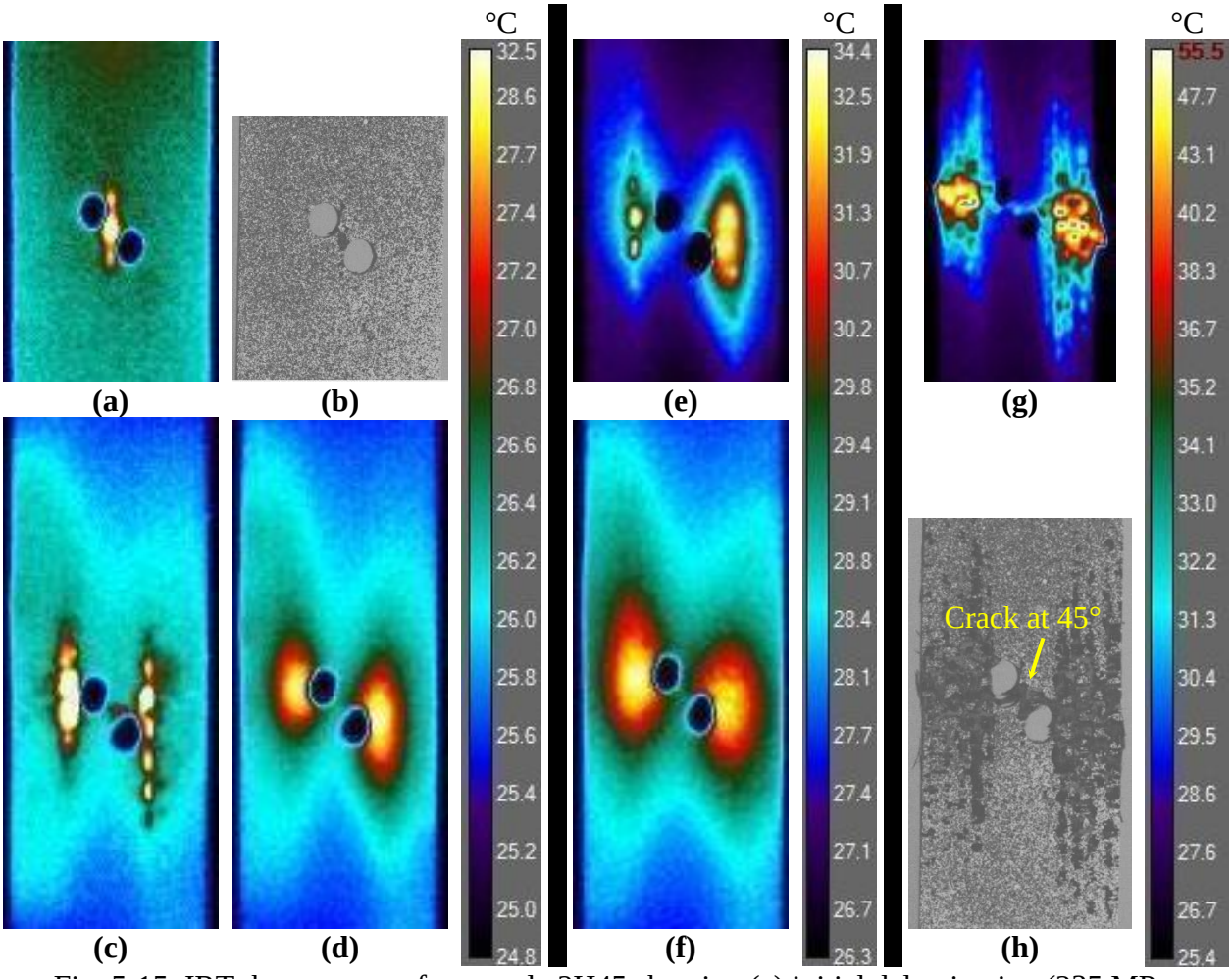

Fig. 5-15. IRT thermograms for sample 2H45 showing (a) initial delamination (235 MPa, 41.8 seconds), (b) complimentary DIC image after first failure, (c) second delamination event, temperature distribution (d) before maximum load, (e) at maximum load (376 MPa, 89.7 seconds), (f) before final failure, (g) at final failure (353 MPa, 102.7 seconds) and (h) complimentary DIC image after failure

Although due to the higher SCF values for 2H45, the failure initiated earlier but the accumulation of failure along the 45° angle is difficult as compared to that of a transverse failure. Therefore, the processing zone shifted, from the central area between the holes to the outer periphery, to ease the accumulation of damage. Since, on the outer edges, the

distribution of stress as seen in Fig. 5-15(d) supports the transversal damage. The specimen 2H45 then continues to carry the load till it reaches its maximum strength of 376 MPa (89.7 seconds) by accumulating the damage on the outer edges of the holes Fig. 5-15(e).

After reaching the maximum strength, both 2H0 and 2H45, remained partially intact and carried the load further. The distribution of stress is observed concentrated on the outer edges of the holes as depicted from the temperature distribution in IRT thermograms, Fig. 5-14(d).and Fig. 5-15(f). At last, at the final failure point both the specimens fail abruptly accompanying interfacial and transversal matrix failure and fiber breakage as shown in IRT thermograms and complementary DIC images in Fig. 5-14(e, f) and Fig. 5-15(g, h). Here, extensive axial delamination events are noticed in the specimen 2H45 as compared to that in the specimen 2H0. The reason for this is attributed to the difference in the orientation of holes and the temperature distribution, equivalently stress distribution, around the holes just before the final failure.

5. 3. 5. Fracture Surface Analysis

The overall fracture morphology of the representative specimens 1H, 2H90, 2H0 and 2H45 is shown in Fig. 5-16(a), (b), (c), and (d), respectively. All the specimens showed a certain level of delamination fracture morphology along with transverse matrix cracking and fiber failure.

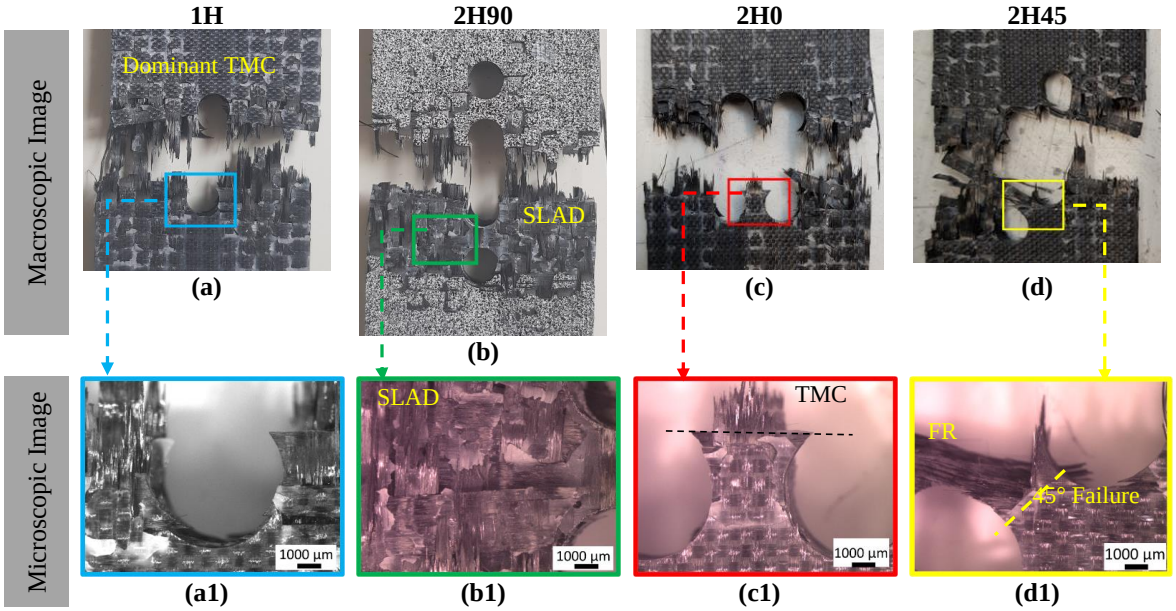

Fig. 5-16. Fracture surface morphology (Note: SLAD – Slanted large area delamination, TMC – Transverse matrix crack, FR – Fiber rotation)

The comparison of fracture surfaces of 1H and 2H90 specimens, having critical regions at the outer periphery of the hole(s), reveals that in 1H specimen the failure is dominated by transversal matrix cracks while in 2H90 large-area delamination fracture is observed. This observation is consistent with IRT results where large-area delamination at edges of the holes in 2H90 while transversal fracture in 1H are apparent, Fig. 5-13(c2) and Fig. 5-12(c), respectively. The higher maximum strength of 2H90 as compared to that of 1H could be attributed to these observations as more active delamination in a fiber-dominated failure directs to higher notched strength [92]. The fracture surface of 2H90 also revealed a slanted through the thickness delamination growth extending across two holes as depicted in Fig. 5-16(b1). Such a phenomenon is only possible due to the interaction between two holes. On the contrary, fewer delamination fracture events could be observed for 1H, Fig. 5-16(a1), which is in agreement with IRT results.

The fracture surface appearance of specimens 2H0 and 2H45, having critical region in-between the two holes, provides interesting complimentary reasons for the higher maximum strength of 2H45 as compared to that of 2H0. On large scale, the fracture of 2H0 is dominated by transverse matrix cracking, Fig. 5-16(c), while the fracture surface of 2H45, Fig 16 (d), reveals features such as higher number of delamination fracture and rotation of weft fibers. Apart from delamination, the change in the orientation of fibers towards the loading direction also suggest a higher load carrying capability of laminates [136, 137] which also ascertains the higher maximum strength of 2H45 as compared to that of 2H0. The magnified pictures of the central portion between the two holes of sample 2H0 and 2H45 are shown in Fig. 5-16(c1) and (d1), respectively. This fracture surface morphology of the critical zone provides information about the delayed damage progression in 2H45 as compared to that of 2H0. In agreement with the IRT results, the fracture at critical zone is controlled by transverse matrix crack in sample 2H0, while in 2H45 the damage progressed across the holes at 45° angle. Moreover, the rotation of weft fiber tow is also visible in the central region of sample 2H45. These observations justify the higher maximum strength value of 2H45, though the SCF is greater than that of the 2H0 counterpart.

5. 4. Conclusions

Well-established methods of FEM incorporated with the DIC and IRT are performed to evaluate the stress concentration factor for four (4) different woven composite specimens, i.e. one single hole and others with two interacting holes, oriented at three different angles (0°, 45°, 90°), under tension. To the best of the authors' knowledge, three-way comparison containing FEM, DIC, and IRT are integrated, for the first time, to understand the failure dynamics of the woven composites with two interacting holes. The stress analysis as well as the strength prediction is conducted in this study. It is shown that adding one more hole with the same size in the longitudinal direction resulted in the enhancement of the final failure load and reduction in stress concentration factor in the vicinity of the hole such that SCF for plate with 2H90 is around 20% less than the 1H sample.

The processing zone for two-hole specimens is determined by DIC technique. The prediction of strength for specimen with processing zone at the outer periphery and/or between holes is carried out utilizing the PSC and EPSC approaches. The required characteristic distances are found through the FEM and DIC, which are in well agreement to each other. The results of strength prediction show that the PSC method could be utilized without any modification to estimate the strength of the sample with processing zone at the outer periphery of notches. However, it is proposed that EPSC method could not be applicable for the woven composites, unlike the quasi-isotropic materials.

Progressive failure analysis is conducted by the IRT technique to unearth the influence of two interacting holes on the failure progression. The time of initial axial-splitting around the hole(s), being earliest for 2H45 and furthest for 2H90, is found to be directly correlated with the SCF values. This axial splitting provided a more adequate crack blunting effect for 2H90 as compared to 1H. The IR thermograms at maximum strength revealed delamination dominated failure of 2H90 as compared to that of 1H, where the failure is controlled by transversal matrix cracking. In 2H0 and 2H45, initially, the damaged is accumulated in the region between the holes but later a transformation of working zone to the outer periphery of holes in 2H45 is unveiled, which resulted in a higher maximum strength of 2H45 as compared to 2H0.

Finally, the fracture surfaces inspection disclosed a slanted through the thickness large area delamination morphology for 2H90 as compared to a matrix dominated failure in 1H with negligible interfacial failure. The comparison of fracture surfaces of 2H0 and 2H45,

provided additional insight into the damage progression such that for 2H0, the major damage, being transverse matrix cracking, remains confined to the region in-between the holes. On contrary, the fracture morphology of 2H45 showed several features such as fiber rotation, higher amount of interfacial failure, and damage growth at 45° angle in-between the holes. These complementary observations further approve the results of mechanical tests and IRT analysis. The future work will include applying an appropriate failure criterion to study the effect of additional holes on the fracture behavior of woven composite materials.

CHAPTER 6. CONCLUSIONS

The conclusions of the chapters 2, 3, 4 and 5 are reiterated here briefly:

- Determining tab material for tensile test of CFRP laminates with combined usage of digital image correlation and acoustic emission techniques

The combined usage of DIC and AE analysis is shown to be valuable for determining a suitable tab material for UD FRPs, under tensile loading. Various stacking sequences were and two different tab materials, namely CFRP and GFRP, were considered. A relatively uniform strain gradient is observed from the full field strain data in case of laminates containing 0°, 15°, 30°, 45° and 60° plies with CFRP used as end tabs. While laminates with 75° and 90° fabric layers, showed a fairly uniform strain gradient with GFRP end-tabs. A more uniform strain distribution, in any case, is shown to be related to a slower damage progression by adopting AE analysis. Three distinctive stages in AE energy release rate were identified and it was observed that the rate of damage accumulation is associated inversely with the span of the second stage of AE activity. For laminates with 0°, 15°, 30°, 45° and 60°plies, the extent of the second stage was found to be longer when CFRP tabs were used, suggesting a slower damage progression as compared to that of GFRP tabs. The slower damage progression, indicating relatively a mild stress distribution, was found to be supporting the uniformity of strain gradient obtained from the DIC data. On contrary, the AE energy release rate, conversely damage accumulation rate, was found to be faster in laminates with 75° and 90°, when CFRP tabs were utilized. Acknowledging the fact that the main physical difference between samples with CFRP and GFRP tabs is the tab material itself, it was perceived that the difference in damage accumulation rates and strain gradient distribution is due to the usage of different tab materials. For 0°, 15°, 30°, 45° and 60° ply configurations mechanical response of carbon tab is close to the sample itself due to akin values off elastic modulus. On the other hand, for laminates with 75° and 90° ply configuration glass tab performs better due to closer elastic modulus as to the sample.

- Investigation on interlaminar delamination tendency of multidirectional carbon fiber composites

The investigation of interlaminar delamination tendency and through the thickness failure characterization of 7 unique angled-ply laminated composites is carried out by concurrently utilizing three different strain monitoring techniques including DIC, SG and FBG sensors, and two damage monitory techniques namely IRT and AE analysis. This approach allowed to understand the variation in damage propagation with varying the orientation of angled plies from 0° to 90° with an increment of 15°. The mismatch and inconsistencies in the strain information from the surface and middle plane of laminates was associated with the failure events and further supported by cross-validation with AE and/or IRT data. A remarkable difference in sequence of failure is seen in laminates with 15°, 45° and 90° plies as compared to that of laminate with all 0° plies, wherein the failure was controlled dominantly by longitudinal splitting events. In laminate with 15° plies, an initial major failure was observed due to edge delamination of angled surface ply, which was vividly observed by sudden strain fluctuations and confirm by damage events seen in AE and IRT data. However, after this initial failure, the inner layers apparently remained intact, and the global failure of the sample occurred at higher stress levels. In laminate with 45° plies, the initial failure was observed, with help of AE and IRT data, to be longitudinal splitting in 0° plies while the damage accumulation in 45° layers was delayed due to possible reorientation of 45° plies towards the loading direction. Transverse matrix cracks at the surface plies of the laminate with 90° layers is observed from the initial stages of the test which was further validated from the early change in slope of stress-strain curve obtained from DIC data. Coalescence of such sequential events, as seen in the IRT thermograms, resulted in sudden failure of the laminate.

- A novel hybrid damage monitoring approach to understand the correlation between size effect and failure behavior of twill CFRP laminates

An in-depth understating of the influence of thickness variation, in laminated composites, on mechanical properties and failure dynamics was developed by utilizing hybrid test setup, further augmenting the significance of such a method. With an increase in thickness from 4.83 mm to 9.87 mm, the tensile strength and shear strength showed an increase of 49 MPa and 20.7 MPa, respectively. Micro-damage initiation point was observed and cross-validated, by comparing the information obtained from AE, IRT and/or DIC, to be earliest in the thinnest laminates as compared to that of the thicker ones. Under uniaxial tension, a relatively active mode of failure, in thinner laminates, was matrix cracking which transformed to a higher energy release rate mechanism i.e., delamination failure in the

thicker ones. A stagnation zone was also identified in the AE energy release rate curve, which was found to be the longest for the thickest laminate and apparently invisible for the thinnest one, suggesting a quicker damage progression in thinner ones. Failure dynamics, in case of shear tests, was majorly identified by the extent of heterogeneity in DIC strain maps within the v-notch region of the test samples. An earlier and more severe heterogeneity in strain maps for thinner laminates suggested that the damage saturated more rapidly in thinner laminates, as compared to that of the thicker ones.

- Stress concentration, strength prediction, and failure analysis of plain-weave CFRP with two interacting notches

Difference in stress concentration, mechanical properties, and failure development in notched woven CFRP laminates with single and two holes, in different orientations (0°, 45°, 90°), was scrutinized by incorporating FEM, DIC and IRT. Drilling an additional hole in longitudinal direction resulted in approximately 20 % reduction of stress concentration factor around the vicinity of the holes as compared to that of laminate with single hole. For the first time, the strain obtained from DIC data was utilized to determine the processing/working zone, by realizing the extent of non-linearity present in the stress-strain curves obtained from points considered at the outer periphery of the holes and in-between two holes. The characteristics distances, to be utilized for strength prediction from PSC and EPSC methods, were also determined by DIC and FEM, which were found to be in well agreement to each other. The results of strength prediction showed that the PSC method could be utilized without any modification to estimate the strength of the sample with processing zone at the outer periphery of notches. However, it was proposed that EPSC method could not be applicable for the woven composites, unlike the quasi-isotropic materials. Progressive failure analysis was conducted by the IRT technique to unearth the influence of two interacting holes on the failure progression. The time of initial axial-splitting around the hole(s), was earliest for 2H45 and furthest for 2H90, was found to be directly correlating with the SCF values. This axial splitting provided a more adequate crack blunting effect for 2H90 as compared to that of 1H. The IR thermograms at maximum strength revealed delamination dominated failure of 2H90 as compared to that of 1H, where the failure was controlled by transversal matrix cracking. Finally, the fracture surfaces inspection disclosed a slanted through the thickness large area delamination morphology for 2H90 as compared to a matrix dominated failure in 1H with negligible interfacial failure. These complementary observations further approved the results of mechanical tests and IRT analysis.

CHAPTER 7. REFERENCES

1. International, A., *ASTM D3039 / D3039M-17, Standard Test Method for Tensile Properties of Polymer Matrix Composite Materials*. 2017: West Conshohocken, PA.
2. Johnson, P. and F.-K. Chang, *Characterization of Matrix Crack-Induced Laminate Failure—Part I: Experiments.* Journal of Composite Materials, 2001. **35**(22): p. 2009-2035.
3. Amara, K., et al., *Effect of transverse cracks on the mechanical properties of angle-ply composites laminates.* Theoretical and Applied Fracture Mechanics, 2006. **45**(1): p. 72-78.
4. Pernice, M.F., et al., *Experimental study on delamination migration in composite laminates.* Composites Part A: Applied Science and Manufacturing, 2015. **73**: p. 20-34.
5. Yuan, Y., et al., *Failure modes and strength prediction of thin ply CFRP angle-ply laminates.* Composite Structures, 2017. **176**: p. 729-735.
6. Chen, B.Y., et al., *Modelling delamination migration in angle-ply laminates.* Composites Science and Technology, 2017. **142**: p. 145-155.
7. Shafighfard, T., E. Demir, and M. Yildiz, *Design of fiber-reinforced variable-stiffness composites for different open-hole geometries with fiber continuity and curvature constraints.* Composite Structures, 2019. **226**: p. 111280.
8. Hensley, S., et al., *Digital image correlation techniques for strain measurement in a variety of biomechanical test models.* Acta of bioengineering and biomechanics, 2017. **19**(3).
9. Majumder, M., et al., *Fibre Bragg gratings in structural health monitoring—Present status and applications.* Sensors and Actuators A: Physical, 2008. **147**(1): p. 150-164.
10. Mulle, M., et al., *Assessment of cure residual strains through the thickness of carbon–epoxy laminates using FBGs, Part I: Elementary specimen.* Composites Part A: Applied Science and Manufacturing, 2009. **40**(1): p. 94-104.
11. Yan, C., et al., *Development of flexible pressure sensing polymer foils based on embedded fibre Bragg grating sensors.* Procedia Engineering, 2010. **5**: p. 272-275.
12. Li, L., et al., *Cluster analysis of acoustic emission signals for 2D and 3D woven glass/epoxy composites.* Composite Structures, 2014. **116**: p. 286-299.
13. Li, L., S.V. Lomov, and X. Yan, *Correlation of acoustic emission with optically observed damage in a glass/epoxy woven laminate under tensile loading.* Composite Structures, 2015. **123**: p. 45-53.
14. Carvelli, V., A. D'Ettorre, and S.V. Lomov, *Acoustic emission and damage mode correlation in textile reinforced PPS composites.* Composite Structures, 2017. **163**: p. 399-409.
15. Zalameda, J. and W. Winfree, *Detection and Characterization of Damage in Quasi-Static Loaded Composite Structures Using Passive Thermography.* Sensors, 2018. **18**(10).

16. Fedulov, B., et al., *Influence of fibre misalignment and voids on composite laminate strength.* Journal of Composite Materials, 2015. **49**(23): p. 2887-2896.
17. Li, Y., et al., *The effect of fiber misalignment on the homogenized properties of unidirectional fiber reinforced composites.* Mechanics of Materials, 2016. **92**: p. 261-274.
18. Wilhelmsson, D. and L.E. Asp, *A high resolution method for characterisation of fibre misalignment angles in composites.* Composites Science and Technology, 2018. **165**: p. 214-221.
19. Mehdikhani, M., et al., *Voids in fiber-reinforced polymer composites: A review on their formation, characteristics, and effects on mechanical performance.* Journal of Composite Materials, 2018. **0**(0): p. 0021998318772152.
20. Wisnom, M.R., *Size Effects in the Testing of Fibre-Composite Materials*. Vol. 59. 1999. 1937-1957.
21. Wisnom, M.R., B. Khan, and S.R. Hallett, *Size effects in unnotched tensile strength of unidirectional and quasi-isotropic carbon/epoxy composites.* Composite Structures, 2008. **84**(1): p. 21-28.
22. Lavoie, J.A., C. Soutis, and J. Morton, *Apparent strength scaling in continuous fiber composite laminates.* Composites Science and Technology, 2000. **60**(2): p. 283-299.
23. Cantera, M.A., G. Czél, and M. Jalalvand, *New Approaches to Quantifying Tensile Strength Variability and Size Effects in Unidirectional Composites*. 2017.
24. Portnov, G.G., V.L. Kulakov, and A.K. Arnautov, *A refined stress-strain analysis in the load transfer zone of flat specimens of high-strength unidirectional composites in uniaxial tension 1. Theoretical analysis.* Mechanics of Composite Materials, 2006. **42**(6): p. 547-554.
25. Worthem, D.W., *Flat tensile specimen design for advanced composites.* 1990.
26. Kulakov, V., et al., *Stress-Strain State in the Zone of Load Transfer in a Composite Specimen under Uniaxial Tension*. Vol. 40. 2004. 91-100.
27. De Baere, I., W. Van Paepegem, and J. Degrieck, *On the design of end tabs for quasi-static and fatigue testing of fibre-reinforced composites.* Polymer Composites, 2009. **30**(4): p. 381-390.
28. Tahir, M.M., W.-X. Wang, and T. Matsubara, *A novel tab for tensile testing of unidirectional thermoplastic composites.* Journal of Thermoplastic Composite Materials, 2019. **32**(1): p. 37-51.
29. Odegard, G. and M. Kumosa, *Elastic-plastic and failure properties of a unidirectional carbon/PMR-15 composite at room and elevated temperatures.* Composites Science and Technology, 2000. **60**(16): p. 2979-2988.
30. Kawai, M., et al., *Effects of end-tab shape on strain field of unidirectional carbon/epoxy composite specimens subjected to off-axis tension.* Composites Part A: Applied Science and Manufacturing, 1997. **28**(3): p. 267-275.
31. Adams, D.O. and D.F. Adams, *Tabbing guide for composite test specimens*. 2002, UTAH UNIV SALT LAKE CITY DEPT OF MECHANICAL ENGINEERING.
32. Czél, G., M. Jalalvand, and M.R. Wisnom, *Hybrid specimens eliminating stress concentrations in tensile and compressive testing of unidirectional composites.* Composites Part A: Applied Science and Manufacturing, 2016. **91**: p. 436-447.
33. P. Nemeth, M., C. Herakovich, and D. Post, *On the off-axis tensile test for unidirectional composites*. Vol. 5. 1982.
34. Kashfuddoja, M., R.G.R. Prasath, and M. Ramji, *Study on experimental characterization of carbon fiber reinforced polymer panel using digital image correlation: A sensitivity analysis.* Optics and Lasers in Engineering, 2014. **62**: p. 17-30.

35. Caminero, M.A., et al., *Damage monitoring and analysis of composite laminates with an open hole and adhesively bonded repairs using digital image correlation.* Composites Part B: Engineering, 2013. **53**: p. 76-91.
36. Depuydt, D., et al., *Digital image correlation as a strain measurement technique for fibre tensile tests.* Composites Part A: Applied Science and Manufacturing, 2017. **99**: p. 76-83.
37. Tekieli, M., et al., *Application of Digital Image Correlation to composite reinforcements testing.* Composite Structures, 2017. **160**(Supplement C): p. 670-688.
38. Ubaid, J., M. Kashfuddoja, and M. Ramji, *Strength prediction and progressive failure analysis of carbon fiber reinforced polymer laminate with multiple interacting holes involving three dimensional finite element analysis and digital image correlation.* International Journal of Damage Mechanics, 2014. **23**(5): p. 609-635.
39. Fan, G., et al., *Improving the tensile ductility of metal matrix composites by laminated structure: A coupled X-ray tomography and digital image correlation study.* Scripta Materialia, 2017. **135**: p. 63-67.
40. Flament, C., et al., *Local strain and damage measurements on a composite with digital image correlation and acoustic emission.* Journal of Composite Materials, 2016. **50**(14): p. 1989-1996.
41. Oz, F.E., et al., *Multi-instrument in-situ damage monitoring in quasi-isotropic CFRP laminates under tension.* Composite Structures, 2018. **196**: p. 163-180.
42. Dahmene, F., S. Yaacoubi, and M.E. Mountassir, *Acoustic Emission of Composites Structures: Story, Success, and Challenges.* Physics Procedia, 2015. **70**: p. 599-603.
43. Yilmaz, C. and M. Yildiz, *A study on correlating reduction in Poisson's ratio with transverse crack and delamination through acoustic emission signals.* Polymer Testing, 2017. **63**: p. 47-53.
44. Fotouhi, M., et al., *Detection of fibre fracture and ply fragmentation in thin-ply UD carbon/glass hybrid laminates using acoustic emission.* Composites Part A: Applied Science and Manufacturing, 2016. **86**: p. 66-76.
45. Kulakov, V.L., et al., *Stress-Strain State in the Zone of Load Transfer in a Composite Specimen under Uniaxial Tension.* Mechanics of Composite Materials, 2004. **40**(2): p. 91-100.
46. Sause, M.G.R., et al., *Pattern recognition approach to identify natural clusters of acoustic emission signals.* Pattern Recognition Letters, 2012. **33**(1): p. 17-23.
47. Tabrizi, I.E., et al., *Experimental and numerical investigation on fracture behavior of glass/carbon fiber hybrid composites using acoustic emission method and refined zigzag theory.* Composite Structures, 2019. **223**: p. 110971.
48. International, A., *Standard Test Method for Tensile Properties of Polymer Matrix Composite Materials,* in *ASTM D3039 / D3039M-17*. 2017: West Conshohocken, PA,.
49. Naderi, M., A. Kahirdeh, and M.M. Khonsari, *Dissipated thermal energy and damage evolution of Glass/Epoxy using infrared thermography and acoustic emission.* Composites Part B: Engineering, 2012. **43**(3): p. 1613-1620.
50. Bussiba, A., et al., *Damage evolution and fracture events sequence in various composites by acoustic emission technique.* Composites Science and Technology, 2008. **68**(5): p. 1144-1155.
51. Yilmaz, C., et al., *A hybrid damage assessment for E-and S-glass reinforced laminated composite structures under in-plane shear loading.* Composite Structures, 2018. **186**: p. 347-354.

52. Wisnom, M.R., *The role of delamination in failure of fibre-reinforced composites.* Philosophical Transactions of the Royal Society a-Mathematical Physical and Engineering Sciences, 2012. **370**(1965): p. 1850-1870.
53. Huang, Z.-M. and Y.-X. Zhou, *Strength of Multidirectional Laminates*, in *Strength of Fibrous Composites*, Z.-M. Huang and Y.-X. Zhou, Editors. 2012, Springer Berlin Heidelberg: Berlin, Heidelberg. p. 145-235.
54. Choi, N.S., A.J. Kinloch, and J.G. Williams, *Delamination Fracture of Multidirectional Carbon-Fiber/Epoxy Composites under Mode I, Mode II and Mixed-Mode I/II Loading.* Journal of Composite Materials, 1999. **33**(1): p. 73-100.
55. Pagano, N.J. and R.B. Pipes, *The Influence of Stacking Sequence on Laminate Strength.* Journal of Composite Materials, 1971. **5**(1): p. 50-57.
56. Miyagawa, H., C. Sato, and K. Ikegami, *Mode II interlaminar fracture toughness of multidirectional carbon fiber reinforced plastics cracking on 0//0 interface by Raman spectroscopy.* Materials Science and Engineering: A, 2001. **308**(1): p. 200-208.
57. Tabrizi, I.E., et al., *Determining tab material for tensile test of CFRP laminates with combined usage of digital image correlation and acoustic emission techniques.* Composites Part A: Applied Science and Manufacturing, 2019. **127**: p. 105623.
58. Ali, H.Q., et al., *Microscopic analysis of failure in woven carbon fabric laminates coupled with digital image correlation and acoustic emission.* Composite Structures, 2019. **230**: p. 111515.
59. Ajovalasit, A. and G. Pitarresi, *Strain Measurement on Composites: Effects due to Strain Gauge Misalignment.* Strain, 2011. **47**(s1): p. e84-e92.
60. Brunbauer, J. and G. Pinter, *On the strain measurement and stiffness calculation of carbon fibre reinforced composites under quasi-static tensile and tension-tension fatigue loads.* Polymer Testing, 2014. **40**: p. 256-264.
61. Munoz, V., et al. *Coupling infrared thermography and acoustic emission for damage study in CFRP composites*. in *The 12th International Conference on Quantitative InfraRed Thermography—QIRT*. 2014.
62. Munoz, V., et al., *Damage detection in CFRP by coupling acoustic emission and infrared thermography.* Composites Part B: Engineering, 2016. **85**: p. 68-75.
63. Cuadra, J., et al., *Damage quantification in polymer composites using a hybrid NDT approach.* Composites Science and Technology, 2013. **83**: p. 11-21.
64. Oz, F.E., N. Ersoy, and S.V. Lomov, *Do high frequency acoustic emission events always represent fibre failure in CFRP laminates?* Composites Part A: Applied Science and Manufacturing, 2017. **103**: p. 230-235.
65. Bertan, B., et al., *Experimental failure analysis and mechanical performance evaluation of fiber-metal sandwich laminates interleaved with polyamide-6,6 (PA 66) interlayers through the combined usage of acoustic emission, thermography and microscopy techniques.* Journal of Sandwich Structures and Materials, 2020.
66. Kuang, K.S.C., et al., *Embedded fibre Bragg grating sensors in advanced composite materials.* Composites Science and Technology, 2001. **61**(10): p. 1379-1387.
67. Emmons, M.C., et al., *Strain measurement validation of embedded fiber Bragg gratings.* International Journal of Optomechatronics, 2010. **4**(1): p. 22-33.
68. Wood, K., et al., *Fiber optic sensors for health monitoring of morphing airframes: I. Bragg grating strain and temperature sensor.* Smart Materials and structures, 2000. **9**(2): p. 163.
69. Canturri, C., et al., *Delamination growth directionality and the subsequent migration processes – The key to damage tolerant design.* Composites Part A: Applied Science and Manufacturing, 2013. **54**: p. 79-87.

70. Eaton, M., *Acoustic Emission (AE) monitoring of buckling and failure in carbon fibre composite structures*. 2007: Cardiff University.
71. Swolfs, Y., L. Gorbatikh, and I. Verpoest, *Fibre hybridisation in polymer composites: A review.* Composites Part a-Applied Science and Manufacturing, 2014. **67**: p. 181-200.
72. Shi, Y.B., D. Hull, and J.N. Price, *Mode II fracture of +θ/-θ angled laminate interfaces.* Composites Science and Technology, 1993. **47**(2): p. 173-184.
73. Greenhalgh, E.S., C. Rogers, and P. Robinson, *Fractographic observations on delamination growth and the subsequent migration through the laminate.* Composites Science and Technology, 2009. **69**(14): p. 2345-2351.
74. Scott, A.E., et al., *Damage accumulation in a carbon/epoxy composite: Comparison between a multiscale model and computed tomography experimental results.* Composites Part A: Applied Science and Manufacturing, 2012. **43**(9): p. 1514-1522.
75. Marthin, O. and E.K. Gamstedt, *Damage shielding mechanisms in hierarchical composites in nature with potential for design of tougher structural materials.* Royal Society Open Science, 2019. **6**(3): p. 181733.
76. Swolfs, Y., *Perspective for Fibre-Hybrid Composites in Wind Energy Applications.* Materials (Basel, Switzerland), 2017. **10**(11): p. 1281.
77. Fikry, M.J.M., S. Ogihara, and V. Vinogradov, *The effect of matrix cracking on mechanical properties in FRP laminates.* Mechanics of Advanced Materials and Modern Processes, 2018. **4**(1): p. 3.
78. Sutherland, L.S., R.A. Shenoi, and S.M. Lewis, *Size and scale effects in composites: I. Literature review.* Composites Science and Technology, 1999. **59**(2): p. 209-220.
79. Sutherland, L.S., R.A. Shenoi, and S.M. Lewis, *Size and scale effects in composites: II. Unidirectional laminates.* Composites Science and Technology, 1999. **59**(2): p. 221-233.
80. Wisnom, M.R., *Size effects in the testing of fibre-composite materials.* Composites Science and Technology, 1999. **59**(13): p. 1937-1957.
81. Wisnom, M.R. and J.W. Atkinson, *Reduction in tensile and flexural strength of unidirectional glass fibre-epoxy with increasing specimen size.* Composite Structures, 1997. **38**(1): p. 405-411.
82. Mehdikhani, M., et al., *Voids in fiber-reinforced polymer composites: A review on their formation, characteristics, and effects on mechanical performance.* Journal of Composite Materials, 2018. **53**(12): p. 1579-1669.
83. Sutherland, L.S., R.A. Shenoi, and S.M. Lewis, *Size and scale effects in composites: III. Woven-roving laminates.* Composites Science and Technology, 1999. **59**(2): p. 235-251.
84. Ashrafi, H., et al., *Tensile properties of GFRP laminates after exposure to elevated temperatures: Effect of fiber configuration, sample thickness, and time of exposure.* Composite Structures, 2020. **238**: p. 111971.
85. Hitchon, J.W. and D.C. Phillips, *The effect of specimen size on the strength of cfrp.* Composites, 1978. **9**(2): p. 119-124.
86. Brien, T.K., *Characterization of Delamination Onset and Growth in a Composite Laminate*, K.L. Reifsnider, Editor. 1982, ASTM International: West Conshohocken, PA. p. 140-167.
87. Jackson, K.E., S. Kellas, and J. Morton, *Scale Effects in the Response and Failure of Fiber Reinforced Composite Laminates Loaded in Tension and in Flexure.* Journal of Composite Materials, 1992. **26**(18): p. 2674-2705.
88. Kellas, S. and J. Morton, *Strength scaling in fiber composites.* AIAA journal, 1992. **30**(4): p. 1074-1080.

89. Saeedifar, M., et al., *Damage assessment of NCF, 2D and 3D woven composites under compression after multiple-impact using acoustic emission.* Composites Part A: Applied Science and Manufacturing, 2020. **132**: p. 105833.
90. (ISO), T.I.O.f.S., *ISO 527-4:1997 Determination of tensile properties of plastics Part 4: Test conditions for isotropic and orthotropic fibre-reinforced plastic composites*. p. 11.
91. International, A., *ASTM D5379 / D5379M - 19, Standard Test Method for Shear Properties of Composite Materials by the V-Notched Beam Method*.
92. Wisnom, M.R., *The role of delamination in failure of fibre-reinforced composites.* Philosophical Transactions of the Royal Society A: Mathematical, Physical and Engineering Sciences, 2012. **370**(1965): p. 1850-1870.
93. AlKhateab, B., et al., *Damage mechanisms in CFRP/HNT laminates under flexural and in-plane shear loadings using experimental and numerical methods.* Composites Part A: Applied Science and Manufacturing, 2020. **136**: p. 105962.
94. Khan, R.M.A., et al., *Investigation on interlaminar delamination tendency of multidirectional carbon fiber composites.* Polymer Testing, 2020. **90**: p. 106653.
95. Kempf, M., O. Skrabala, and V. Altstädt, *Acoustic emission analysis for characterisation of damage mechanisms in fibre reinforced thermosetting polyurethane and epoxy.* Composites Part B: Engineering, 2014. **56**: p. 477-483.
96. Lomov, S., et al., *Monitoring of acoustic emission damage during tensile loading of 3D woven carbon/epoxy composites.* Textile Research Journal, 2014. **84**(13): p. 1373-1384.
97. Massarwa, E., I. Emami Tabrizi, and M. Yildiz, *Mechanical behavior and failure of glass/carbon fiber hybrid composites: Multiscale computational predictions validated by experiments.* Composite Structures, 2021. **260**: p. 113499.
98. Lin, J.-K. and C.E.S. Ueng, *Stresses in a laminated composite with two elliptical holes.* Composite Structures, 1987. **7**(1): p. 1-20.
99. Chang, F.-K., R.A. Scott, and G.S. Springer, *Design of Composite Laminates Containing Pin Loaded Holes.* Journal of Composite Materials, 1984. **18**(3): p. 279-289.
100. Whitney, J.M. and R.J. Nuismer, *Stress Fracture Criteria for Laminated Composites Containing Stress Concentrations.* Journal of Composite Materials, 1974. **8**(3): p. 253-265.
101. Paul, T.K. and K.M. Rao, *Finite element stress analysis of laminated composite plates containing two circular holes under transverse loading.* Computers & Structures, 1995. **54**(4): p. 671-677.
102. Xu, X.W., T.M. Yue, and H.C. Man, *Stress analysis of finite composite laminate with multiple loaded holes.* International Journal of Solids and Structures, 1999. **36**(6): p. 919-931.
103. Xu, X.W., H.C. Man, and T.M. Yue, *Strength prediction of composite laminates with multiple elliptical holes.* International Journal of Solids and Structures, 2000. **37**(21): p. 2887-2900.
104. Green, B.G., M.R. Wisnom, and S.R. Hallett, *An experimental investigation into the tensile strength scaling of notched composites.* Composites Part A: Applied Science and Manufacturing, 2007. **38**(3): p. 867-878.
105. Ataş, A., N. Arslan, and F. Sen, *Failure Analysis of Laminated Composite Plates with Two Parallel Pin-loaded Holes.* Journal of Reinforced Plastics and Composites, 2008. **28**(10): p. 1265-1276.

106. Karakuzu, R., et al., *Effects of geometric parameters on failure behavior in laminated composite plates with two parallel pin-loaded holes.* Composite Structures, 2008. **85**(1): p. 1-9.
107. Karakuzu, R., et al., *Failure behavior of quasi-isotropic laminates with three-pin loaded holes.* Materials & Design, 2010. **31**(6): p. 3029-3032.
108. Ghezzo, F., et al., *Numerical and experimental analysis of the interaction between two notches in carbon fibre laminates.* Composites Science and Technology, 2008. **68**(3): p. 1057-1072.
109. Mahdi Attar, M., *Analytical Study of Two Pin-Loaded Holes in Unidirectional Fiber-Reinforced Composites.* Journal of Applied Mechanics, 2013. **80**(2).
110. Kazemahvazi, S., J. Kiele, and D. Zenkert, *Tensile strength of UD-composite laminates with multiple holes.* Composites Science and Technology, 2010. **70**(8): p. 1280-1287.
111. Achache, H., B. Boutabout, and D. Ouinas, *Mechanical Behavior of Laminated Composites with Circular Holes.* Key Engineering Materials, 2013. **550**: p. 1-8.
112. Yeh, H.Y. and M.D. Le, *Stresses of Composite Laminates Containing Holes and Cracks*, in *Fracture of Engineering Materials and Structures*, S.H. Teoh and K.H. Lee, Editors. 1991, Springer Netherlands: Dordrecht. p. 170-175.
113. Sen, F. and O. Sayman, *Failure Response of Two Serial Bolted Joints in Composite Laminates.* Journal of Mechanics, 2011. **27**(3): p. 293-307.
114. Mao, C. and X. Xu, *Bending problem of a finite composite laminated plate weakened by multiple elliptical holes.* Acta Mechanica Solida Sinica, 2013. **26**(4): p. 419-426.
115. Amaro, A.M., et al., *Influence of open holes on composites delamination induced by low velocity impact loads.* Composite Structures, 2013. **97**: p. 239-244.
116. Ubaid, J., M. Kashfuddoja, and M. Ramji, *Strength prediction and progressive failure analysis of carbon fiber reinforced polymer laminate with multiple interacting holes involving three dimensional finite element analysis and digital image correlation.* International Journal of Damage Mechanics, 2013. **23**(5): p. 609-635.
117. Maksymovych, O. and O. Illiushyn, *Stress calculation and optimization in composite plates with holes based on the modified integral equation method.* Engineering Analysis with Boundary Elements, 2017. **83**: p. 180-187.
118. Jhanji, K.P., et al., *Response of composite laminate with various cut-out combinations to tension load.* IOP Conference Series: Materials Science and Engineering, 2019. **561**: p. 012109.
119. Cai, H., A.-z. Lu, and Y.-c. Ma, *Shape optimization of two interacting holes with different areas in an infinite plate.* European Journal of Mechanics - A/Solids, 2019. **78**: p. 103844.
120. Özaslan, E., et al., *Stress analysis and strength prediction of composite laminates with two interacting holes.* Composite Structures, 2019. **221**: p. 110869.
121. Liu, G. and K. Tang, *Study on stress concentration in notched cross-ply laminates under tensile loading.* Journal of Composite Materials, 2015. **50**(3): p. 283-296.
122. Solis, A., E. Barbero, and S. Sánchez-Sáez, *Analysis of damage and interlaminar stresses in laminate plates with interacting holes.* International Journal of Mechanical Sciences, 2020. **165**: p. 105189.
123. Turan, K., M.O. Kaman, and M. Gur, *Progressive Failure Analysis of Laminated Composite Plates With Two Serial Pinned Joints.* Mechanics of Advanced Materials and Structures, 2015. **22**(10): p. 839-849.
124. Pandita, S.D., K. Nishiyabu, and I. Verpoest, *Strain concentrations in woven fabric composites with holes.* Composite Structures, 2003. **59**(3): p. 361-368.

125. Toubal, L., M. Karama, and B. Lorrain, *Stress concentration in a circular hole in composite plate.* Composite Structures, 2005. **68**(1): p. 31-36.
126. Xu, W., S.I. Thorsson, and A.M. Waas, *Experimental and numerical study on cross-ply woven textile composite with notches and cracks.* Composite Structures, 2015. **132**: p. 816-824.
127. Taheri-Behrooz, F. and H. Bakhshan, *Characteristic length determination of notched woven composites.* Advanced Composite Materials, 2018. **27**(1): p. 67-83.
128. Özaslan, E., A. Yetgin, and B. Acar, *Stress concentration and strength prediction of 2×2 twill weave fabric composite with a circular hole.* Journal of Composite Materials, 2018. **53**(4): p. 463-474.
129. Zhang, H., et al., *Failure analysis of 3D printed woven composite plates with holes under tensile and shear loading.* Composites Part B: Engineering, 2020. **186**: p. 107835.
130. Bhaskara Rao, P., et al., *Statistical analysis for fatigue life evaluation of woven E-glass/epoxy composite laminates containing off-centre interacting circular holes.* Mechanics of Time-Dependent Materials, 2020.
131. International, A., *ASTM D5766 / D5766M-11(2018), Standard Test Method for Open-Hole Tensile Strength of Polymer Matrix Composite Laminates*. 2018: West Conshohocken, PA.
132. Khan, R.M.A., et al., *A novel hybrid damage monitoring approach to understand the correlation between size effect and failure behavior of twill CFRP laminates.* Composite Structures, 2021. **270**: p. 114064.
133. Nima Akhavan Zanjani, S.K., *Stretch Forming Simulation of Woven Composites Based on an Orthotropic Non-Linear Material Model.* Journal of Materials Science and Chemical Engineering, 2015. **3**(7): p. 168-179.
134. O'Higgins, R.M., M.A. McCarthy, and C.T. McCarthy, *Comparison of open hole tension characteristics of high strength glass and carbon fibre-reinforced composite materials.* Composites Science and Technology, 2008. **68**(13): p. 2770-2778.
135. Tan, J.L.Y., V.S. Deshpande, and N.A. Fleck, *Failure mechanisms of a notched CFRP laminate under multi-axial loading.* Composites Part A: Applied Science and Manufacturing, 2015. **77**: p. 56-66.
136. Rotem, A. and Z. Hashin, *Failure Modes of Angle Ply Laminates.* Journal of Composite Materials, 1975. **9**(2): p. 191-206.
137. Sket, F., et al., *Automatic quantification of matrix cracking and fiber rotation by X-ray computed tomography in shear-deformed carbon fiber-reinforced laminates.* Composites Science and Technology, 2014. **90**: p. 129-138.